UNIVERSITY OF BIRMINGHAM

Phase Field Modelling of Nickel Oxidation

Michael Johnson

PhD Thesis

Date: 17th September 2022
Word count: 22,375

Project supervisors:
Dr Nils Warnken and Dr Mary Taylor

Abstract

Reactions occur in metallurgy, developing a methodology for including these reactions into a simple diffusion scheme has been undertaken within this work with an aim to simulate the reactions occurring during oxide growth. The diffusion scheme developed by Larsson [1] was used as the foundation of the scheme. Initially, the growth of Fe_3C in *bcc* phase was simulated; the produced precipitate growth matched that of DICTRA. This technique was modified to simulate the growth of $(Fe, Cr)_3C$ in a *bcc* phase. Further work was conducted to determine the interface reactions between the metal, oxide and gas phases. This simulation was used to model the growth of nickel oxide; these simulations produced k_p results that agreed with Haugsrud [2]. Simulations provided a range of values for unknowns within the model; the rate of oxygen converting from the gas phase and the rate at which metallic nickel becomes ionic. These were determined to be 10 and $100s^{-1}$ and 1×10^{-4} and 1×10^{-5} times metal diffusion in the bulk phase respectively. The equations describing the motion of metal and gas ions within an oxide were modified and written in a phase-field consistent manner. The currently available phase-field models are not designed in a manner that is appropriate for the inclusion of the numerical schemes for the interface reactions; therefore a modified set of phase-field equations are proposed. Phase-field simulations studied the growth of nickel oxide; these simulations require further work to develop the curvature influence between the oxide and gas-phase. The lack of a suitable interfacial curvature limits the simulations ability to grow an oxide into the gas phase.

Acknowledgements

Michael Johnson gratefully acknowledges financial support from the Centre for Doctoral Training in Innovative Metal Processing (IMPaCT) funded by the UK Engineering and Physical Sciences Research Council (EPSRC), grant reference EP/L016206/1.

I would like to thank Dr. Nils Warnken for his continued support throughout my thesis, for providing thoughtful and insightful comments about the work that has been undertaken and pushing me to produce work of a higher quality and standard than I would have been able to without his support and guidance.

I would like to thank my family for their never ending care and support. They have always encouraged me to pursue my interests and passions and have been by my side throughout it all.

Finally I would like to thank my wife Grace for her continued support throughout the course of my PhD, for being my biggest supporter in all things, especially the time and evenings apart that have been spent working towards this thesis.

Contents

Chapter 1

Introduction

Nickel-based superalloys are the material choice for aerospace turbine blades [3, 4]. Current generation nickel-based superalloys are designed to operate at temperatures above the materials melting point during service. Nickel-based superalloys are also able to maintain their mechanical properties up to 85% of their melting temperature due to the presence of a fine particulate phase [2, 5–20] which makes them suitable for the high mechanical loads present within an aerospace turbine.

The development of alloys traditionally has taken an empirical trial-and-error approach, where the addition and modification of certain elements are used to promote the ideal properties of the material. For nickel-based superalloys which have more than 10 alloying additions this results in the modification of elements being a costly and time-consuming procedure due to the chemically complex nature of the different additions [8, 21–26]. Alloying additions can be broken down into four main categories; base elements, mechanically strengthening elements, long term stability elements and oxidation resistance elements [3, 27].

Most alloying additions have a critical concentration that must be reached before the desired properties are shown; this is particularly important if the additions help to provide oxidation resistance in the form of a protective oxide film [21, 28–30] as there is a need for sufficient metal to form an oxide. There is concern with spallation removing sufficient

amounts of an element resulting in the material no longer being protective [31, 32]. Spallation is the breakaway of an oxide layer that has formed on the surface of the metal. The effect of spallation is the reduction of the total amount of the alloying addition in the bulk and the materials ability to form a new protective oxide.

Re and Ru additions enhance the creep resistance of the material, however, these elements have a high-cost and high density which make it disadvantageous for use within turbine blades [33–37]. The low diffusion coefficient of Re and Ru enhances the materials creep resistance by limiting how quickly mass is able to move [26, 38]. The main additions to improve the oxidation resistance of nickel-based superalloys are Al and Cr and their formation of Al_2O_3 (alumina) and Cr_2O_3 (chromia) respectively [25, 39], these oxide layers reduce the motion of metal and oxygen ions in the oxide which reduces the oxidation rate. The reduction in oxidation rate results from the oxide impinging the rate at which metal or oxygen ions diffuse. Small additions of rare earth elements (Y, Hf, La, Y and Zr) can increase the scale adherence and reduce the rate of oxidation as they segregate to grain boundaries where they form oxides subsequently decreasing the outward flux of cations [25, 27, 40–46]. The presence of rare earth elements also alters the mechanism by with which oxidation occurs as these elements form oxides which block the fast diffusion along short circuit diffusion paths. Once the short-circuit diffusion paths are blocked diffusion occurs through the bulk oxide reducing the oxidation rate by up to two orders of magnitude [2, 46, 47]. The addition of iron helps improve the workability of the material, and reduces the materials cost, however, in large concentrations iron is detrimental to the oxidation rate of the alloy [48, 49]. Designs for aero-engines is closely linked to the development of new materials, particularly those which are suitable for improving and replacing the existing materials.

The use and range of applications for nickel-based superalloys are steadily increasing, the main uses are from gas and jet turbines, specifically within the sections that are subjected to high temperatures [16, 27, 32, 50–63]. The most common component is turbine blades and vanes, but increasingly with applications for turbine disks [64–73].

Nickel-based superalloys are extensively used within the oil and gas industry; for parts where the superior corrosion resistance is required [8, 74–77]. Alternative industries are looking to Nickel-based superalloys with interest for applications such as the exhaust manifold for a formula one engine [78]. High performance nickel-based superalloys are becoming increasingly interesting for a wide range of industries, but are still primarily used within the aviation industry (75% of all produced), around 25% of produced nickel-based superalloys are used within the chemical and nuclear industries [51, 55, 77–87].

Due to the ability of nickel-based superalloys to operate at high temperatures, the effects of oxidation upon the material become more critical and can influence the materials lifetime [88, 89]. The impact of oxidation upon nickel-based superalloys is only due to increase due to the drive from governments and the public to increase the efficiency of flight; increasing the turbine efficiency occurs from increasing the operating temperature. Current efficiency gains within oxidation have resulted from an increase in the operating temperature of the material [3]; this has required material optimisation that has resulted in increased stresses on the material.

Current approaches to increasing the operating temperature of nickel-based superalloy aerospace turbines is to apply layers of barrier coatings [4, 89] onto the surface and producing internal cooling channels [90] within the turbine blades. The external coatings are present to increase the oxidation resistance and decrease the temperature experienced by the turbine blade materials [4]. These coatings are only suitable, providing that there is a good adhesion between the coating and the base substrate [4]; different coatings are applied to reduce any thermal expansion-mismatch between these barriers with the drive to increase the lifetime of the coating [4, 89]. Oxidation of the substrate is concerning as this is a mechanism for removing barrier coatings. Oxidation can reduce the thickness of the turbine blade; should sufficient amounts of the turbine blade material be oxidised, this can lead to creep having a more significant influence on the turbine blade causing failure due to thickness-debt effect [90].

The majority of oxidation modelling looks at how initial oxides grow which are based

on density functional theory (DFT) [91, 92], and molecular dynamics (MD) [93–95] techniques. These techniques are suitable for describing the early stages of oxide nucleation and development but are not used to describe long term oxidation due to the computational costs of doing so. There is a growing amount of interest into providing longer term oxidation simulation results using approaches based on CALPHAD. One model simulating the flux of elements for oxidation has been produced [96]; this focuses on considering the diffusion along grain boundaries and does not have a description for the phase interface. Recently a phase-field model for modelling oxidation has been developed by Kim et al. [97]. The studies model uses the MOOSE framework and has been highly optimised to work in multiple dimensions, but does not track the diffusion of individual atoms. The approach used within this work has problems simulating an alloy being oxidised because it does not consider the effects of the different elements on the resulting oxidation.

To model oxidation, a numerical scheme needs to be used that is suitable to simulate the different conditions that occur within oxidation; the gas-oxide interface, the oxide metal interface and the inter-oxide flux of anions or cations [14, 98]. The simulation range and timescales are also significant, as oxidation occurs over hundreds of hours. A numerical model that can simulate the effects of oxidation over long time scales and additionally for a range of initial oxide thicknesses, from nanometers to multiple micrometres, is also essential. Techniques that focus on individual atoms [2, 99] are not suitable for simulating the timescale or simulation volumes required to get meaningful results within a realistic timescale; this requires the production of simulations that focus on the macro-evolution.

The timescale for aerospace turbine design cycles are $3-5$ years, whereas the development of new high-performance alloys is every $10-20$ years [100]. The result of this is that the new alloys are not on the cutting edge of technological advancements in terms of their mechanical properties and being able to influence the design of the turbine in development [100]. Reducing the timescale for alloy development is of growing interest. However, the reliance on physical experiments which are trial-and-error [25, 101] related is problematic as it slows down the possible combinations of alloying elements which are tried. The use of numerical models to help influence the choices for physical experiments could be used to

try more exotic and varied combinations of elements. A numerical model that is suitable for describing a wide range of different effects such as oxidation, creep and fatigue would have the possibility to improve alloy design cycles [52].

The complexities in producing a numerical model for simulating oxide growth have resulted in little progress to the equation defined by Wagner in the 1950s [102]; defining the rate of oxidation to be the square root of time multiplied by a constant ($\Delta Z = \sqrt{K_n t}$). Wagners equation is used to describe the rate of oxidation but does not allow any scope for looking into the different effects of the morphology and microstructure on the material. The simplifications in the equation do not consider multiple elements contributing to the oxide growth rate.

This work seeks to develop a numerical model suitable for providing insight into physical processes occurring during oxidation. The model seeks to describe the interfaces between the metal, oxide and gas phases in a thermodynamically consistent manner. The created model will use available thermodynamic data from CALPHAD (CALculating PHAse Diagrams) [103] assessments. Further this seeks to develop these methods and produce a phase-field model; this modelling technique was selected due to the range of different effects that phase-field models are designed to simulate. A phase field model allows this technique to increase in complexity and produce a resulting output for oxide growth rate and stability by developing the work on already established techniques and methodologies [104–106]. Creating a method to scale easily in terms of elemental complexity is advantageous for simulating nickel-based superalloys with their complicated mix of more than 10 elements [101]. A model that can realistically simulate an alloy system, like nickel-based superalloys, requires there to be appropriate thermodynamic databases for the complex combination of elements. A phase-field model that can simulate various elements during oxidation would provide alloy designers with more direct and immediate feedback. The result of the phase-field model can help to influence the selection of different elements used in experimental validation tests. The understanding gained from such a process would give insight into how different elements mix and influence mechanical properties such as oxidation, creep and fatigue whilst reducing the cost of time and material to test a wide

range of alloys. This work seeks to be the basis of a tool that materials engineers can use to help design future alloys for use at high temperatures within turbine blades; increasing the operating temperature increases the efficiency of turbines, therefore reducing the emission of greenhouse gases.

Chapter 2

Background

2.1 Oxidation

Oxidation of metals is a chemical process in which a metal loses one or more electrons and joins with an oxygen ion to form an oxide. The formed oxide acts as a protective coating which helps to reduce further oxidation. However, the oxide may spall off, re-exposing the surface to oxygen [107]. From comprehensive experimental and theoretical investigations, the general oxidation behaviour is dependent on the composition and exposure conditions such as oxygen pressure and temperature [60].

2.1.1 Material

The study of pure systems is of interest in oxidation as it provides an understanding of different oxidation mechanisms based on various elemental contributions. An example is Cu_2O, which has been used to study the initial stages of oxidation [108]. Understanding the early stages of oxidation gives an idea of the mechanisms and thermodynamics of oxidation. The pure nickel system has been extensively studied and found to have a significant variation of results [109]. It has been found that the presence of dissolved foreign materials (impurities) affects the oxidation rate [35, 102, 110–112], this is hypothesised to be the result of different valencies of added elements that reduces the number

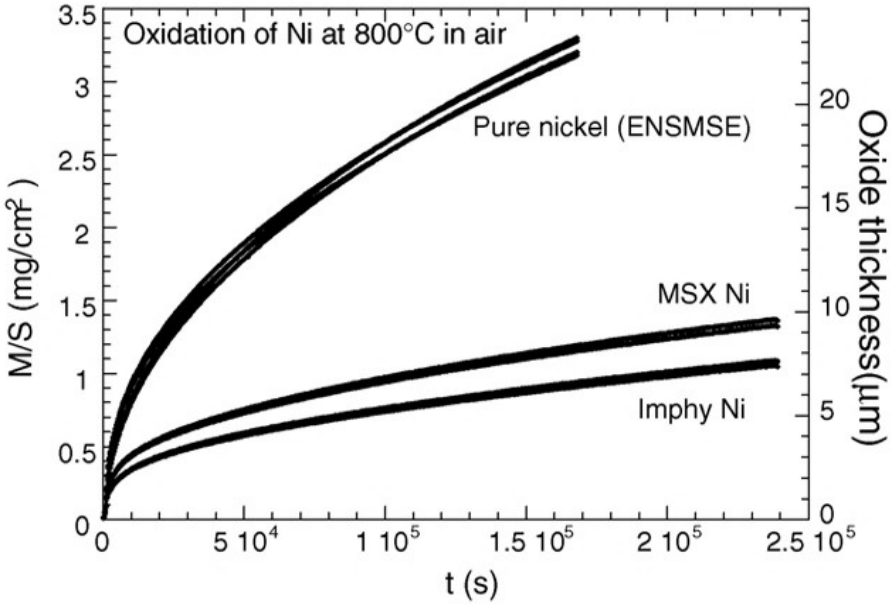

Figure 2.1: Oxidation rate for high purity Nickel samples vs industrial high purity nickel at 800°C [121].

of electron holes. Increasing the number of electron holes increases the number of cation vacancies in the oxide [113]. The literature has documented that the presence of higher valent, less noble elements has the most significant effect on the oxidation rate [113–120]. Nickel self-diffusion can differ by a factor of 10 at high temperatures; the cause for such discrepancies is the presence of impurities within the sample; seen by the difference in growth rates within Figure 2.1 [2, 112, 121]. The oxidation rate of nickel with small added concentrations of Cr can be significant and highlight the effect of impurities on the oxidation rate [116]; Figure 2.2 shows the discrepancy in calculated and measured values.

Impurities within oxide samples not only affect the oxidation rate; oxidation rate values for different purity's of nickel are displayed in Table 2.1 and graphically shown in Figure 2.2 and 2.3); they can also cause oxide film failure [109]. Oxide film failure from impurities results from more reactive components and insoluble metallic particles. The more noble components concentrate at the metal-oxide interface, where these elements can affect the interface adhesion and result in spallation of the oxide from the metal substrate [109]. The Oxidation of ultra-high purity nickel(99.995%) has been shown to not buckle up to 1100°C , additionally, the presence of external stresses did not result in spallation [123]. SEM micrographs showed that only the columnar oxide grain layer formed at high purity nickel samples shown in Figure 2.4 by two SEM micrographs after oxidation for an alloy

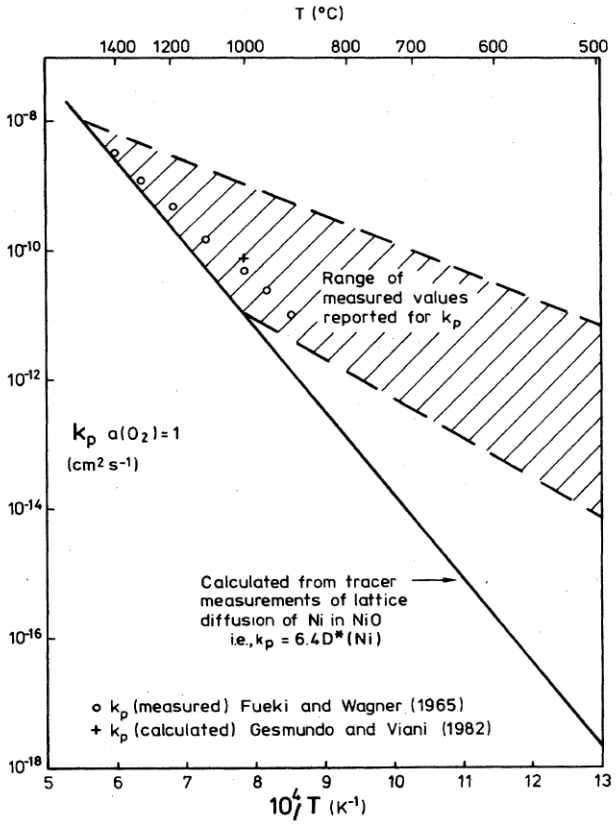

Figure 2.2: Parabolic rate constant measured for the growth of NiO on Ni in oxygen compared with that calculated using Wagner's theory and the tracer diffusion of Ni in the NiO lattice [118].

and high purity nickel [123, 124].

Table 2.1: Oxidation rate constants for different purity's of Nickel [124]

Temp (C)	Rate constant k_p $(\mu m/hr^{\frac{1}{2}})$	
	99.6% Ni	99.995% Ni
1000	8.45	3.89
900	4.09	2.82
800	1.58	

The high-temperature resistance of nickel-based superalloys is attributed to the rapid formation of coherent chromia and alumina oxide scales which are chemically stable and more protective than nickel oxide [39, 125–127]. Samples have shown chromium depletion in the material with a large amount of chromium-oxide. The depletion is hypothesised to have occurred where originally voids were present, reducing the availability of chromium to form the oxide. These voids were filled with oxide by the inward diffusion of oxygen by removing the surrounding chromium; Figure 2.5 shows this depletion of chromium around voids in the material. These locations may also have been where the original metal surface was; Figure 2.6 shows chromium depletion at the initial surfaces location

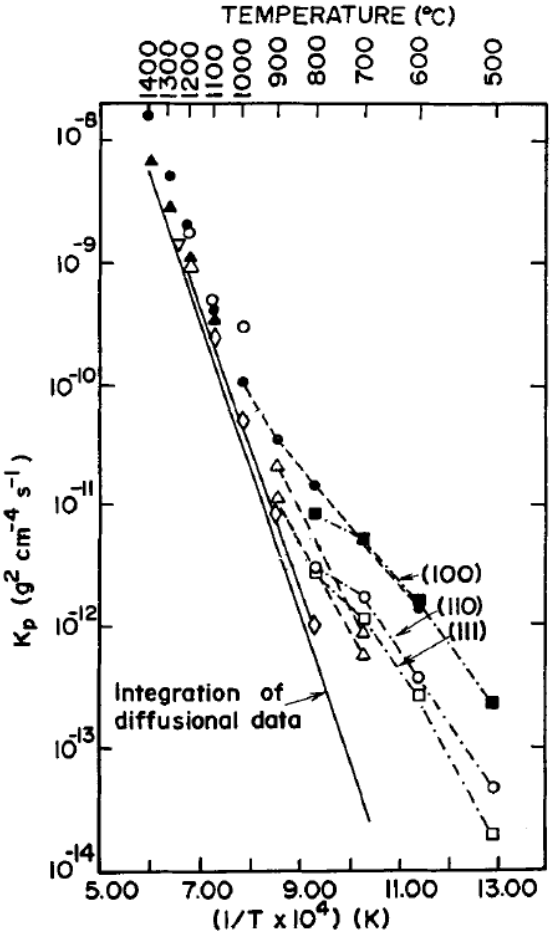

Figure 2.3: Parabolic rate constants for the oxidation of Ni to form NiO in 1atm pure oxygen [109, 122].

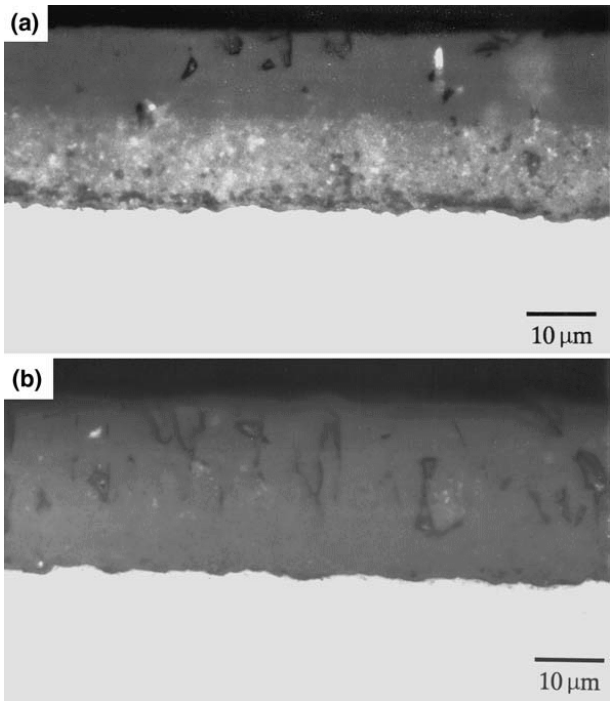

Figure 2.4: Oxide cross sections for A Ni200 and b 99.995% Ni after oxidation for 12.5h [123].

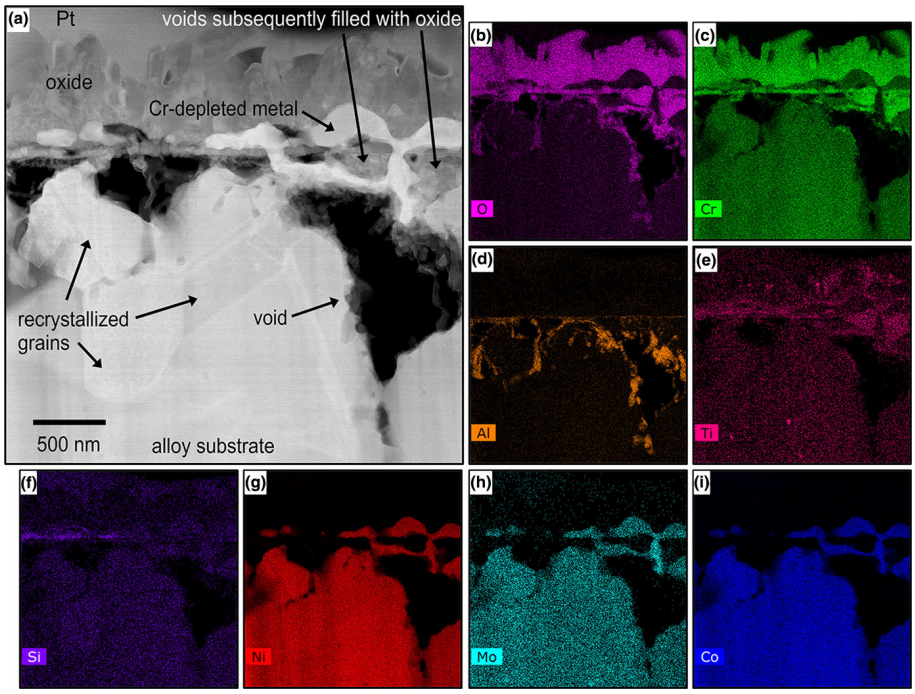

Figure 2.5: Cross-sectional TEM results of alloy 617 exposed to CO_2 at 700°C and 20MPa for 500h using an autoclave. (b) STEM image, (c-j) EDS mapping of region (b) [128].

[128]. The depletion of Cr from the bulk may result in a lack of carbides and may affect the formation of a protective oxide if the oxide spalls.

2.1.2 Initial Oxide Growth

Oxidation starts with oxygen chemisorption, which induces two-dimensional surface structures, followed by the nucleation and growth of oxide films. Composition and crystal structure determines the growth of oxide films and whether the oxide grows into the material or on the surface [129, 130]. The nucleation of an oxide island requires the capture of oxygen atoms. Each oxide island has an active zone where oxygen can be captured; the radius of the active zone is proportional to the oxygen surface diffusion rate. The probability of there being a nucleation event is proportional to the fraction of available surface area outside of the available active zones [129] Figure 2.7 presents TEM images of simple geometric islands formed on the surface of a copper-platinum alloy.

Initially, the nucleation of an oxide layer is equiaxed as there is a large driving force for oxidation as the metal is in contact with the atmosphere. The driving force decreases as the surface becomes covered by oxide, and the grains grow, preferring a columnar

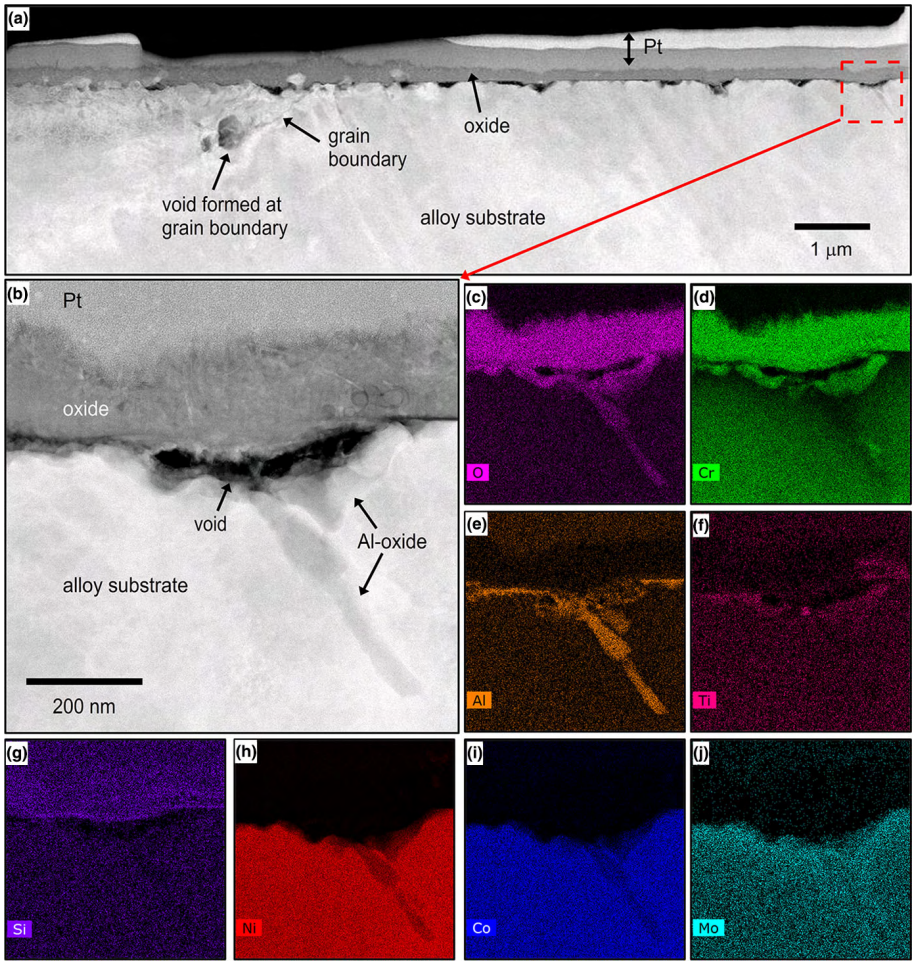

Figure 2.6: Cross sectional TEM results of alloy 617 exposed to CO_2 at 700°C and 0.1MPa for 100h using a tube furnace, (a) low magnification STEM image, (b) higher magnification STEM image of the region indicated in (a). (e-j) EDS mapping of the region shown in (b) [128].

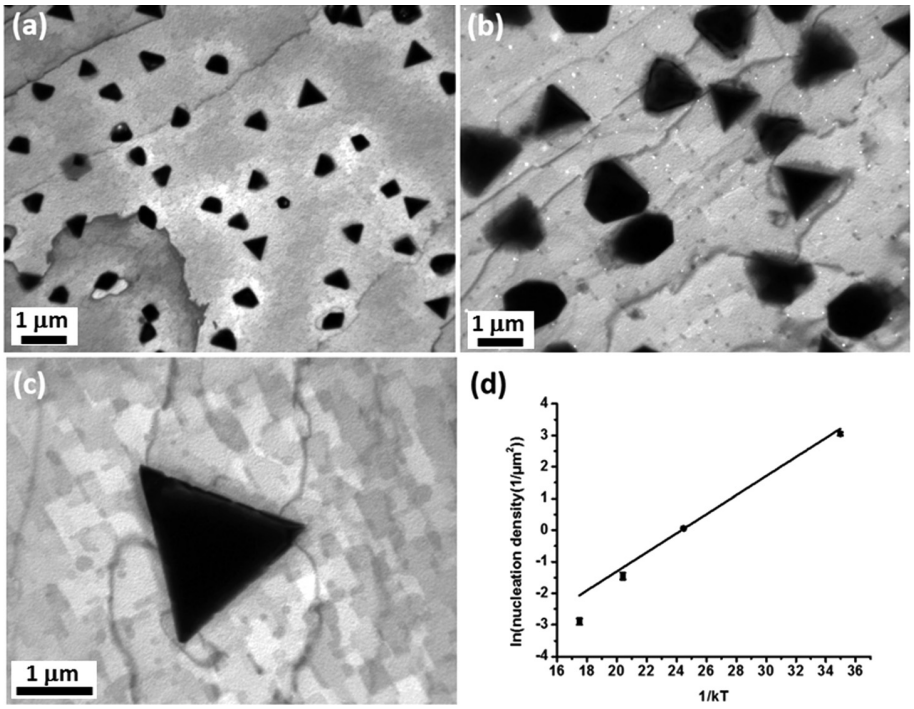

Figure 2.7: Bright field TEM images of surface oxidation of Cu-5at%Pt (100) alloy at (a) 500°C , (b) 600°C , (c) 700°C , and (d) a plot of nucleation density vs 1/kT representing the Arrhenius dependence of the nucleation density [129].

grain structure. Once small islands of columnar grains are present, these grains grow to impingement [131]. The principle of lattice diffusion cannot explain the growth of the inner oxide film; this is, however, related to the purity of the materials [2, 132, 133]. Once oxides cover the surface of the metal, the bulk oxide grows into the metal or away from the metal surface [134]. This mechanism for the formation of an oxide film is known as "grain boundary sweeping".

After the formation of the initial layer of oxides on the metal surface, there is subsequent growth of the oxide, which requires ions diffusing through the oxide for the reaction to proceed [135, 136]. Diffusion of the mobile species (anions/cations) is the rate-limiting step for oxide film growth; therefore, the reactions at the interface play a minor role in influencing the rate of oxidation. In his original model, Wagner assumed that the interface reactions played a minor role in the rate of oxidation [109, 118, 137, 138].

At the early stages of copper oxidation, Cu_2O islands nucleate rapidly and form a discontinuous branched structure; further oxidation causes these oxide islands to coalesce together and form an oxide structure [139]. The oxide islands grow as the probability

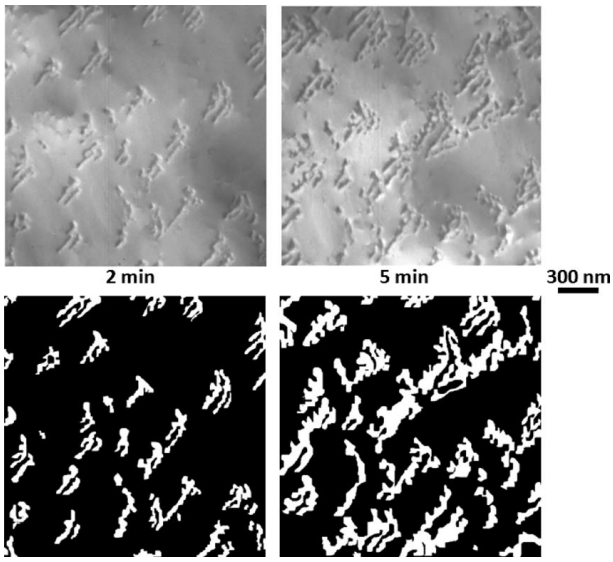

Figure 2.8: In situ TEM images of oxide islands formed on Cu(111) at 450°C and 5×10−4 Torr oxygen pressure [139].

for an oxygen atom to join onto an existing island is higher than the formation of a new island [139] Figure 2.8 shows TEM images of copper oxide islands growing on a copper substrate. Dislocation and stacking faults in copper films have a minor effect on the oxide nucleation and growth; however, significant surface roughness can enhance the nucleation of oxide islands [129, 140, 141]. Other research has shown that surface roughness affects the oxidation resistance [42, 142–146, 146, 147]. The roughness in the surface limits the mobility of oxygen over the surface, resulting in a higher density of the oxide islands and thus slowing down the lateral growth of oxide islands. Copper forms a thermally rough surface over 700°C ; rough surface oxidation tests were conducted at 750°C and smooth at 650°C . The oxides were shown to grow in three dimensions; if the island growth has a linear dependence on time, then the growth of the oxide must be surface diffusion dominated; the growth of copper oxide islands at 650°C and 750°C after 10 minutes are shown in Figure 2.9 [140]. As the data was measured over relatively short time scales (under 60 minutes), the temperature difference has little bearing on the oxide growth rate.

2.1.3 Mechanism

During oxidation, the interfaces move fast compared to the timescale for establishing local equilibrium; therefore, a non-equilibrium approach is required [148]. Generally, the generic

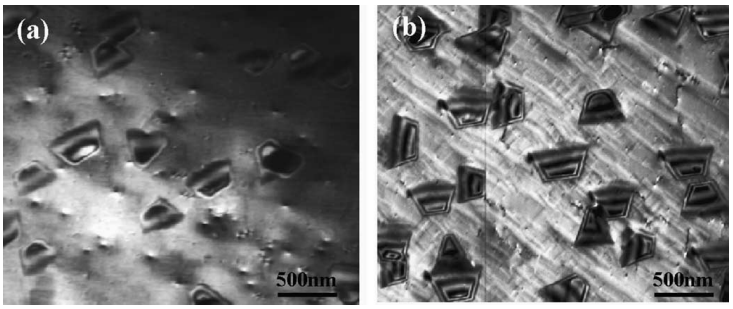

Figure 2.9: Dark field images of oxide islands formed on (a) flat Cu(110) surface at 650°C and (b) thermally rough surface at 750°C at $5 \times 10^{-}4$ Torr oxygen pressure after 10 minutes [141].

driving force of high-temperature oxidation can be separated into transport mechanisms, solid-state diffusion, and thermodynamics of chemical reactions [149]. The oxidation rate for pure nickel oxidised in air at 1000°C is inversely proportional to the thickness of the oxide layer, which in turn is proportional to the displacement of the metal surface (Z) [102]. The rate of oxidation can be determined from equation Equation 2.1, where n is the best fit of data where n= 2 results in parabolic growth, K'$_n$ is a rate constant and Δm is the specific weight gain [150],

$$(\Delta Z)^n = K'_n t \tag{2.1}$$

$$(\Delta m)^n = K'_n t \tag{2.2}$$

Oxidation of high purity metals on flat surfaces produces a single compound oxide adherent to the metal. The thickness of oxide formed from oxidation depends upon the oxide's oxidising temperature, plastic properties, and the sample's shape and size. As the oxide is plastic, this allows deformation to ensure adherence between the oxide and base metal; as the base metal is depleted, the plasticity of the oxide decreases due to the smaller volume of the metal substrate. The reduced plasticity of the oxide reduces the ability to form a good oxide adherence which can result in a longitudinal crack that forms at the corner and spreads down the surface of the oxide-metal interface [119, 138].

Mrowec generalised oxidation by considering what a ternary oxide would look like under different physical oxide properties. The oxidation of a sample that forms two oxide phases,

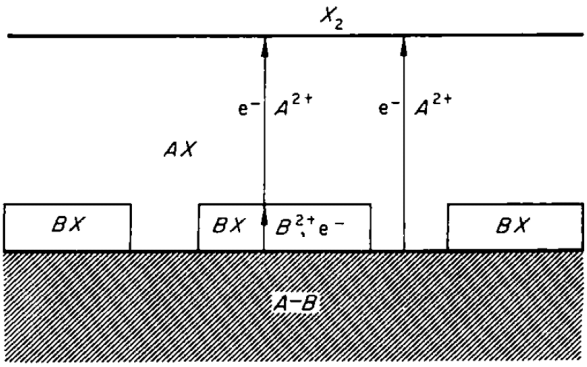

Figure 2.10: Schematic showing the formation of an oxide on binary layers where there is no mixing of oxides [138].

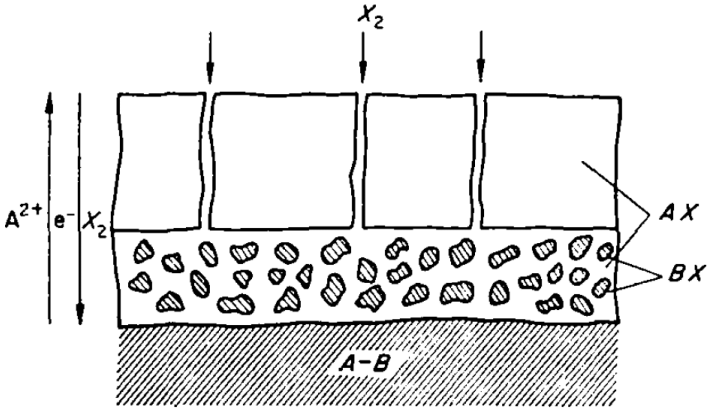

Figure 2.11: Schematic showing the oxide structure for binary oxide where the oxides are porous and there is no mixing of oxides [138].

AX and BX, where they are mutually insoluble; metal A has a much smaller affinity for the oxidant than element B. The oxide AX grows faster than BX as there is a smaller concentration of defects. The AX layer forms a complete coverage of the material and islands of BX at the interface of the two phases; schematically represented in Figure 2.10. The islands of oxide BX act as a mechanical obstacle for plastic flow resulting in the layer AX losing contact with the metal substrate; this dissociation of the outer oxide ruins the oxide layer's compactness. The outer layer grows AX between cracks in an attempt to close the present cracks in the oxide, but this increases the oxidation rate, as the cracks are never fully closed, allowing oxygen to ingress into the oxide; represented within Figure 2.11 [119, 138].

An oxide is formed on a metal surface when heated in an oxygen atmosphere. The oxide layer is generally not porous; further reaction is only possible by diffusion of metal or oxygen within the solid oxide. If the diffusion is slow, the oxidation rate is controlled by

the diffusion process [151]. The oxide grows on the metal by transporting electrons, ions, atoms or molecules through the oxide scale. The ability of the oxide to protect the metal by acting as a barrier depends on the mechanical integrity of the scale forcing diffusion to occur through the oxide phase. Measurements of the diffusion coefficients within oxides are complex; there has been significant work in making measurements which are used to explain the rates at which oxides grow on a range of metals [133].

The mechanisms which drive oxidation are challenging to measure; for nickel oxide growth, the oxidation behaviour has been well studied. Despite being well studied, the oxidation mechanism is complex, and how oxygen ingress occurs is not fully understood [11, 121, 152]. The oxide structure determines whether electronic currents are carried by electrons or holes, which is linked to a consideration of the primary ion transport, whether it is cations or anions respectively [118]. Electrons are more mobile than metal ions due to their smaller size; the electric field produced by the electrons and ions will influence the motion of ions and electrons or holes until equilibrium is reached. Equilibrium is reached when the electric currents of the diffusing species are equal, but opposite [118]. Wagner's initial model assumed that there should be no net electrical current flowing across the film [118]. For the case of nickel, the electrical conductivity is mainly controlled by electron holes; the mobility of these holes are around 10^4 times greater than that of vacancies [116]. In the case of chromium-rich oxide films on iron, oxide growth occurs from the fast outward flux of chromium along the grain boundaries prompting the formation of $FeCr_2O_3$, Cr_2O_3 or both [149].

The location where an oxide grows depends upon which species has the faster mobility; if the mobile ion is oxygen, the oxide grows at the oxide/metal interface, whereas if the mobile ion is a cation, then the oxide grows at the oxide/gas interface [153, 154]. The bulk diffusion for nickel occurs via the outward diffusion of Ni^{2+} within the oxide by an exchange of cationic vacancies [2, 116, 138, 153, 155]. This view is supported by research by Atkinson, who determined that the rate of lattice diffusion was much slower than nickel grain boundary diffusion [118, 133]. The diffusion rate along grain boundaries was determined to be comparable with the diffusivity of Ni within the NiO Lattice [2]. Further

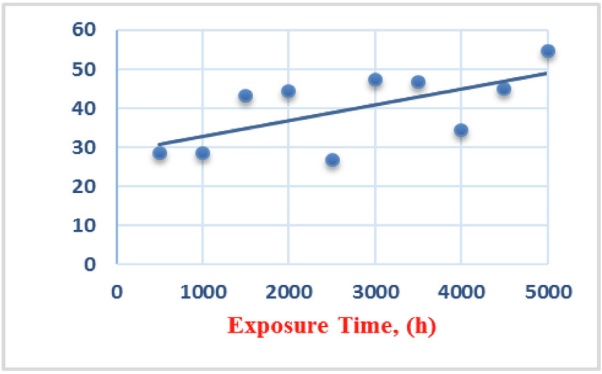

Figure 2.12: Chromium wt% measured on the surface, plotted as a function of time of exposure (measured from EDS analysis) [156]

evidence for the motion of cations is the presence of Kirkendall voids at the oxide/metal interface [60].

Few studies exist to provide an understanding of the oxidation of ternary systems. The lack of studies is due to the complexity arising from the interactions of all the alloying species present within the oxide and the competing growth of different oxides [107]. This limitation becomes very apparent when studying the oxidation of a nickel-based superalloy as there are multiple alloying additions [22]. Oxidation occurs faster than diffusion; this results in complications in understanding the thermodynamics as the compositions are often thermodynamically unstable [130]. This non-equilibrium state is the cause of solute trapping of nickel and chromium during experiments in NiCrMo alloys [60, 148]; Figure 2.12 showing chromium concentration increasing on an oxides surface over time. A complication with trying to understand the thermodynamics of oxidation results from the oxidation state being far from equilibrium which causes there to be a complicated interplay between kinetic and thermodynamic effects [130]. Oxide scales grow from the diffusion of ions; therefore, the growth of an oxide will depend on the gradient in chemical potential and the gradient within an electric field, which may develop from a separation of charge [118]. In general, for any diffusing species i, the flux is given by;

$$J_i = \frac{D_i C_i}{kT}\left(\frac{-d\mu_i}{dx} + q_i E\right) \tag{2.3}$$

where C_i is the concentration, μ is the chemical potential of species i, D_i is the diffusion

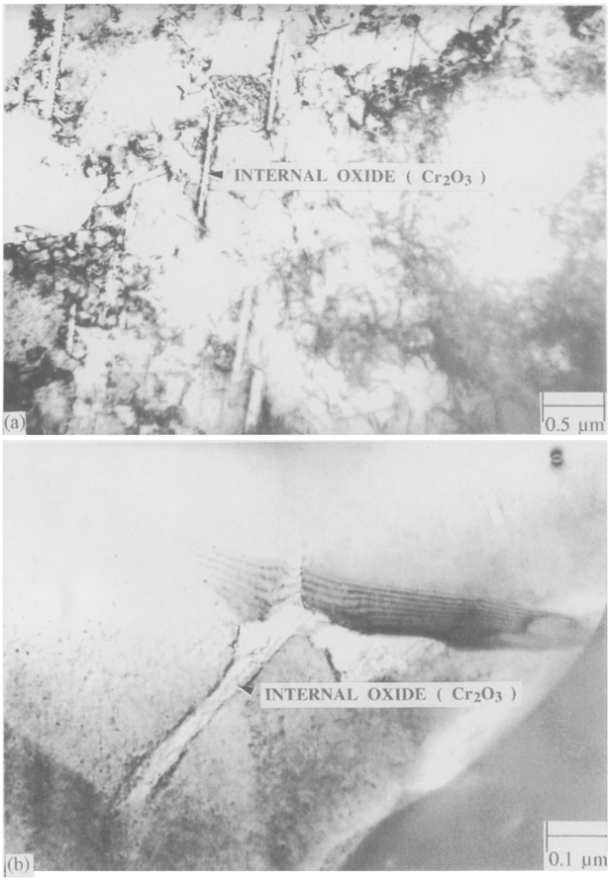

Figure 2.13: TEM transverse-section image of Ni-1at%Cr substrate after 15 minute oxidation at 1273K showing (a) internal oxide particles and (b) internal oxide formation along the grain boundary of the metal substrate [157]

coefficient and q_i the charge of the diffusing species, and E is the electric field [118]. The diffusion of oxygen into the oxide occurs via continuous or partially continuous microchannels or interconnected porosity within the oxide. SIMS studies have shown the motion of gaseous oxygen into the oxide via these mechanisms [2, 132, 133, 155, 157]; Figure 2.13 shows internal oxides present after oxidation. Oxygen ingress into an oxide may occur once the surface cracks during an applied load [2, 47, 138, 153, 158].

The motion of ions is coupled to the opposite flux of vacancies; these vacancies can coalesce to form pores if the annihilation of vacancies is not fast enough [2, 154, 159]. Ordinarily, vacancies annihilate through grain boundaries or dislocations [154, 159].

Predicted oxidation rates show a large discrepancy that is several orders of magnitude slower than observed experimentally; this discrepancy is the result of diffusion along grain boundaries known as short-circuit diffusion paths, rather than being purely driven by lattice diffusion [118, 132, 155, 158, 160]. Along high angle grain boundaries of the

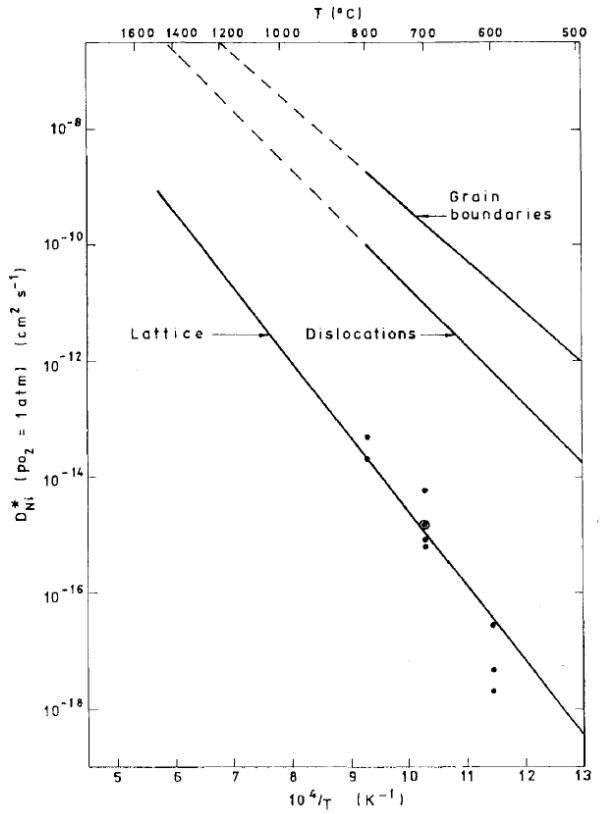

Figure 2.14: Arrhenius plot of tracer diffusion coefficient for Ni diffusion in NiO along the lattice, dislocations and along grain boundaries [133].

(100) plane, the diffusion rate of nickel in NiO is almost 6 orders of magnitude faster than bulk diffusion for a temperature range of 500-800°C [133, 161]; Arrhenius plots Figure 2.14 show a different ion diffusion rates for different routes Figure 2.15 presents the effect of high angle grain boundaries on ion diffusivity. The transport of material within grain boundaries depends on several factors; the geometry of the grain boundaries, the level of stoichiometry and the solute segregation within the material. [160, 162, 163]. The transport along grain boundaries causes there to be greater penetration in the alloy near the grain boundaries from a lateral supply of oxygen [160], and beneath grain boundaries, there will be a higher consumption of metal [157, 158] (c.f. Figure 2.16).

2.1.4 Thermodynamics

Thermodynamically, the oxidation mechanism can be described by the metal surface being thermodynamically unstable due to the oxygen atmosphere. The formation of an oxide separates the metal from the ambient atmosphere. Therefore the driving force is the free

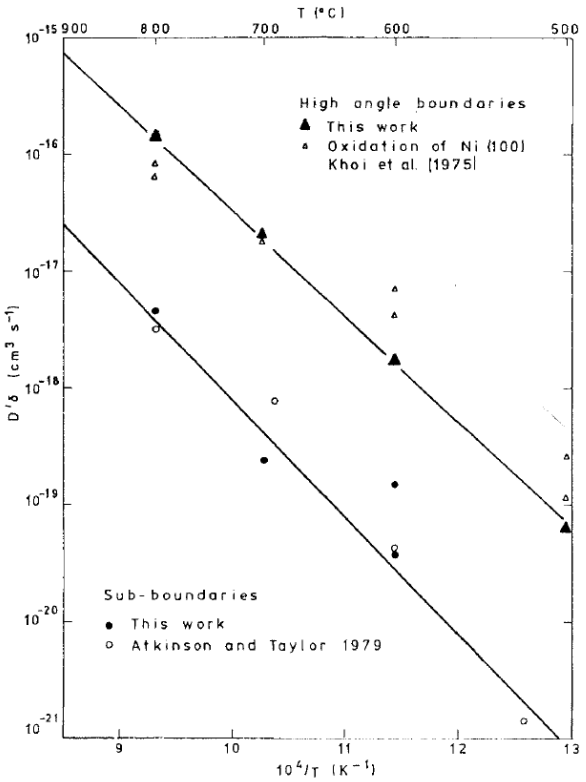

Figure 2.15: Arrhenius plot for diffusion in high angle boundaries and sub grain boundaries at P_{O_2} [132, 133]

energy associated with the reaction between the oxygen, and the respective metal [131]. After producing a continuous oxide film, the reacting species must travel through the oxide for further growth to occur [164].

Thermodynamic calculations have been used to show that the stable oxides on Ni-Al and Ni-Cr are Al_2O_3 and Cr_2O_3 , respectively, provided that there is more than 1ppm of aluminium or chromium [40]. Most nickel-based superalloys are based upon the Ni-Al-Cr system, as it simplifies the alloy chemistry; therefore, having a good thermodynamic model to describe the thermodynamics of Ni-Al-Cr helps to provide a good basis for how the system will respond. Additionally, this can be extrapolated to form a description for higher-element systems where there is a lack of experimental data [50]. The quality of thermodynamic data helps provide more realistic numerical models that can better predict real-world experimental results.

If the oxide is adherent and continuous, then oxide growth is governed by the diffusion of the reaction species via point defects. The driving force will be determined by the differ-

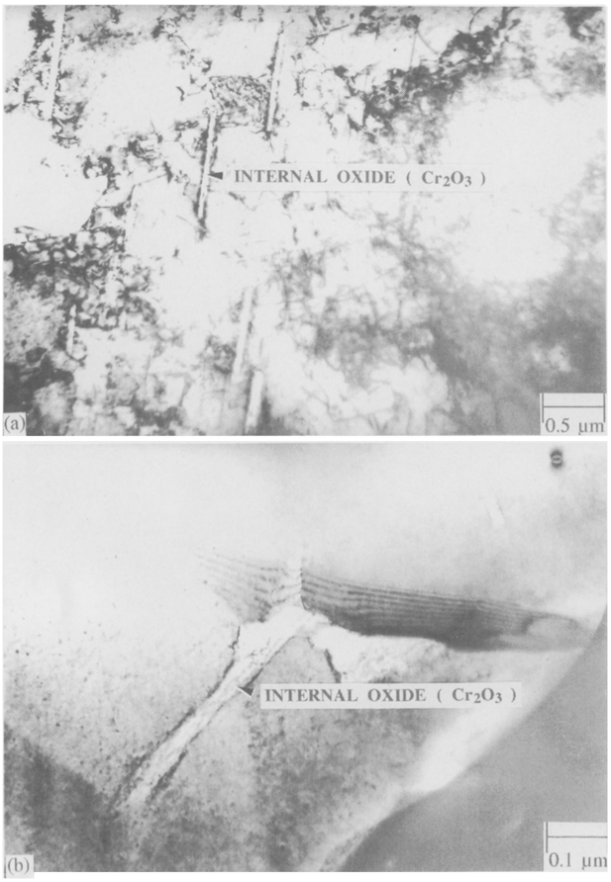

Figure 2.16: TEM trasnverse-section image of Ni-1at%Cr after 15 minutes of oxidation at 1273K showing (a) internal oxide particles and (b) internal oxide formation at the grain boundary of the metal substrate [157].

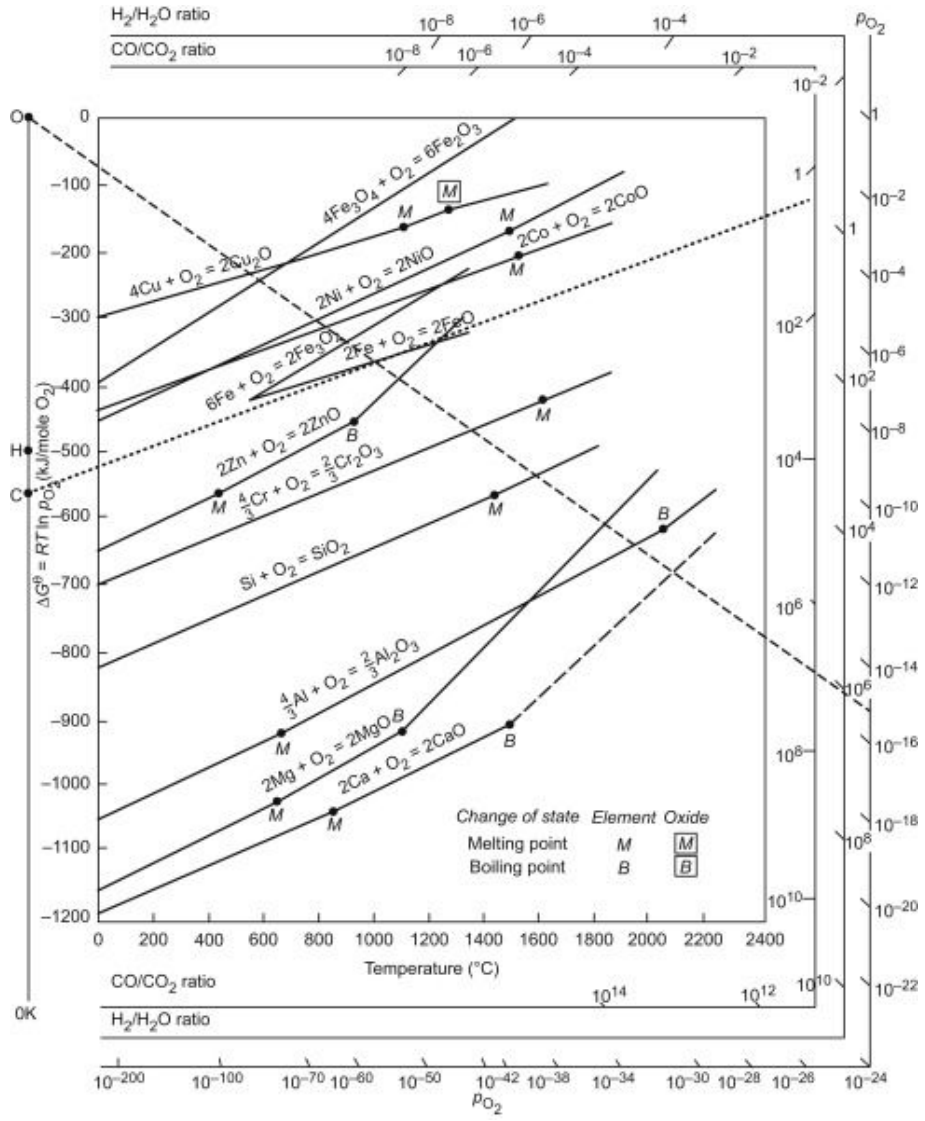

Figure 2.17: Ellingham Diagram showing free energies of formation for selected oxides as a function of temperature. Corresponding equilibrium p_{O_2} and H_2/H_2O and CO/CO_2 ratios. Dashed lines are for equilibrium oxygen concentration for Fe/FeO and for the same CO/CO_2 reaction [165]

ence in ambient pressure and the decomposition pressure of the oxide at the oxide-metal interface [164]. If the ambient pressure decreases to the oxide decomposition pressure, no gradient will be present, and the oxidation will stop [164]. The mechanism of oxidation scale stability is described by an Ellingham Diagram which is displayed in Figure 2.17.

2.1.5 Kinetics

Kinetics controls the oxide scale thickening process; oxides such as NiO, CoO and FeO have electrons that hop between divalent (2+) and trivalent (3+) cations; the variation in valency is related to the amount of oxygen ions in the oxide. The motion of electrons

is fast compared to the diffusion of divalent cations throughout the lattice, which forms new oxide [160, 166, 167]. As the rate of cation diffusion throughout oxides is rarely the same due to different affinities for oxygen; changing the rate of cation diffusion means that the kinetic rate equations are rarely followed. Not consistently following the kinetic rate equations results in an oxide composition changing in a complex way with respect to time [160]. Considering the formation of an oxide is shown in Figure 2.18; in the case where ,Figure 2.18(a), only element B alone forms an oxide; this produces internal oxide BO in a matrix A. Figure 2.18(b), minor element B oxidised forms an oxide on the surface of the material and depletes the concentration of element B in the bulk region. Figure 2.18(c), major element B oxidises alone and produces an oxide with particles of A matrix within the oxide BO. Figure 2.18(d), major element B forms an oxide on the material's surface and becomes depleted in concentration in the bulk region. Figure 2.18(e), elements A and B form a single oxide composed of various concentrations (A, B)O. Figure 2.18(f), elements A and B oxidise to form the oxide ABO_2 dispersed within the AO matrix. Figure 2.18(g), A and minor component B) oxidise to give insoluble oxides. Figure 2.18(h), element A and major element B oxidise to give insoluble oxides within an AO and BO matrix [160].

Oxide growth rates are typically parabolic; this was shown by Wagner in his original work [118]. Wagner solved Fick's first and second laws assuming that the flux of cations is proportional to their chemical potential gradients [168]. The parabolic growth curves can be used to determine the activation energy for the cation diffusion [96, 109, 118, 169–171]. By plotting the square of mass change against temperature, the gradient can be plotted against the reciprocal of temperature; the gradient of this line is the activation energy multiplied by the molar gas constant, R [150].In some experiments, the oxidation rate becomes sub-parabolic at temperatures below 1000°C [2].

2.1.6 Oxide Structure

Nickel and cobalt oxide structures are like that of NaCl and are found to be metal deficient at high temperatures, which is described by $M_{1-\delta}O$. This indicates that there is a move away from stoichiometry within the metal sublattice [2, 111, 172, 173] for nickel the

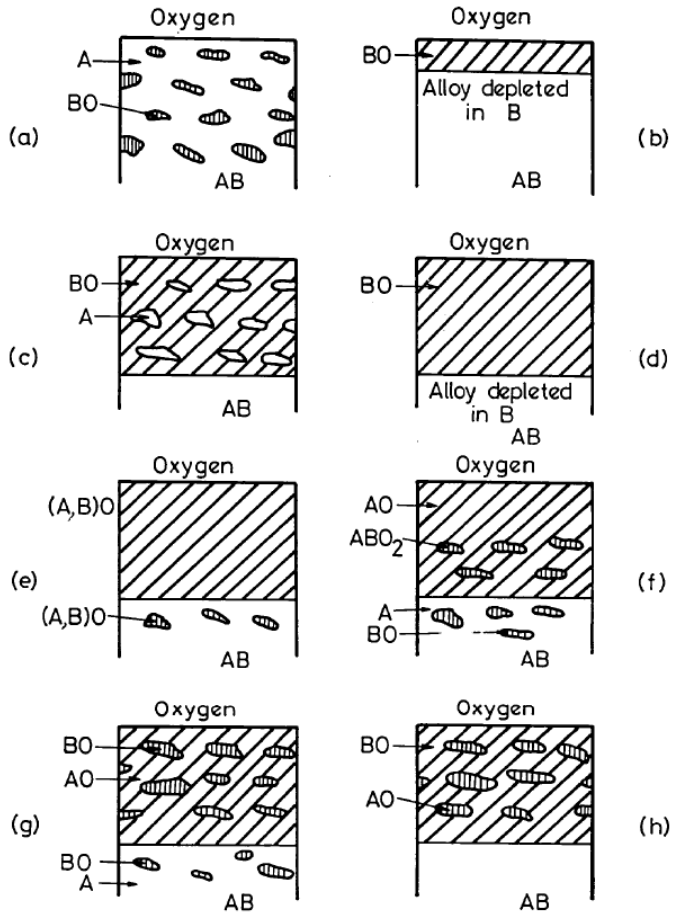

Figure 2.18: Schematic showing the different oxide structures that can form from the alloy AB where b is the less noble metal [160].

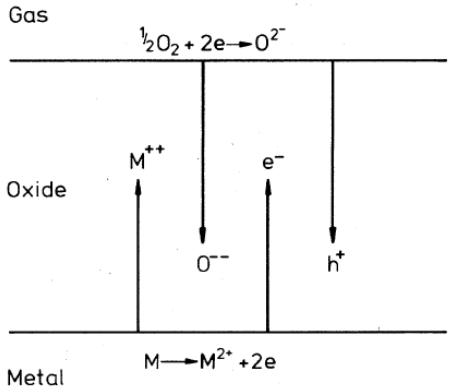

Figure 2.19: Transport of ions and electrons across a growing oxide film [118].

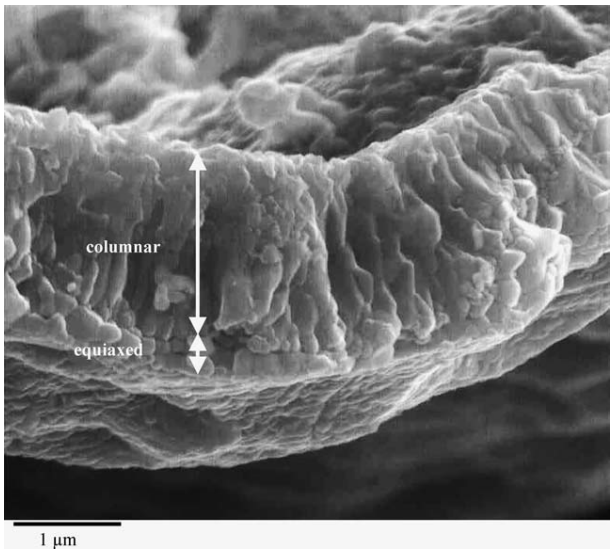

Figure 2.20: SEM fracture cross section of NiO scale formed during 12hr at 800°C in air under atmospheric conditions [166].

value of δ is of the order 10^{-3}-10^{-4} which is approximately 10^{-1}at% [2, 174]. This non-stoichiometry results from the oxygen partial pressure, which is in equilibrium with the oxide [173, 175]. To maintain charge balance there are cation defects (*i.e.* Ni^{3+}) [176, 177]. For nickel, under most operating conditions, NiO is the only stable oxide present, the other two oxides (Ni_2O and Ni_3O_4 are transitional) [172, 178]. A single stable oxide provides simplifications for understanding the oxide and the oxidation rate.

Oxides on a nickel-based superalloy tend to be single or multiple phases which are interpreted to be stoichiometric oxides and consist in addition to NiO as corundum Cr_2O_3 and Al_2O_3, and spinel $NiCr_2O_4$, there are some solute elements present. However, these are within thermodynamic solubility limits [60]. Oxides which form on a metal substrate consist of two layers; the difference is their grain structure. The inner layer grains are equiaxed, and the outer layer is made up of columnar grains which are perpendicular to the surface of the oxide shown in SEM images of oxides in Figure 2.20 [2, 131, 134, 179, 180]; which validates the "grain boundary sweeping" oxide grain growth mechanism. The formed oxide structure is temperature dependent; at lower temperatures, the structure is more equiaxed with occasional platelets and whispers. At higher temperatures (700-900°C), ridges form at the surface, and above 1000-1100°C facetted NiO grains dominate the surface morphology [2] as the temperature increases, grain boundaries become clearer and more distinct [181].

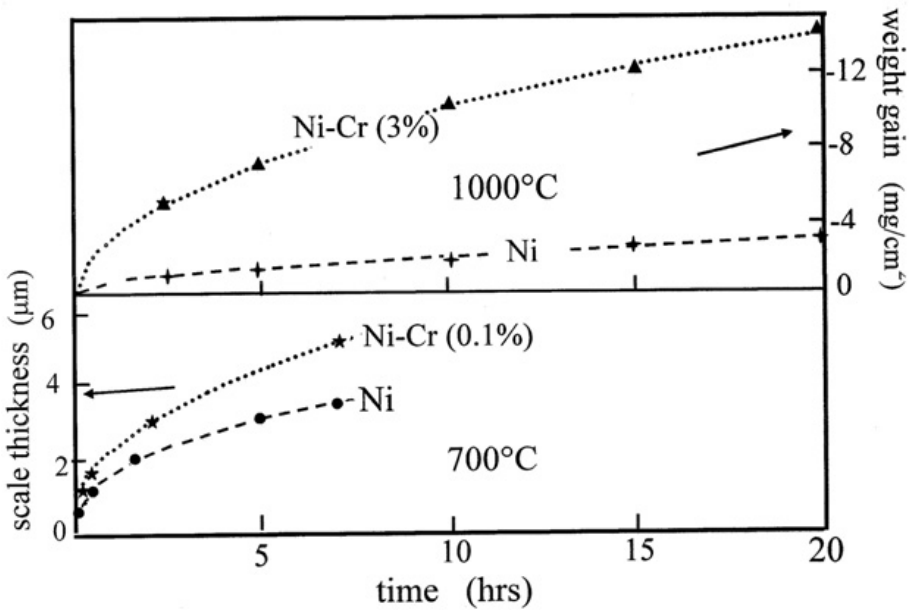

Figure 2.21: Isothermal weight gain versus time for Ni and Ni-3wt% Cr at 1000°C and oxide scale thickness for Ni and Ni-0.1wt%Cr at 700°C [116].

The substrate and oxide grains' orientation play a crucial role in oxidation. Certain orientations of oxide grains grow faster than others [147]. The initial oxide grain boundary orientations are random. The grain orientations are selectively chosen as the oxide grows due to their different growth rates. The preference for certain grain orientations may be why thin oxide films are more uniform, as the predominant oxide grains have not yet been selected [2]. The different nickel oxide grain orientations have different growth rates at different temperatures [125, 181]. This effect on growth rate implies that the temperature at which the samples are oxidised has a bearing on the grain structure of the formed oxide.

Porosity within an oxide decreases as the oxygen pressure increases; additionally, the morphology of the pore changes with the oxygen pressure. Low ambient oxygen pressure forms pores that coalesce to form macro-pores parallel to the oxide-alloy interface. At higher oxygen pressures, the pores are uniformly transported outwards through the scale and eliminated from the oxide [155, 158].

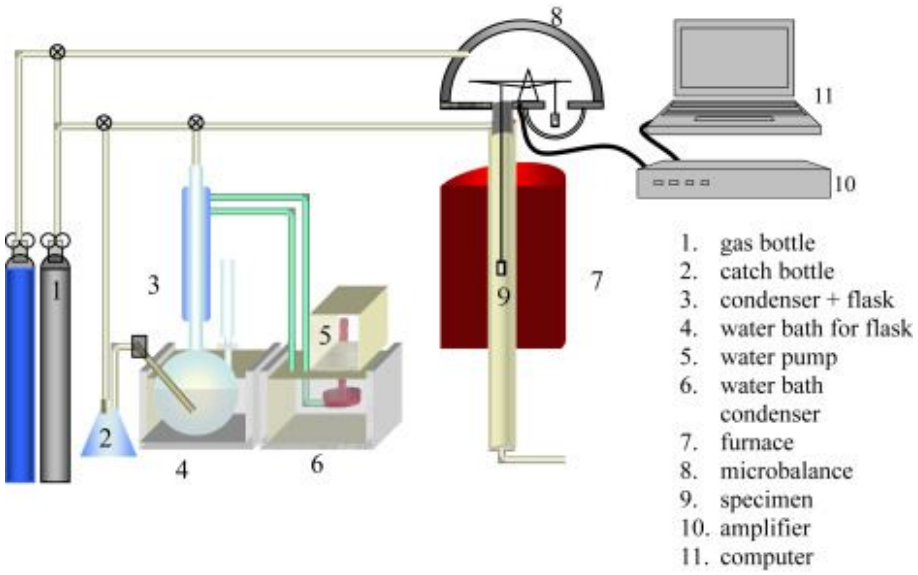

Figure 2.22: Thermogravimetric analysis equipment for measuring mass increase during oxidation [182].

2.1.7 Measurement Techniques

The techniques for measuring the oxidation rate are based on measurements of the oxidation thickness or mass gain during oxidation. Simply this can be weighing or measuring the oxide thickness after fixed periods. Advanced equipment is available to measure the weight gain many times a minute to provide a more detailed look at the oxidation rate. As the weight gain of interest is small, a sensitive balance is required to provide enough detail about the sample's weight gain. The equipment commonly used is thermogravimetric, which measures the weight increase during high-temperature oxidation using a microbalance within a controlled gas atmosphere (c.f. Figure 2.22) [2, 152, 182]. If the oxidising atmosphere is highly corrosive, the use of an expensive microbalance is undesirable; therefore, the elongation of a helical spring is observed to determine how the sample gains mass. The spring for such a spring balance is usually made from silica fibre (c.f. Figure 2.23) [182].

Secondary Ion Mass Spectroscopy (SIMS) is used to measure the concentration of atoms at local points; a common example in oxides is to measure the oxygen concentration within an oxide [2, 5, 173]. An ion beam is used to sputter the surface of a sample, and the ejected ions are measured via mass spectrometry. The sputtering is continued to reach deeper regions of the oxide layer [182]; Figure 2.24 shows a SIMS profile for iron oxide showing

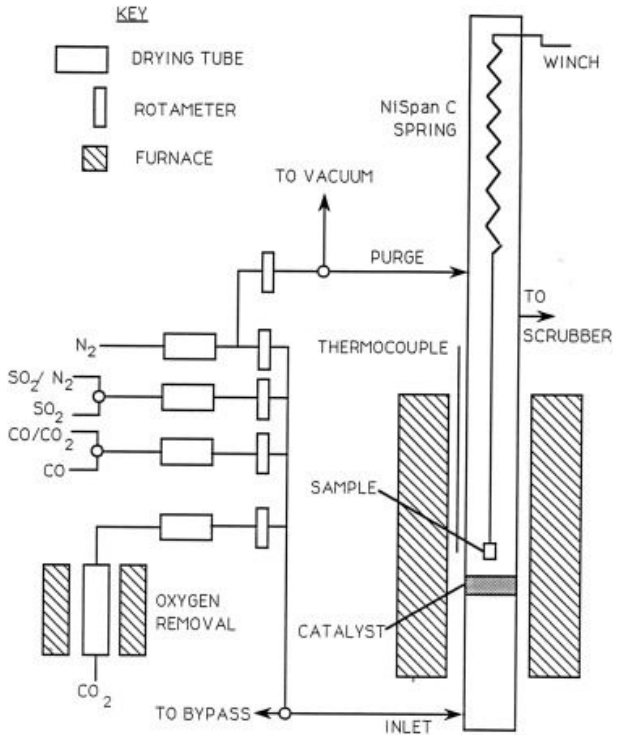

Figure 2.23: Spring balance for measuring high temperature oxidation kinetics [182].

concentration against depth. As SIMS measures different masses, isotopes of diffusing species can be measured and used to determine their ingress rate. This technique can give an idea of the mechanisms behind the oxidation process [2]. If a radioactive trace is used, the radioactive isotope needs to have a sufficient half-life for the time scales of oxidation [173]; this allows sufficient time for the measurements to be taken before the isotopes have decayed.

2.1.8 Stresses in Oxides

As the material is oxidised, the molar volume of the oxide is usually different from that of the metal. The difference in molar volumes causes stress resulting from the expansion or shrinking of the material. After oxidation, this stress leads to a matrix mismatch [183]. The Pilling-Bedworth Ratio can describe this matrix mismatch (PBR) [56]. This matrix mismatch led to Pilling and Bedworth suggesting that the ability of a metal to form a protective oxide scale could be related to the ratio of the molar volume of the oxide and metal [109],

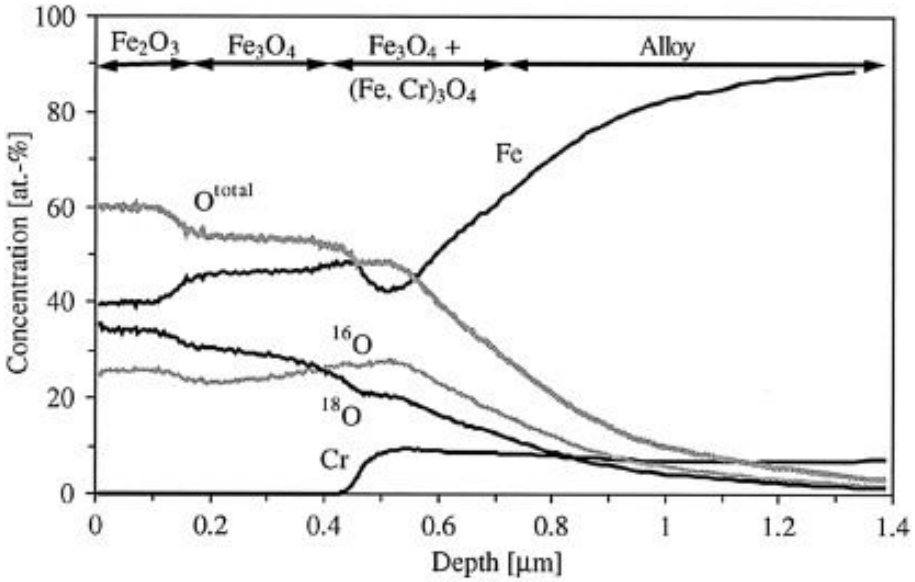

Figure 2.24: SIMS analysis of an oxide grown on Fe-9Cr steel in an oxidising atmosphere of N_2-1%$^{16}O_2$-2%$H_2{}^{18}O$ [182].

$$PBR = \frac{V_{metal}}{V_{oxide}} \tag{2.4}$$

If the PBR is less than one, it indicates that insufficient oxide is formed to cover the surface of the metal. If the PBR is much larger than one, it indicates that too much oxide is formed and thus will result in cracking and spalling [56]. Therefore the ideal ratio is where it is close to one for the formation of protective oxide scales [23], a table of different PBR values is in Table 2.2. It is important, however, to note that this only holds for some oxide formers and is, therefore, insufficient to describe the protective nature of oxide formers [23].

Table 2.2: the PBR for common metals [56]

Oxide scale	Oxide–metal volume ratio
MgO	0.81
Al2O3	1.28
ZrO2	1.56
Cr2O	1.64
NiO	1.65
FeO	1.68
TiO2	1.70–1.78
CoO	1.86
Cr2O3	2.07
Fe3O4	2.1

2.1.9 Failure of Oxides

The heating of a metal with an oxide is important for materials that will be thermally cycled as there is a mismatch in the thermal expansions; they expand at different rates. The mismatch in thermal expansions can result in the oxide spalling, thus leaving the surface bare for oxidation to occur; known as spallation [63, 68, 71, 123]. Residual stresses are usually compressive, which results in delamination and cracking of the oxide leading to spallation. The oxide scales resistance to spallation is used as an indication of its protectiveness [123]

2.1.10 Barrier Coatings

Design choices for what to prioritise within material design have increased creep and fatigue strength at the expense of oxidation resistance. To improve the oxidation resistance of materials, barrier coatings are applied to the surface [62, 184–186]. These coatings apply a protective property to the surface of the material. Coatings can increase the wear resistance, oxidation resistance or reduce the temperature for the in-service component.

Barrier coatings are applied to the surface of a material to promote a more protective surface that allows a more extreme operating environment [185, 187–189]. Figure 2.25 shows a SEM image of barrier coatings which are commonly applied to single-crystal nickel-based superalloys consisting of a metallic bond coat and a top coat [185].

The metallic bond coat is present to reduce the lattice mismatch stress from thermal expansion between the substrate and the top coat and therefore improve their adhesion [18, 190]. The ceramic layer in YSZ-based systems cannot prevent oxidation of the substrate [29]. These bond coats consist of materials like nickel aluminides, which have good thermal stability and a high melting temperature, around 1640°C [27, 62, 191]. Adding platinum into aluminium bond coats was discovered to significantly reduce the aluminium diffusion rate and improve the oxidation resistance. The reduction of aluminium diffusion occurs by enhancing the selective oxidation of aluminium that provides a purer oxide, and a slower growth rate [192, 193]; Figure 2.26 shows the reduction in oxidation rate for platinum

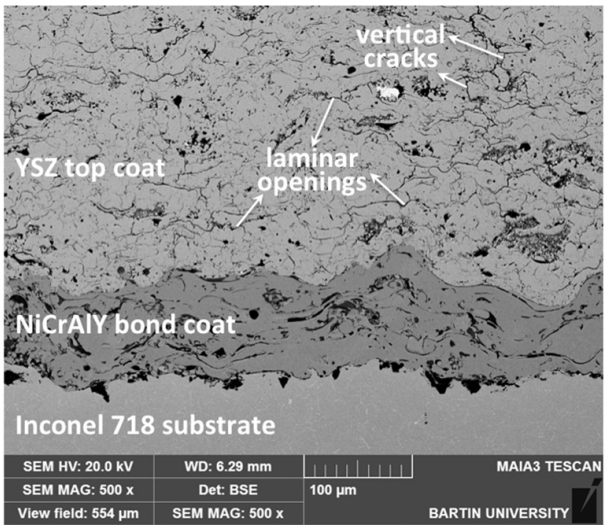

Figure 2.25: Cross-sectional microstructure of as-sprayed TBC system [185].

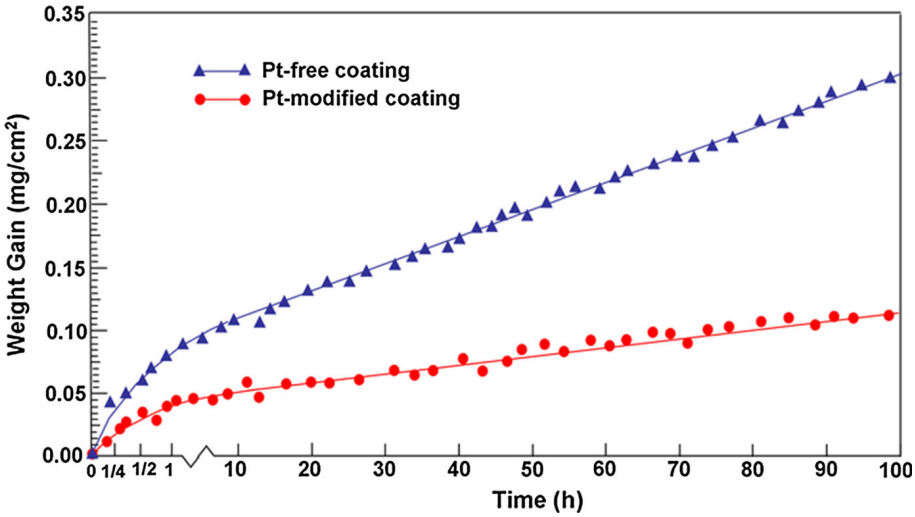

Figure 2.26: Oxidation rates of Pt-free and Pt-modified coatings during isothermal exposure at 1150°C in air [193].

modified coatings compared to platinum free coatings. The platinum concentration profile through the bulk metal is an indicator of thermal stability for the barrier coating; the more uniform concentration, the less thermally stable the barrier coating becomes [194]. Adding some reactive elements, such as silicon, can improve the oxidation resistance; this occurs by increasing the activity of aluminium which promotes the oxidation of aluminium, and subsequently the adherence of the oxide scale [62].

MCrAlY coatings have a large amount of chromium and aluminium to provide sufficient oxidation resistance that ensures the substrate is well protected; the small addition of a reactive element, such as yttrium, helps to improve the adhesion of the formed oxide scale [9, 185, 195]. M refers to nickel, cobalt, or both [9, 46, 193, 195, 196]. MCrAlY overlay

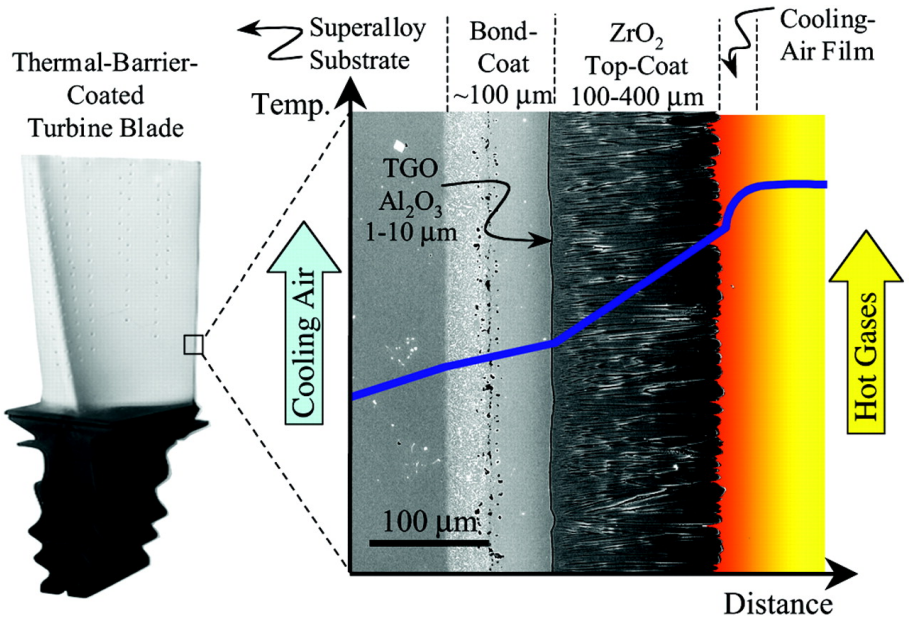

Figure 2.27: Cross-sectional SEM of an electron beam physical vapour deposited TBC super imposed onto a schematic showing the temperature reduction provided by the TBC [198].

coatings are widely employed in hot sections of gas turbine engines in the aerospace and power generation industries. The use of coatings is for high-temperature oxidation and hot corrosion protection. These coatings thermally grow protective alumina scales with high thermodynamical stability, good compactness, and a slow growth rate [197].

The top coat can take the form of several different materials systems; the material system is present to reduce the temperature that the substrate material experiences. One of the main materials is a ceramic top coat referred to as a Thermal Barrier Coating (TBC). These TBCs allow turbine blades to reach temperatures of 1500°C by providing thermal insulation for the metallic substrate resulting from the low thermal conductivity [46, 188, 189, 195, 198]; Figure 2.27 schematically represents the temperature from the atmosphere and to the bulk metal. Adding a TBC can reduce the blade surface temperature by $100-300$°C . Modern TBCs systems consist of an internal metallic bond coating and another ceramic layer. The bond coat helps to provide oxidation protection for the superalloy and promotes the adherence of the TBC to the substrate [199].

Aluminide coatings are applied to nickel-based superalloys to provide protection where conventional nickel-based superalloys cannot properly function. Aluminide coatings are applied to form a stable and continuous α-Al_2O_3 scale that can act as a protective barrier

to control the mutual diffusion of the alloying elements and corrosive species [62]

The durability and longevity of barrier coatings are critical for extending the service life of components; if a coating fails, the material will likely fail rapidly [189]. There are several different mechanisms by which barrier coatings can fail; thermal shock; due to a mismatch in thermal expansion [200]; mechanical fatigue, a partial stress over-load during service, and the growth of the substrate [32, 49, 201] or bond coat [202]. Oxidation of the substrate or bond coat is the leading cause of TBC failure [185, 187, 201].

2.2 Modelling

Multiscale modelling approaches are widely applied to the theory, analysis and experimental prediction of structural materials at an atomistic level. There is an increasing reliance on powerful modern computation techniques, which can avoid the drawbacks of time and cost from traditional trial and error methods. Various computational methods are applied to simulate microstructure evolution, such as first principles, Monte Carlo, molecular dynamics, and phase field method [203].

2.2.1 Wagners Model

All current present-day understanding of oxidation results from work initially done by C. Wagner [102]. Wagner assumed that the diffusion of cations causes oxidation along short-circuit diffusion paths, and there is limited diffusion of anions [118, 168, 204]. The thermodynamic model Wagner developed was based on irreversible thermodynamics [109, 168, 205]. The principle of irreversible thermodynamics is that the independent migration of ions and electrons is proportional to its gradient within chemical potential but is also independent of the gradients of other species [109]. Wagners oxide growth equation is;

$$X^2 = k_p t \tag{2.5}$$

where X is the film thickness, k_p is the parabolic rate constant. The parabolic rate constant

is constant with the growth of oxide being controlled by transport along a gradient of the driving force

$$\frac{dX}{dt} = \frac{k_p}{2X} \tag{2.6}$$

Wagner's theory is based upon the slowest diffusion within the oxide and, therefore, the rate-limiting step [118].

2.2.2 Micro-Scale Models

Modelling has become an attractive way that experimental results can be coupled with predictive techniques. The large range of powerful and reliable modern computing can avoid the drawbacks of time-consuming and costly "trial and error" methods. These modelling techniques are diverse and aim to simulate the evolution of atomistic movements and interactions; the models are [203]; first principles [206], Monte Carlo [207], Molecular Dynamics [208].

Most modelling techniques are suitable for simulating the micro-scale evolution of oxides; these simulations are computationally intensive and unable to simulate oxidation over long periods. Therefore, simulations capable of running over a long time scale for large and complex simulation domains are desired. To provide results in a numerically efficient manner, this needs to be performed at a macro-scale evolution; sufficiently large simulation domain, which limits the use of techniques such as Monte Carlo [209], Molecular Dynamics [209], and DFT [209].

2.2.3 CALPHAD

In the CALculating PHAse Diagrams (CALPHAD) method, each phase in a system is modelled with a separate Gibbs energy expression which is a function of its constitution, temperature and pressure [50, 103]. These models are fitted to many different kinds of experimental and theoretical data. Sublattices can describe long-range ordering for when

atoms are on different lattice sites. When the same atom can occupy different types of sites, there can also be short-range ordering; this is something which is challenging to describe [103]. There is an explicit Gibbs energy expression that is used for CALPHAD models;

$$G_M^{\alpha} = {}^{srf}G_M^{\alpha} - T{}^{cfg}S_M^{\alpha} + {}^{E}G_M^{\alpha} + {}^{phys}G_M^{\alpha} \tag{2.7}$$

where α is the phases, ${}^{srf}G_M^{\alpha}$ is the surface of reference relative to other phases but also for internal ordering, T is the temperature ${}^{cfg}S_M^{\alpha}$ is the configurational entropy, ${}^{E}G_M^{\alpha}$ is the excess Gibbs energy, and ${}^{phys}G_M^{\alpha}$ is the contribution to the Gibbs energy due to specific physical phenomena like ferromagnetism [103]. The substitutional regular solution model for a multi-component system is defined as;

$$G_m = \sum_i {}^{\circ}G_i x_i + RT \sum_i x_i \ln(x_i) + {}^{E}G_m + {}^{phys}G_m \tag{2.8}$$

where x_i is the mole fraction of component i, ${}^{\circ}G_m$ is the Gibbs energy of component i relative to the same standard state, and $x_i \ln(x_i)$ is the ideal entropy of mixing [103]. The "$\circ$" symbol denotes a pure component that may depend on temperature and pressure but not composition.

The excess Gibbs energy generally will contain multiple terms that depend on composition and temperature; the composition dependence is a series of expansions of the phase constitution [103]

$${}^{E}G_m = \sum_i \sum_{j>i} x_i x_j (L_{ij} + \sum_{k>j} (L_{ijk} + \cdots)) \tag{2.9}$$

The use of mole fraction is not enough to describe multiple sublattices; therefore, a composition variable for the different constituents on a sublattice is used - site fraction; $(y_j{}^s)$, where j specifies the species and s the sublattice. The use of mole fractions is not suitable for the case where a species can sit on multiple sublattices; this is where site fractions

become more attractive as they give an idea of the compositional spread over the different sublattices [103].

2.2.4 Compound Energy Formalism

The compound energy formalism (CEF) approach has been developed from the CALPHAD approach after the concept of lattice stability to describe the whole composition range for substitutional solutions [210]. The concept of 'compound energy' plays the same role for solution phases with sublattices as 'lattice stability' plays for substitutional solutions [210].

The CEF started initially as a purely mathematical method that analytically expressed the Gibbs energy using terms of increasing powers for the mole fractions of atoms within the individual sublattices ('site fractions') [103, 210]. Random mixing was assumed to be taking place within each sublattice. The CEF is an extension of the regular solution model with higher order terms that reduce when all the sites in all but one of the sublattices are vacant [210].

The CEF was constructed as a model to describe the thermodynamic properties of phases which were composed of two or more sublattices where there is a variation of composition *i.e.* $(A, B)_k(D, E, F)_l$ where A and B only mix on the first sublattice, and D, E and F only mix on the second sublattice. The subscripts k and l are the stoichiometric coefficients [210]. In the limit where there are only one species on each sublattice, the stoichiometric compounds are thus "end-members of the solution phase", commonly simplified to "end-member compounds", *e.g.* A_kD_l, for simplicity, these are written as $G_{A:D}$ [210]. For a two sublattice system, the CEF can be written in the form of a substitutional solution model;

$$G_m = \sum_{ij} y_i y_j G_{i:j} + RT \sum_s a^s \sum_i y_i^s \ln(y_i^s) + {}^E G_m \tag{2.10}$$

where G_m is the Gibbs free energy for one mole of material, y is the site fraction of the species i or j, and any excess terms ${}^E G_m$ [103, 211].

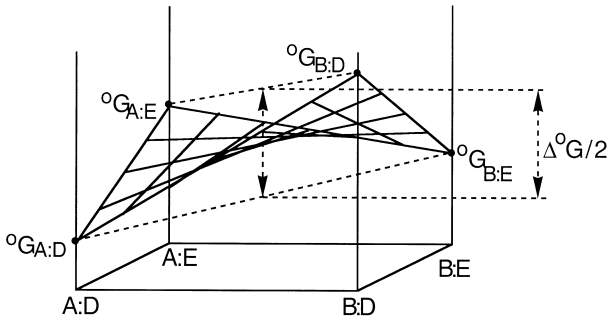

Figure 2.28: Surface for the Gibbs energy of a phase $(A, B)_1(D, E)_1$ for the CEF [210].

Equation 2.10 describes an energy space for the system, where the corners represent the end member energies; for a simple two-element on two sublattice mixture, all possible compositions may be represented on a square; this is a "composition square" represented in Figure 2.28.

The chemical potential for an element can be determined by;

$$\mu_i = G_m + \frac{dG_m}{dy_i} - \frac{1}{a^s}\sum_j y_j \frac{dG_m}{dy_j} \tag{2.11}$$

this considers the contribution not only the energy of the one element of interest but also the other elements within the system [210].

2.2.5 Phase Field

A powerful technique for modelling has proven to be suitable for modelling a vast range of different systems as it can treat arbitrarily complex interface shapes with minimal mathematical complexity [212]. Phase field models are powerful as they are derived in a thermodynamically consistent way; this allows them to be used with proper thermodynamic variables but does not deal with individual atom's behaviour [93, 203, 213–215]. The thermodynamic data commonly comes from CALPHAD assessments of real-world systems [216, 217]. Additionally, there is no need to explicitly track the interface due to a phase variable applied over the entire simulation domain [215, 218–220].

The phase variable is used to determine what phase is present within the system; there are two possible options; 0 and 1 or -1 and 1. This is made up of two different equations,

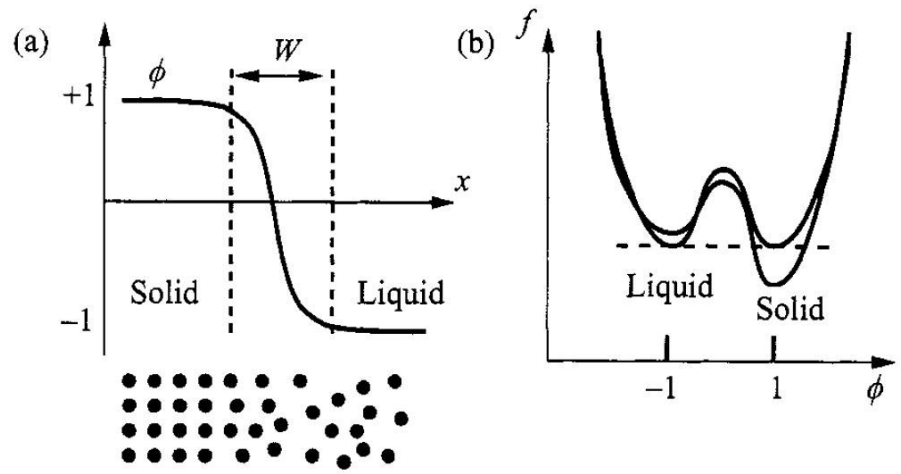

Figure 2.29: Schematic representation of a phase field profile (a) and the double well potential (b) [221].

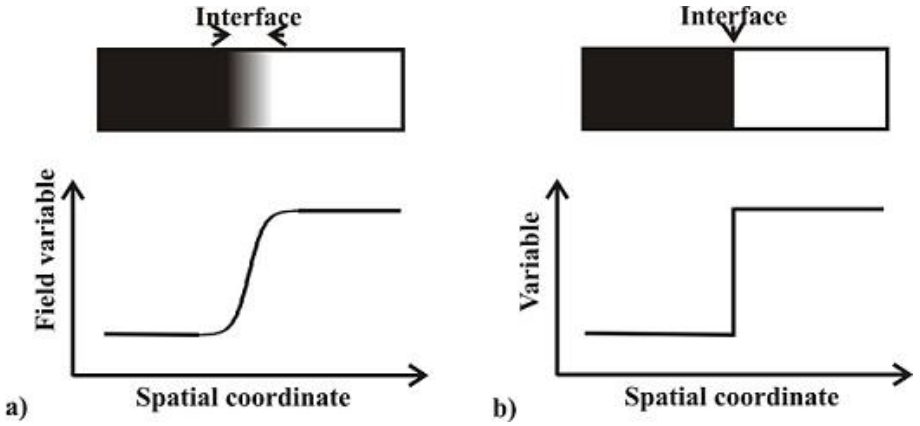

Figure 2.30: Comparison between (a) diffuse interface and (b) a sharp interface [215]

the double well potential [221] shown in Figure 2.29; and the double obstacle potential respectively.

The foundation of the phase field model can be traced back to work done by Van der Waals, who modelled a liquid-gas system with a density function and classified the interface as diffuse. The diffuse interface was rationalised as more natural than a sharp interface [104, 213, 219, 222, 223], through Van der Waals investigations of the density during a phase change between liquid and vapour [219].

Phase field models were initially developed to describe the microstructure of a solidified metal. The phase field model considers both the composition structure and additionally the structural domains and the interfaces; this is done by using a set of phase variables; these variables are continuous over the whole domain [224]; the result of this is that the interfaces within a phase-field model are diffuse, these interfaces do not need to be

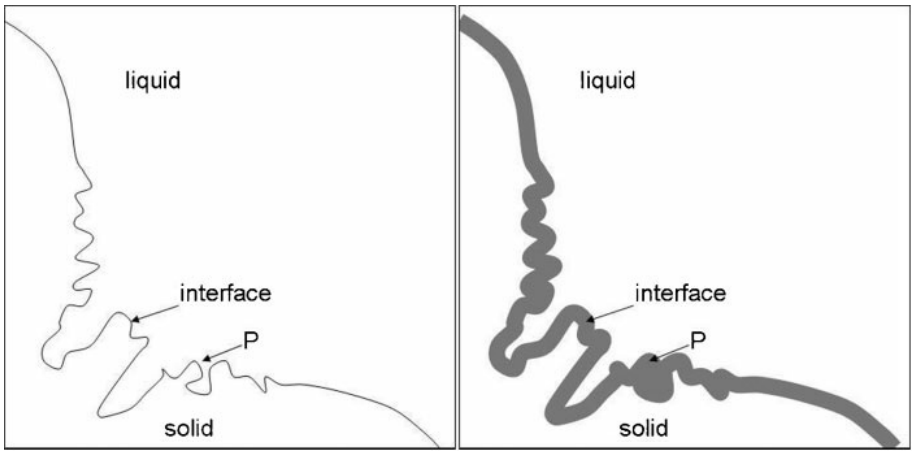

Figure 2.31: Schematic showing the loss of detail due to a wide phase interface value [228].

explicitly tracked [215, 219, 220]. Figure 2.30 compares a diffuse interface with a sharp interface, showing how the phase changes over distance [93, 105, 215, 225, 226]. The interface width needs to be sufficiently large; the wider the interface, the smaller the gradient energy contribution over the interface, but it can result in the loss of detail and include unphysical interactions between different interfaces [213, 227, 228]; Figure 2.31 shows how certain interfaces become hidden by the diffuse interface.

Phase field models have a similar form to the Allen-Cahn equation;

$$\frac{\partial u}{\partial t} - \Delta u + f(u) = 0 \tag{2.12}$$

where u is the order parameter and t is the time step. These equations apply to the simulation domain, providing transformation to the parameter of interest.

Initially, applications of the phase field model were primarily limited to materials science with applications in; solid-state phase transformations, recrystallisation, γ' rafting [104], and grain growth [105, 227]. Phase field models were initially developed for modelling the growth of solidification [229, 230], and there remains a large area of interest in this area [231]; with other material science properties modelled such as fracture and fatigue, [106]. The phase field modelling technique has been gathering interest from other research areas; such as biology [225] and medicine, where it is used to model the growth of tumours, vesicle-fluid interaction, and fluid-structure interaction problems [232], simulating the

propagation of wildfires [233].

As computational power increases, the ability and scope for numerical models to produce higher quality and detailed results. More detailed and more thermodynamically consistent results can be achieved by considering more variables in numerical models. The inclusion of more elements or physical parameters provides a model capable of being more able to represent real-world systems. Models that consider multiple elements and multiple phases are suitable for modelling the interface reaction of multiple elements is known as the multi-phase-field model [234] this technique introduces a series of fields which represent the materials properties of interest and are used to identify the local phase present [222]. These fields can describe more material properties or multiple phases influencing the microstructure evolution.

2.2.6 Phase Field Oxidation Models

A phase field model simulating oxidation is computationally complex. Many current oxidation models focus on the diffusion of oxygen into the substrate and are based on oxygen concentration in the oxide as a field variable [183]. For a phase field model to accurately model the growth of an oxide, the model would need to include an elastoplastic creep model [235]. Due to oxidation occurring via short circuit diffusion paths, a phase field model capable of modelling grain boundaries is required [183]. Further complexity comes in the availability of thermodynamic and mobility data [212, 213], certain oxide phases are considered stoichiometric and are not compatible with the commonly used diffusion equations [212].

Guyer has produced a general formulation of the phase field model for electrodeposition and electro-dissolution [236, 237]; however, this approach includes the details of charge distribution at the interface and is limited to use within nanometer scale systems [238].

Guyers electrodeposition and electro-dissolution model has been adapted to describe oxidation in a phase field consistent manner. The computational model is very difficult to simulate in more than one dimension because the equations for evolution are stiff [97].

The model was implemented in MOOSE (Multiphysics Object Oriented Simulation Environment) to improve the computational cost of running the simulation, allowing for massively parallel finite element simulations. The system was defined with $\phi = 0$ as being for the oxide and $\phi = 1$ for the bulk phase.

The rate of concentration change within this model is defined as;

$$\frac{\partial c_i}{\partial t} = -\nabla J_i = M_i \nabla^2 \bar{\mu}^0 \text{ for } i = v, e \tag{2.13}$$

This model simulates the motion of defects of anion vacancies and electrons, where the ^{0} denotes the oxide phase. The diffusion flux across the oxide is assumed to be constant in one dimension; this thus simplifies the chemical potential gradient as being $\frac{\Delta \bar{\mu}_i^0}{L}$ where L is the location of the interface. The energy of the system is defined as being;

$$\mathcal{F}(\phi, c_v, c_e, \psi) = \int \left[G^{\phi} + G^{tot} + \frac{1}{2}\psi\rho^s \right] dV \tag{2.14}$$

where ρ is the charge density, simulations were run for thick and thin film limits, a thick film was defined as being $> 1\mu$m, and the thin film was defined as being $\sim \mathrm{L_D}$. Where $\mathrm{L_D}$ is the Debye length

The profiles of vacancies and electrons across the interface for a thick and thin film are shown in Figure 2.32, within the thin film limit the concentration-dependent mobility ($\mathrm{M_i(c_i) = M_i c_i}$) leads to a small difference in the defect concentration and electrostatic profiles. Within the thin film limit, Figure 2.32e shows the vacancy concentration is no longer non-linear, which results in a lower flux near the interface.Figure 2.32f shows the velocity of oxidation is compared to oxidation that proceeds via a fixed rate constant [97].

In order to further improve understanding of how rough surfaces are absorbed into the oxide, simulations are run and compared in Figure 2.33. The profiles are shown for the flat Figure 2.33(a) and rough Figure 2.33(b) surfaces, the non-dimensional concentration profiles of vacancies and electrons Figure 2.33(c) and the electrostatic potential

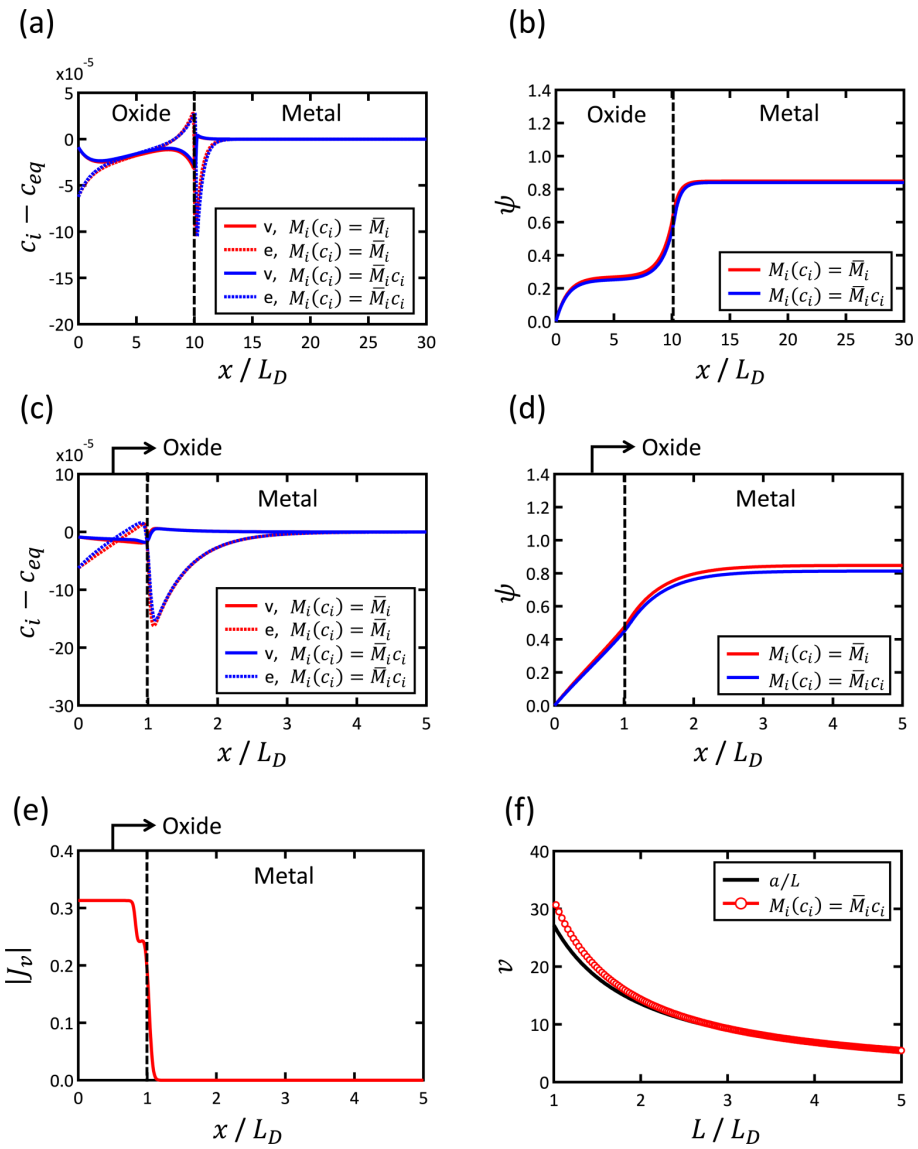

Figure 2.32: Concentration profiles of vacancies c_v and electrons c_e relative to c_{eq} in the thick (a) and thin (c) film limit. The electrostatic profiles are shown for the thick (b) and thin (d) film limit. The diffusional flux of vacancies versus distance in the thin limit (e). Dimensionless oxidation velocity verses oxide film thickness (f), the black curve is for a parabolic growth rate with a fixed rate constant assumption [97].

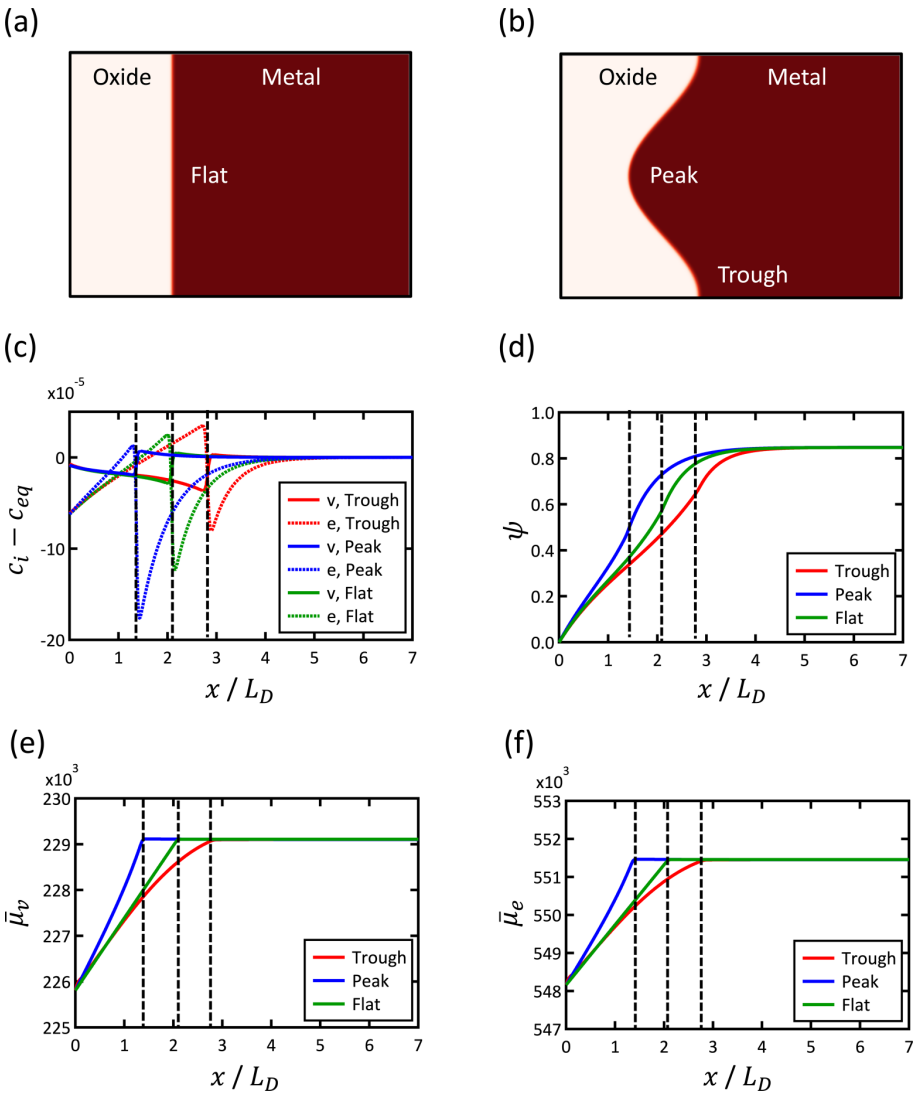

Figure 2.33: Schematics of a flat (a) and rough (b) surface. The non-dimensional concentration profiles of vacancies c_v and electrons c_e relative to c_{eq} (c). The electrostatic potential (ψ) profiles, electrochemical potential (μ_i) (d). Vacancy (e) and electron (f) profiles across the trough and peak of a curved surface and a flat interface. The dotted lines represent the location of the oxide-metal interface (where $\phi = 0.5$) [97].

Figure 2.33(d).

This modelling approach is limited in its respect as the defect concentrations are considered; this limits the model's applicability for studying more complex alloy structures. Its reliance on MOOSE to enable the simulation to run within a reasonable computational time also limits the expansion of such a model to more dimensions and higher order systems; the computational time is not stated by Kim et al. [97].

Chapter 3

Simulating the Growth of Chemically Ordered Phases

3.1 Introduction

Fick's diffusion equations can describe the simulation of how concentration gradients can modify an alloy's composition. The first law postulates that flux is proportional to the concentration gradient, so material transfers from high concentration to low concentration [182, 239]. Fick's diffusion equations are a simplification of how mass travels within a material, the gradient for mass travel is via a concentration gradient; this is not always applicable, as Darken proved during his experiments on a ternary system [240] whereby carbon diffused up the concentration gradient in the presence of silicon.

$$J = -D\frac{\Delta C}{\Delta x} \tag{3.1}$$

where J is the diffusion flux, D is the diffusivity, C is the concentration, and x is the distance over which the diffusion occurs. The second diffusion law predicts how the concentration changes over time; in one dimension, it is [239]

$$\frac{\delta C}{\delta t} = D\frac{\partial^2 C}{\partial x^2} \tag{3.2}$$

where t is time, these equations describe how elements move based on concentration gradients. Such techniques are helpful as they can provide information on the degree of segregation or heating cycles to equilibrate the solute segregation [241–243], through driving towards local equilibrium [244–246], the drive towards local equilibrium is used by DICTRA [241, 247]. Such techniques can explain how fast an interface moves based on the motion of elements and how fast a phase transformation occurs within the material [243, 247]. These techniques cannot model reactions as thermodynamics and kinetics are not natively considered.

Analytical models exist for modelling how a precipitate phase may grow, the most common being the model developed by Zener [248].

$$Z = \alpha_1 (Dt)^{\frac{1}{2}} \tag{3.3}$$

where Z is the thickness of the precipitate, D is the diffusivity coefficient, and t is the time since the region began. α_1 is a prefactor for the 1-dimensional case and is

$$\alpha_1 = K_1 \frac{n_\infty - n_1}{(n_0 - n_\infty)^{\frac{1}{2}}(n_0 - n_1)^{\frac{1}{2}}} \tag{3.4}$$

where n_∞ is the composition in the bulk and is unperturbed by the reaction, n_1 is the composition just in front of the interface and n_0 is the composition of the interface, K_1 varies slowly from 1.13 to 1.41 as n_∞ varies from n_1 to n_0 [248].

This model is simple and gives a general idea of how quickly the interface can grow but is limited as it does not consider the availability of elements to react; it works on the assumption that the bulk phase is sufficiently large and unperturbed by the reaction.

This work seeks to build on the numerical models of Fick's diffusion by adding a reaction-based interface approach to enable such techniques and models to become more suitable

for modelling how chemically ordered phases grow. As the growth of cementite is well documented and there is a greater understanding of simulating iron processes, the growth of cementite will be modelled to provide an understanding of how well this technique can simulate the growth of chemically ordered phases.

3.2 Methodology

3.2.1 Model Description

A numerical model suitable for modelling the growth of chemically ordered (stoichiometric) phases is developed; the numerical procedure is an adaptation of standard Fickian diffusion. The complexity of producing a model capable of simulating chemically ordered phases ensures that the correct composition of different elements moves between the phases of interest. The interface reaction can be described as a chemical reaction;

$$mA^{\alpha} + nB^{\alpha} \rightleftharpoons rA_mB_n^{\beta} \tag{3.5}$$

where α and β are the different phases; β is the chemically ordered phase, m and n are the stoichiometric numbers for the reactants, and r is the stoichiometric number for the products. The driving force for the reaction (Equation 3.5) can be numerically described as the change in energy that results from converting the individual atoms into a stoichiometric compound;

$$\Delta G = r(\mu^{\beta}_{A_mB_n}) - m\mu^{\alpha}_{A} - n\mu^{\alpha}_{B} \tag{3.6}$$

The driving force in Equation 3.6 is described by chemical potentials (μ). Chemical potentials can be re-written in terms of activity through the equation:

$$\mu_i = \mu_i^0 + RT\ln(a_i) \tag{3.7}$$

Substituting Equation 3.7 into Equation 3.6 gives;

$$\Delta G = r((\mu^{\beta}_{A_mB_n})^0 + RT\ln(a^{\beta}_{A_mB_n})) - m((\mu^{\alpha}_{A})^0 + RT\ln(a^{\alpha}_{A})) - n((\mu^{\alpha}_{B})^0 + RT\ln(a^{\alpha}_{B})) \quad (3.8)$$

Combining the logarithmic terms in Equation 3.8 gives;

$$\Delta G = r((\mu^{\beta}_{A_mB_n})^0) - m((\mu^{\alpha}_{A})^0) - n((\mu^{\alpha}_{B})^0) + RT(r\ln(a^{ox}_{A_mB_n}) - m\ln(a^{\alpha}_{A}) - n\ln(a^{\alpha}_{B})) \quad (3.9)$$

combining all the μ^0 terms in Equation 3.9 ($r((\mu^{\beta}_{A_mB_n})^0) - m(\mu^{\alpha}_{A})^0) - n((\mu^{\alpha}_{B})^0)$) into ΔG^0_f; raising the logarithmic terms to the power of the logarithm coefficient gives:

$$\Delta G = \Delta G^0_f + RT(\ln((a^{\beta}_{A_mB_n})^r) - \ln((a^{\alpha}_{A})^m) - \ln(a^{\alpha}_{B})^n)) \quad (3.10)$$

combining the logarithms in Equation 3.10 produces an equation that describes the driving force for stoichiometric equations to be determined solely in terms of activities and the Gibbs free energy of formation:

$$\Delta G = \Delta G^0_f + RT\ln\left(\frac{(a^{\beta}_{A_mB_n})^r}{(a^{\alpha}_{A})^m(a^{\alpha}_{B})^n}\right) \quad (3.11)$$

where G^0_f is the formation energy of the produced compound, R is the molar gas constant, and a is the activity. ΔG is the resultant energy change from the formation of the compound. Chemical potential is equivalent to using individual elements' activity;

The values of chemical potentials are easier to calculate than activities as they can be determined from a wide range of thermodynamic calculation methods such as the Compound Energy Formalism or available software packages such as Thermo-Calc. The alternative value for use is activities a; $a_i = \gamma_i x_i$ where γ_i is the activity coefficient and x is the

molar fraction for element i. The activity of each element is not linear with respect to concentration, and therefore this has to be adjusted by the activity coefficient; this can be obtained from CALPHAD databases.

The computed driving force for the reaction can calculate the total flux of elements which have moved across the interface through the reaction; this is based on the diffusion equation described by Larsson et al. [1] where the driving force rather than being driven by a chemical potential gradient is defined by the driving force for the reaction but has modifications that the elemental mobility at the interface is not equal for different elements;

$$j_R = -\sqrt{x_f^\alpha}\frac{\bar{M}_f^\alpha}{V_m}.\frac{\Delta G}{\Delta z} \tag{3.12}$$

where j_R is the total number of moles which move across the interface. $x_f{}^\alpha$ is the molar fraction of the fastest diffusing species in the α phase; this value is selected as the reaction is limited by the amount of the fastest diffusing element available for the reaction. $M_f{}^\alpha$ is the mobility of the fastest diffusing species in the α phase as the molar fraction value used is the fastest diffusing element; therefore this mobility is selected to modify the rate of reaction. V_m is the molar volume, Δz is the grid spacing across the interface from the centre of the different volumes. The total flux of atoms across the interface is scaled to the bulk element concentrations;

$$j_A = \frac{m}{m+n}j_R \tag{3.13}$$

$$j_B = \frac{n}{m+n}j_R \tag{3.14}$$

In both equations 3.13 and 3.14, the flux of moles moved is the fraction of the stoichiometric numbers ($\frac{n}{n+m}$); this preserves the stoichiometry of the growing phase.

Producing a numerical model that can consider systems with compositions more complex than a binary requires extra considerations. The chemically ordered phase needs to grow

at the composition determined by its stoichiometry. For alloys where multiple elements can form a similar compound, there needs to be a method to describe the variation within the sublattice that is filled by multiple elements and the variations within the bulk phase. To model a system greater in size than a binary, each possible combination of chemically ordered phases is considered, and the proportion of their growth is scaled with the bulk elemental contributions;

$$\Delta G_{i:j} = \mu_{i_m j_n} - m\mu_i^\alpha - n\mu_j^\alpha \tag{3.15}$$

where i and j are the components that make up the compound $\mathrm{i_m j_n}$. Substituting the driving force for systems bigger than a binary Equation 3.15 into Equation 3.12 produces:

$$j_{R,i,j} = -\sqrt{x_j^\alpha}\frac{M_j^\alpha}{V_m}\frac{G_{i:j}}{\Delta z} \tag{3.16}$$

The fluxes for the i elements are then the total reaction fluxes for the element i scaled for stoichiometry and the solution phase composition. Combining Equation 3.16 with Equation 3.13 and Equation 3.14 produces'

$$j_i = -\frac{m}{m+n}\sum_j j_{R,i,j}\sqrt{\frac{x_i}{\sum_{k\neq j} x_k}} \tag{3.17}$$

$$j_j = -\frac{n}{m+n}\sum_i j_{R,i,j}\sqrt{\frac{x_j}{\sum_{k\neq i} x_k}} \tag{3.18}$$

the fraction $\frac{x_i}{\sum_{k\neq j} x_k}$ scales the flux across the interface related to individual elemental concentrations at the interface. This is required as the flux across the interface calculated is the total number of moles; this therefore needs scaling to the individual fraction of each element.

Simulating the evolution of the bulk phase uses the equation used by Larsson et al. [1, 249, 250];

$$j_i = -\frac{\bar{M}_i \bar{x}_i}{V_m} \frac{\Delta \mu_i}{\Delta z} \tag{3.19}$$

where j is the diffusion flux, M is the mobility, x is the molar fraction, μ is the chemical potential, and z is the distance between the centre of slices. The subscript i refers to the element of interest. This flux equation is modified to produce the total flux in equation 3.12. The fluxes of atoms that are calculated are converted into the change in the number of moles;

$$\Delta n_i = A t j_i \tag{3.20}$$

where n is the number of moles, A is the interfacial area of the slices, and t is the time step for the simulation. The thickness of the slice is determined by the number of moles present within each slice;

$$z = \frac{V_m \sum N}{A} \tag{3.21}$$

3.2.2 Parameters and Numerics of Simulations

This model uses the simplification that the molar volume is constant within each phase and during the reaction; this prevents the model from being entirely accurate for modelling any expansion or shrinkage related to the different phases, as the size of each slice is not varied based on the different elements and their composition, purely based off the total number of elements which are present.

The simulation of Cementite Fe_3C was decided to be used as its formation can be treated as a reaction, and there exists a good range of existing data available within the literature. Multiple simulations were performed for both of these models, initially to test the model and compare it to well-known models such as DICTRA. Models for the chemically ordered phase were modelled on only Fe-C and Fe-Cr-C. In the binary case the *bcc* phase had a composition of 0.05at%C, and the balance was Fe. 100 slices were used, spread evenly

Table 3.1: End member values for each phase elemental interaction for both α and β phases

	Energy ($kJ.mol^{-1}$)	
	α phase	β phase
$G_{A:B}$	-60	-80
$G_{A:Va}$	-50	—

Table 3.2: End member values for all elemental combinations for both α and β phases

	Energy ($kJ.mol^{-1}$)	
	α phase	β phase
$G_{A:C}$	-60	-80
$G_{A:Va}$	-50	—
$G_{B:C}$	-50	-100
$G_{B:Va}$	-60	—

over a simulation domain of 100μm. The data was computed using the Compound Energy Formalism due to complications with getting the chemical potentials of the chemically ordered phase from the Thermo-Calc TQ interface. As the Thermo-Calc TQ interface was not used, the CALPHAD assessment of iron, chromium and carbon from [251] was used. These simulations were performed at 700K and 800K. The ternary system had a starting composition of 0.05at%C and 0.1at%Cr, and a starting chemically ordered phase composition of 0.25at%Cr. DICTRA simulations were run using standard settings and a simulation domain that matched the numerical model presented in this work.

The system used for demonstrating this model's ability used the end members; ${G_{A:Va}}^{\alpha} = -50kJ.mol^{-1}$, ${G_{A:B}}^{\alpha} = -60kJ.mol^{-1}$ and ${G_{A:B}}^{\beta} = -80kJ.mol^{-1}$ also displayed in Table 3.1. The molar volume was kept at $1 \times 10^{-6}m^3mol^{-1}$ for both phases, the mobility of elements A and B in the solution phase was $1 \times 10^{-25}m^2J^{-1}s^{-1}$ and $1 \times 10^{-15}m^2J^{-1}s^{-1}$ respectively. These simulations were performed at 700K, with a composition in the α phase as 5at% B. The β phase was modelled as a *bcc* structure with B being the interstitial site element. Simulations that varied the different stoichiometric compound that would grow had the same initial composition in the *bcc* phase.

For the ternary assessment the end members that were used were displayed in Table 3.2; ${G_{A:C}}^{\alpha} = -60kJ.mol^{-1}$, ${G_{B:C}}^{\alpha} = -50kJ.mol^{-1}$, ${G_{A:Va}}^{\alpha} = -50kJ.mol^{-1}$, ${G_{B:Va}}^{\alpha} = -60kJ.mol^{-1}$, ${G_{A:C}}^{\beta} = -80kJ.mol^{-1}$ and ${G_{B:C}}^{\beta} = -100kJ.mol^{-1}$ and the mobilities within the solution phase were $1 \times 10^{-25}m^2J^{-1}s^{-1}$ for elements A and B and $1 \times 10^{-15}m^2J^{-1}s^{-1}$ for

element C. The chemically ordered phase grown had a composition of (A, B)$_2$C and the concentrations of A and B were equal within the β phase.

Similarly to previous work and as described by Larsson et al. [1] the oxide grid points are allowed to split and join, allowing for a dynamic simulation region. Splitting occurs when a grid volume has reached 30% of its original volume, splitting into two equal new grid volumes of the same composition. Joining is when a grid volume has reached less than 30% of its original volume, and its mass is moved into a neighbouring grid volume with the same phase. This comparison relies on fixed cross-sectional areas and volumes only varying by thickness changes. This technique is essential to prevent the grid volumes from becoming empty or too full of mass; both reduce the model's stability. As a single oxide volume is defined during this model, the splitting and joining scheme facilitates compositional dependence of the oxide phase as the metal, and alloying elements diffuse within the region as the mass is contained in multiple volumes.

3.3 Results

Figure 3.1 shows the phase interface position for a binary AB system, where the resulting stoichiometric compounds that are formed are varied. Results show that the transformation rate is unrelated to the different compound formed; however, the amount of transformed compound is greater as the contribution of element A in the compound increases, as seen from an increase in the resulting phase interface position.

The numerical model is capable of simulating the growth of a multi-element system. Figure 3.2 shows a ternary system; growing the compound $(AB)_\alpha C_\beta$. Different starting solute phase compositions are simulated to show the effect of the variation in the chemically ordered phase. As the concentration of B is increased, the rate of the precipitate reaction is decreased, and the interface position slowly reaches equilibrium; for a starting B concentration of 0.2 moles, the simulation reaches equilibrium at $5,000$s whereas for a starting B concentration of 0.6 moles the time is $15,000$s . The thickness of the formed precipitate is also reduced; the difference between the interface position is 11μm.

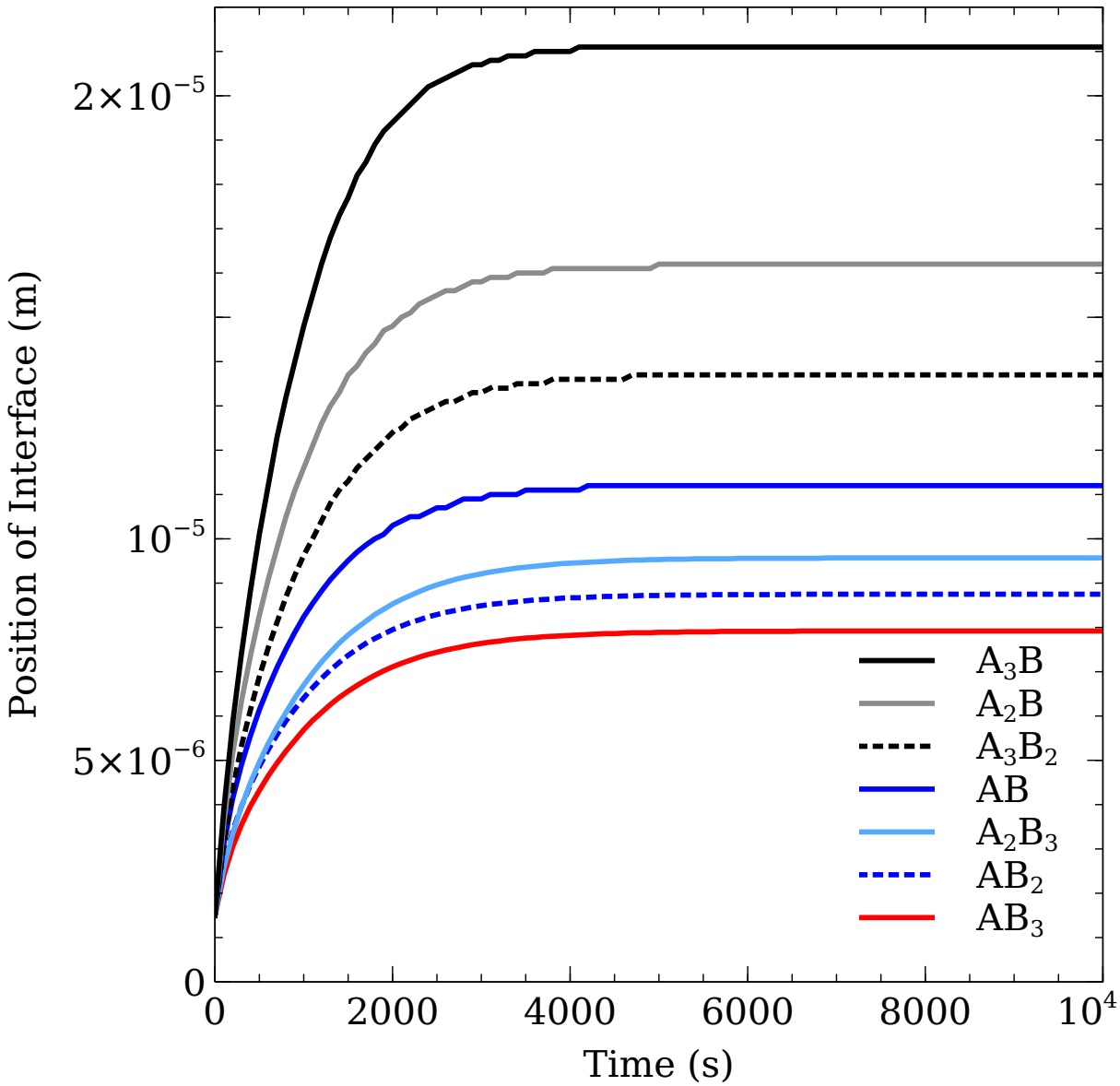

Figure 3.1: Simulations from the numerical modelled defined within this work; show the interface position over time of a range of different stoichiometries for a binary system that starts at the same composition; 0.8at% A and 0.2at%B at 700K. The higher the concentration of element A within the formed stoichiometric compound, the higher the interface position between the ordered and bulk phases; this occurs once the concentration of element B is depleted within the simulation domain. The rate of the reaction is independent of the element concentrations.

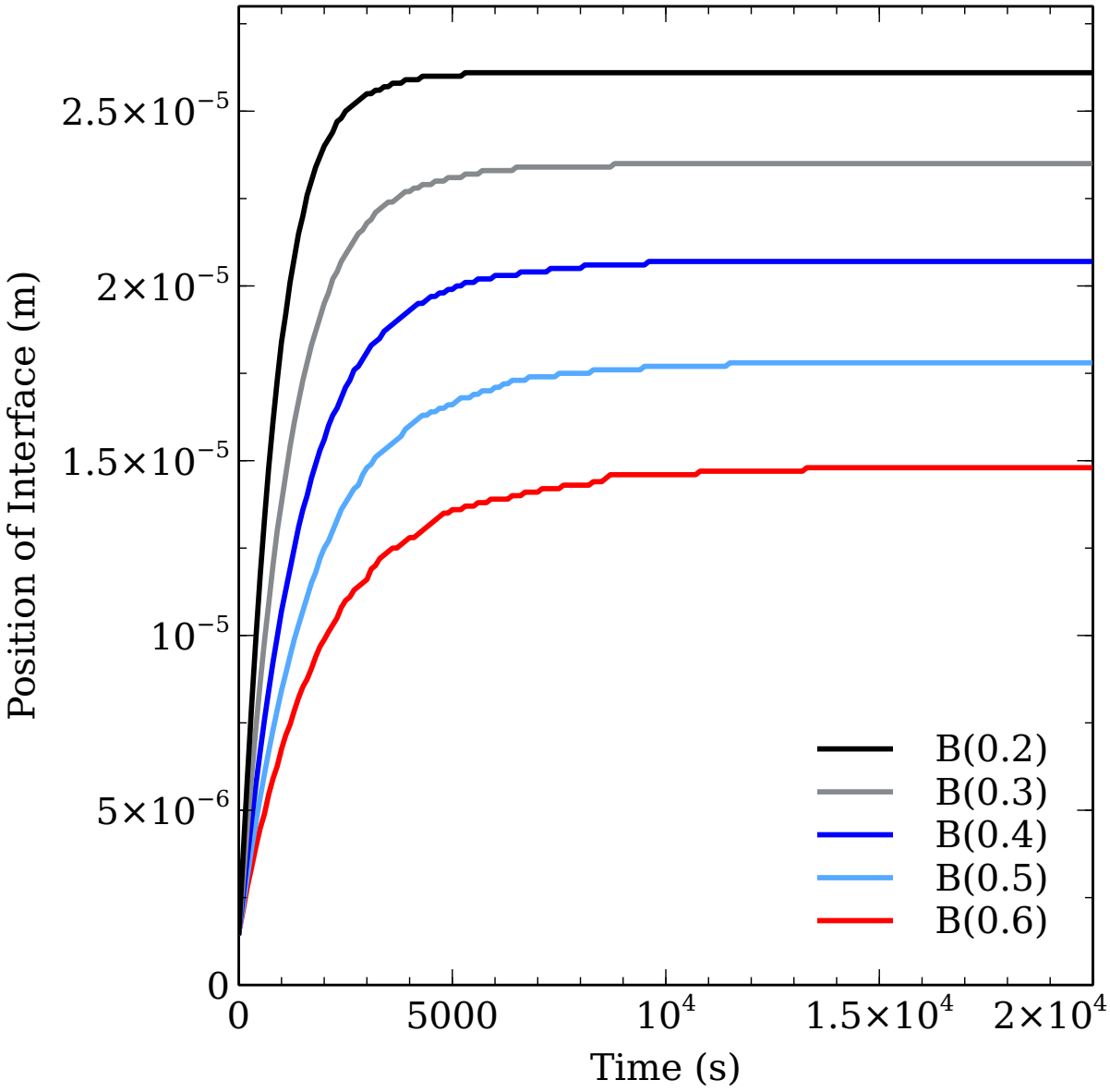

Figure 3.2: The results of a ternary system (A, B)$_2$C at 700K show the effect of varying the concentration of element B. As the concentration of element B increases, the interface reaction time is reduced. Further to this reduction in interface reaction, there is a reduction in the total volume of the formed stoichiometric compound. This reduction in the formed stoichiometric phase is due to the lower driving force for creating the compound B_2C over A_2C. The lower the B concentration in the bulk phase, causes the phase interface between the bulk and stoichiometric phase is due to the system's ability to use carbon in the reaction.

Figure 3.3 shows how the initial concentration of B influences the amount of element B in the precipitate phase. There is variation and oscillation within concentrations of A and B, which is more pronounced for a higher concentration of B. The concentration of C does not vary as this contributes to the interstitial sublattice. The oscillation across the bulk-stoichiometric phase interface is a by-product of the splitting within the stoichiometric phase. As mass travels across the interface, the volume of the stoichiometric phase increases; once sufficient mass has moved, this grid volume is split into two grid volumes maintaining the composition that existed at that point in time. The bulk grid volumes equally have a joining component that contributes; as the volume at the interface decreases due to mass transport, this eventually is combined with a neighbouring volume. As elements A and B are comparatively slow to diffuse compared to element C, the variation within the bulk is less significant; however, the diffusion across the interface for element B is greater than that of A. Therefore, elements A and B are changing interface grid volume composition as the grid volumes are merged over time.

The interaction between the solution and chemically ordered phases can influence the growth rate of the phase. To show the effect of different adjustments is simulated. Figure 3.4 shows how the interface mobility modifier has very little effect between 0.01 and 0.001 ; however, for a lower mobility modifier of 0.0001, there is a significant reduction in the rate of the phase growth.

To validate the numerical model, the growth of Cementite is simulated in binary (Fe_3C) and ternary ($(Fe, Cr)_3C$). The binary growth simulated by this work (red) is compared to that given by DICTRA (black) within Thermo-Calc (dotted line). The rate of the precipitation growth is increased as the temperature increases from 700K (c.f. Figure 3.5) to 800K (c.f. Figure 3.6). The comparison between both positions is shown relative to a Thermo-Calc equilibrium condition from the initial starting concentrations. The interface position determined from this model predicts a slightly thicker interface than what DICTRA determines, and the rate is slightly slower; the difference between the two models' interface position is 1μm.

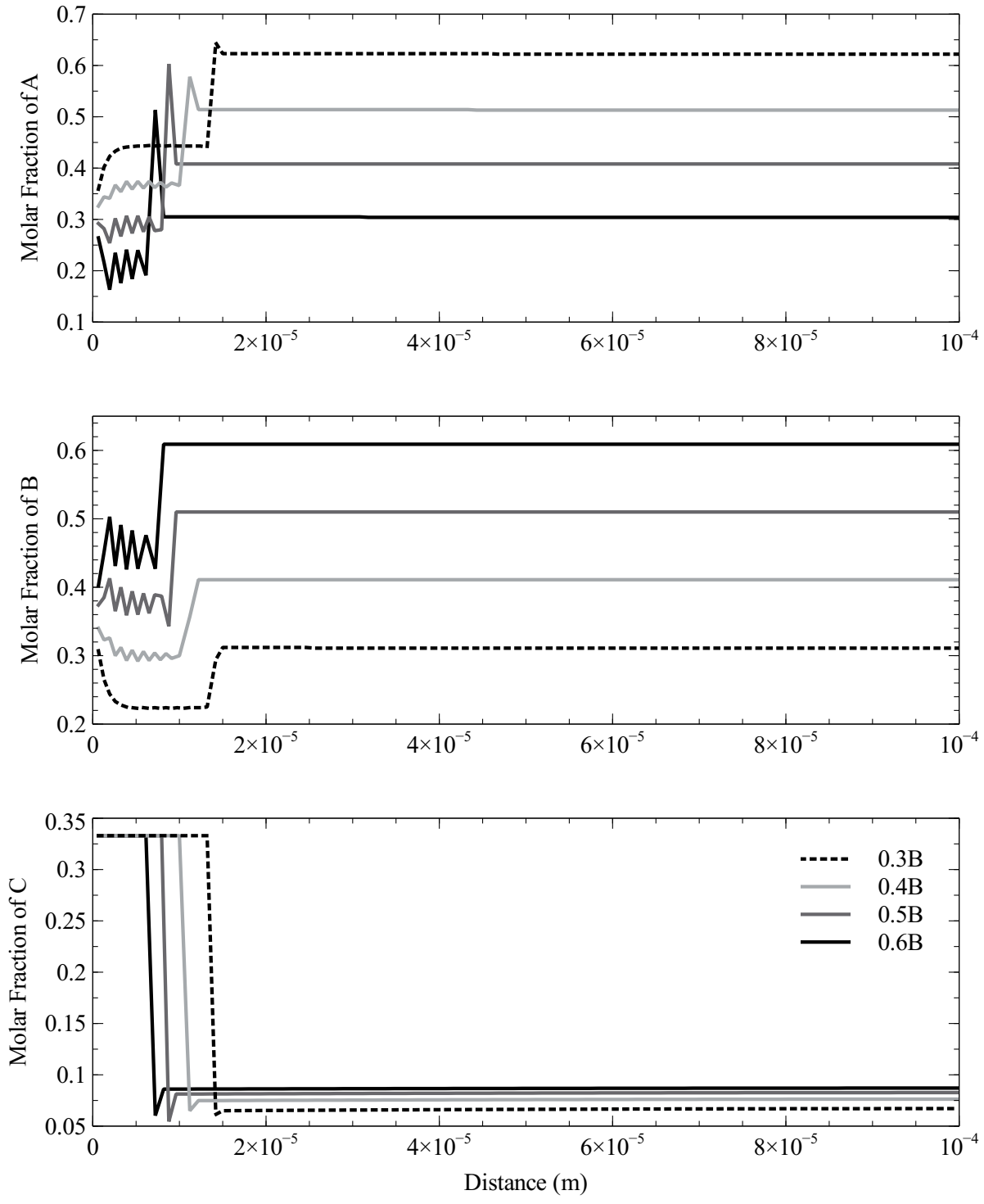

Figure 3.3: Simulated concentration against time for chemically ordered phase growth for a ternary system once. Equilibrium is reached by the simulation after (20, 000s at 700K). As the starting concentration of A within the bulk phase is decreased, the formed stoichiometric phase composition begins to oscillate; this is an artefact of the model's design with grid points and the ability for concentrations to segregate within simulation domain volumes.

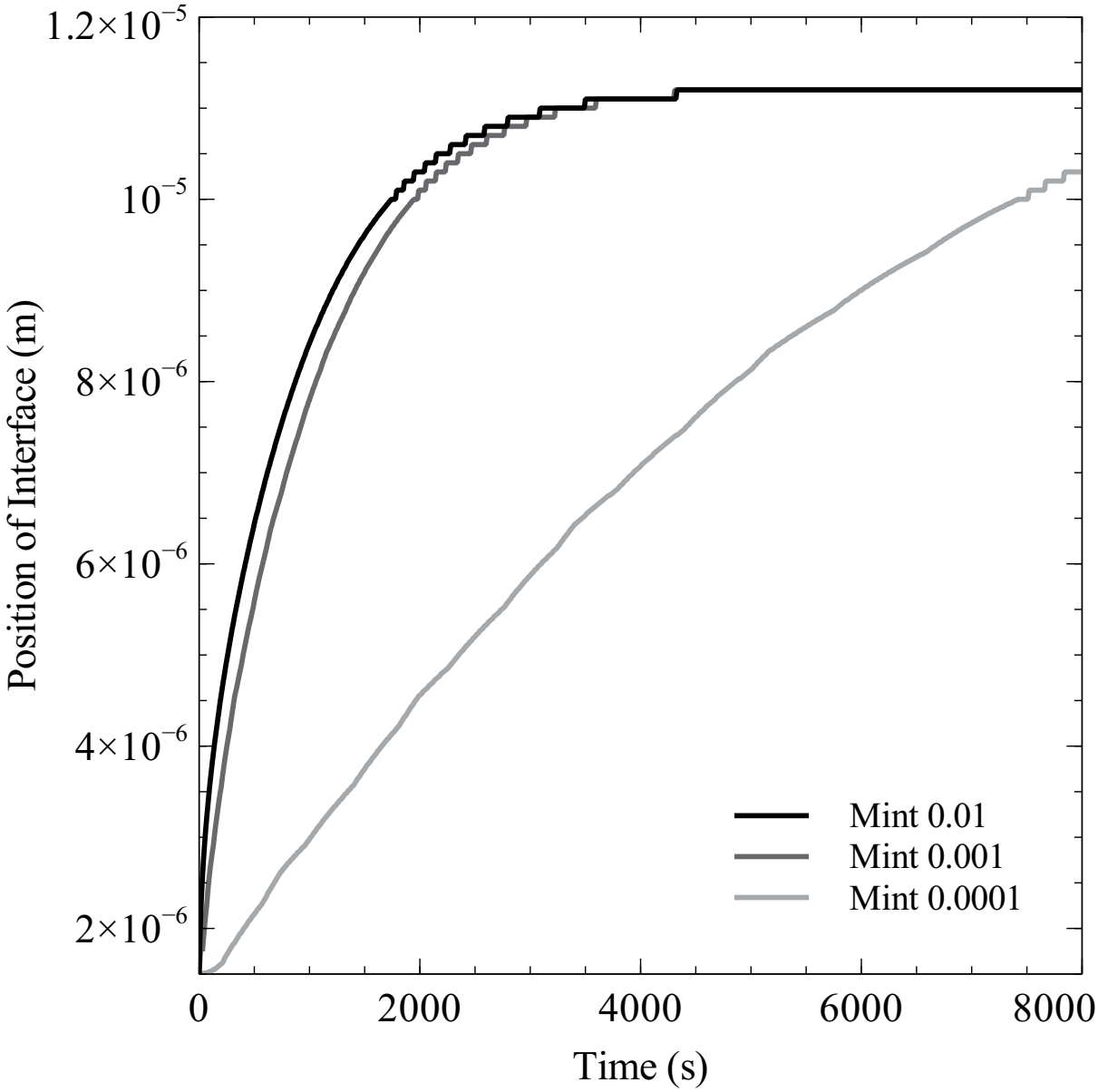

Figure 3.4: Simulated interface position over time for interface mobility modifications of 0.01, 0.001 and 0.0001 for a binary system at 700K. The rate of chemically ordered phase growth at values of 0.01 and 0.001 show the same trend in rate; these reactions are predominantly diffusion limited, whereas the reaction is limited by the rate of the reaction to form the stoichiometric phases is formed when the interface mobility adjustment is set at 0.0001.

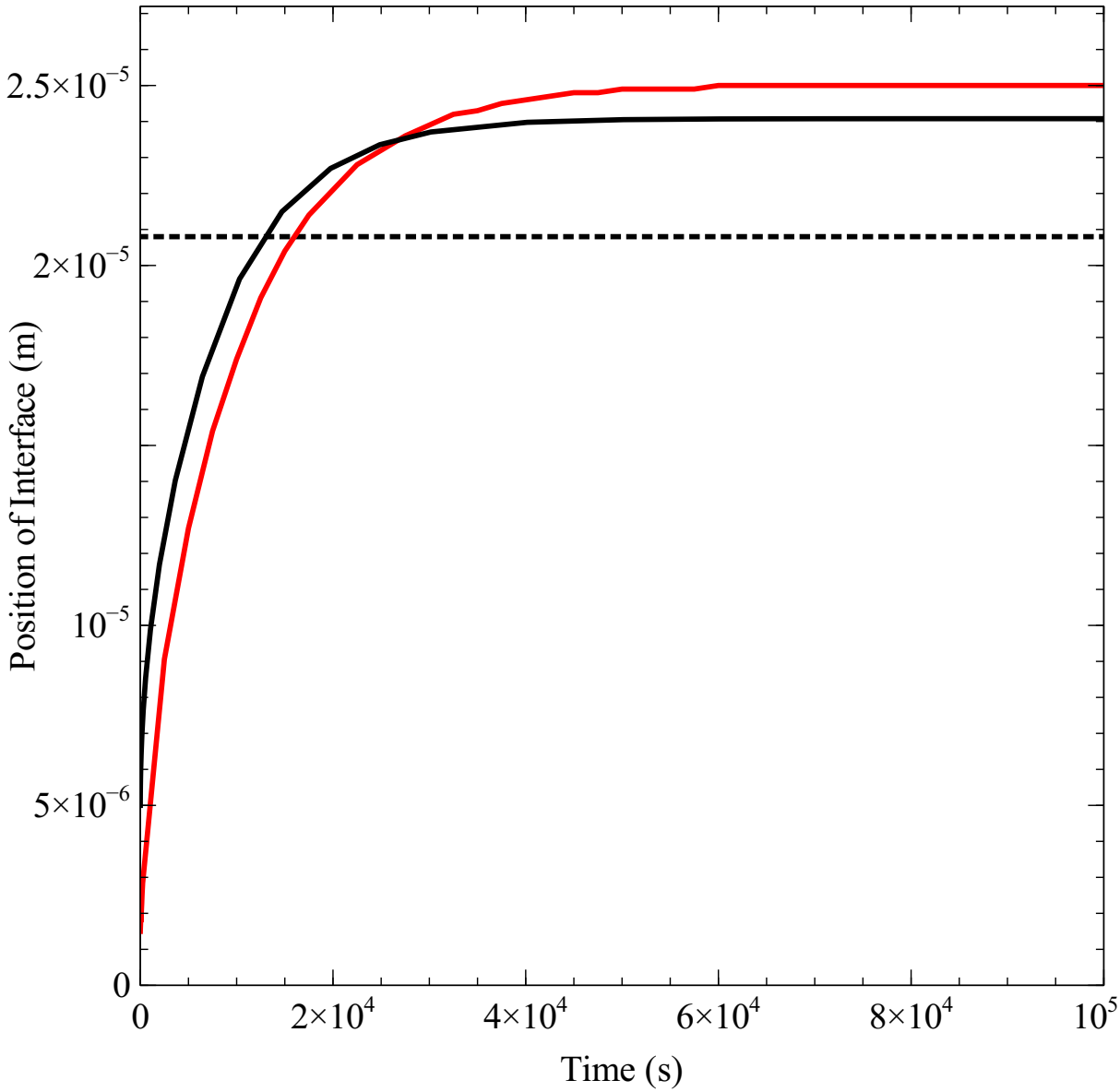

Figure 3.5: Comparison of the interface positions for simulating the growth of Cementite in ferrite in DICTRA (black) and the numerical model developed within this work (red) at 700K. The reaction rate is similar between the two, and the overall resulting interface position is within 1μm of each other. The reduction in reaction rate is likely due to the different numerical methods behind the calculations. For comparison, Thermo-Calc is used to determine an equilibrium calculation (black dotted) for the same bulk composition, which produces an interface but does not consider the starting composition that has formed.

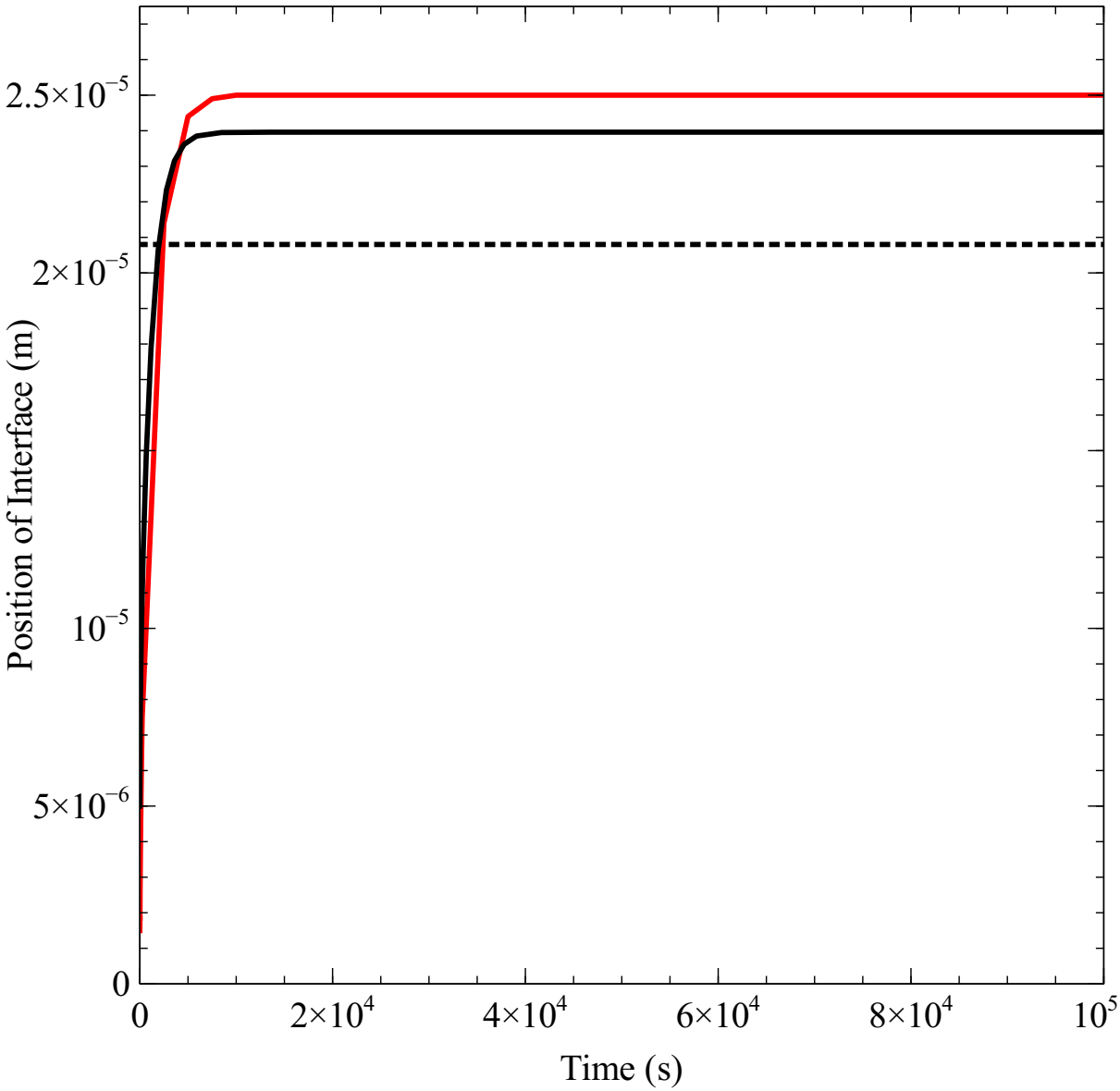

Figure 3.6: comparison of the interface positions for simulating the growth of Cementite in ferrite ordered phase in DICTRA (black) and the numerical model developed within this work (red) at 800K. The reaction rate is similar, and the overall resulting interface position is within 1μm of each other. The reduced reaction rate is likely due to the different numerical methods behind the calculations. For comparison, Thermo-Calc is used to determine an equilibrium calculation (black dotted) for the same bulk composition, which produces an interface but does not consider the starting composition that has formed.

The concentration profiles of the two techniques follow each other at all temperatures simulated. The difference in growth rate between this model and DICTRA is apparent at earlier time steps as the two concentration profiles do not track one another as closely at 700K (c.f. Figure 3.7) as they do once the reaction has used up all available carbon (c.f. Figure 3.8). The 1μm difference in the final interface position is not easily discernible.

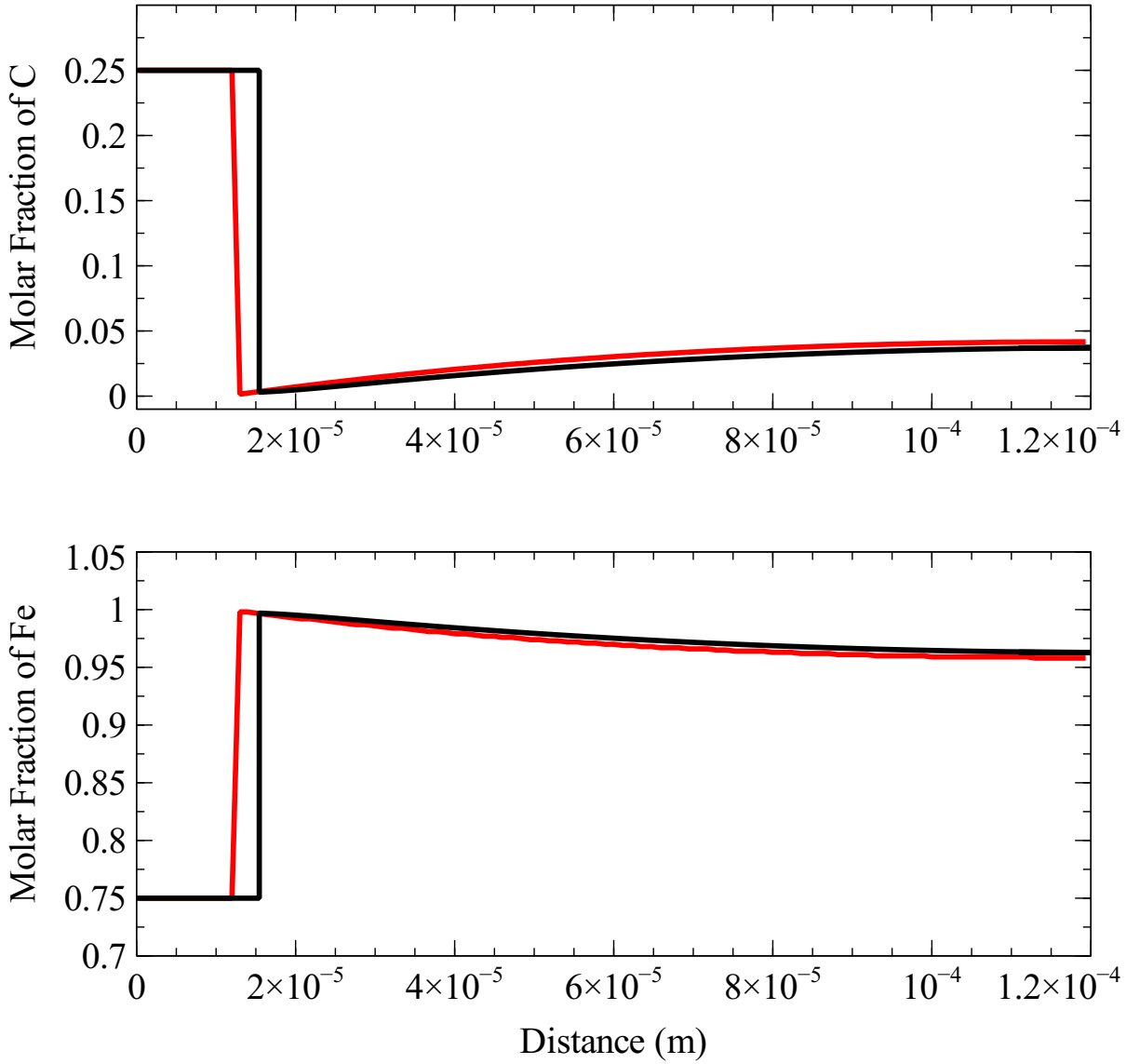

Figure 3.7: Concentration profile for carbon and iron for the resulting simulations in DICTRA (black) and the numerical model developed within this work(red). Simulations had run for 5,000s at 700K. The concentrations in the ferrite phase have a very similar profile showing how similar the two techniques are in their results. The concentration of carbon is depleted more at the interface between the two phases in both carbon and iron.

Figure 3.9 and Figure 3.10 show concentration profiles at 800K as the simulation has proceeded further there is less of a difference between the two techniques. The increased

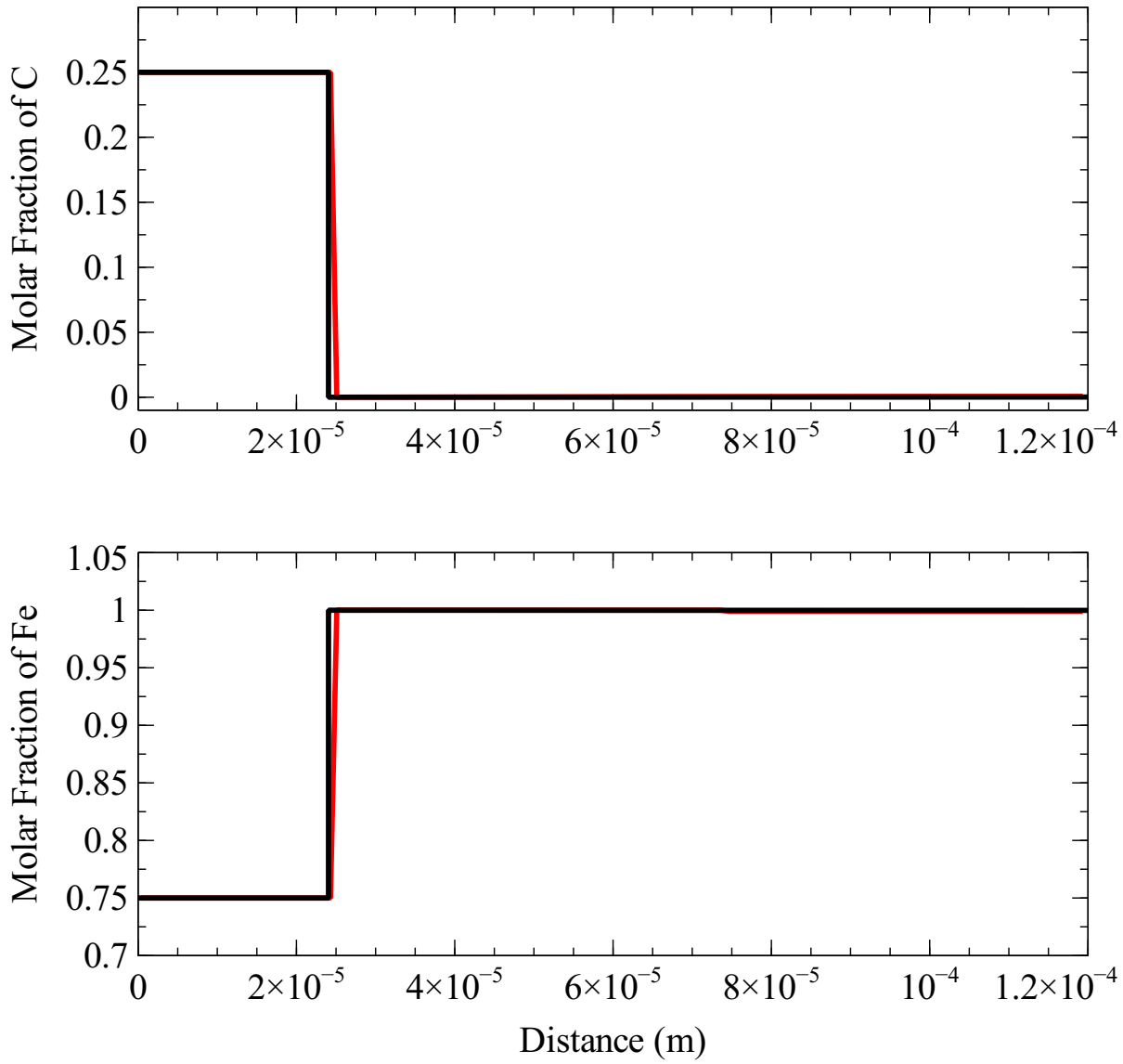

Figure 3.8: Concentration profile for carbon and iron for the resulting simulations in DICTRA (black) and the numerical model developed within this work (red). Simulations had run for 50,000s at 700K. The concentrations in the ferrite phase have a very similar profile showing how similar the two techniques are in their results. The concentration of carbon is depleted within the ferrite phase entirely, which has stopped any further reaction from occurring.

growth rate from a higher temperature allows the simulation to reach equilibrium quicker and causes the two models to track interface positions and concentration profiles better.

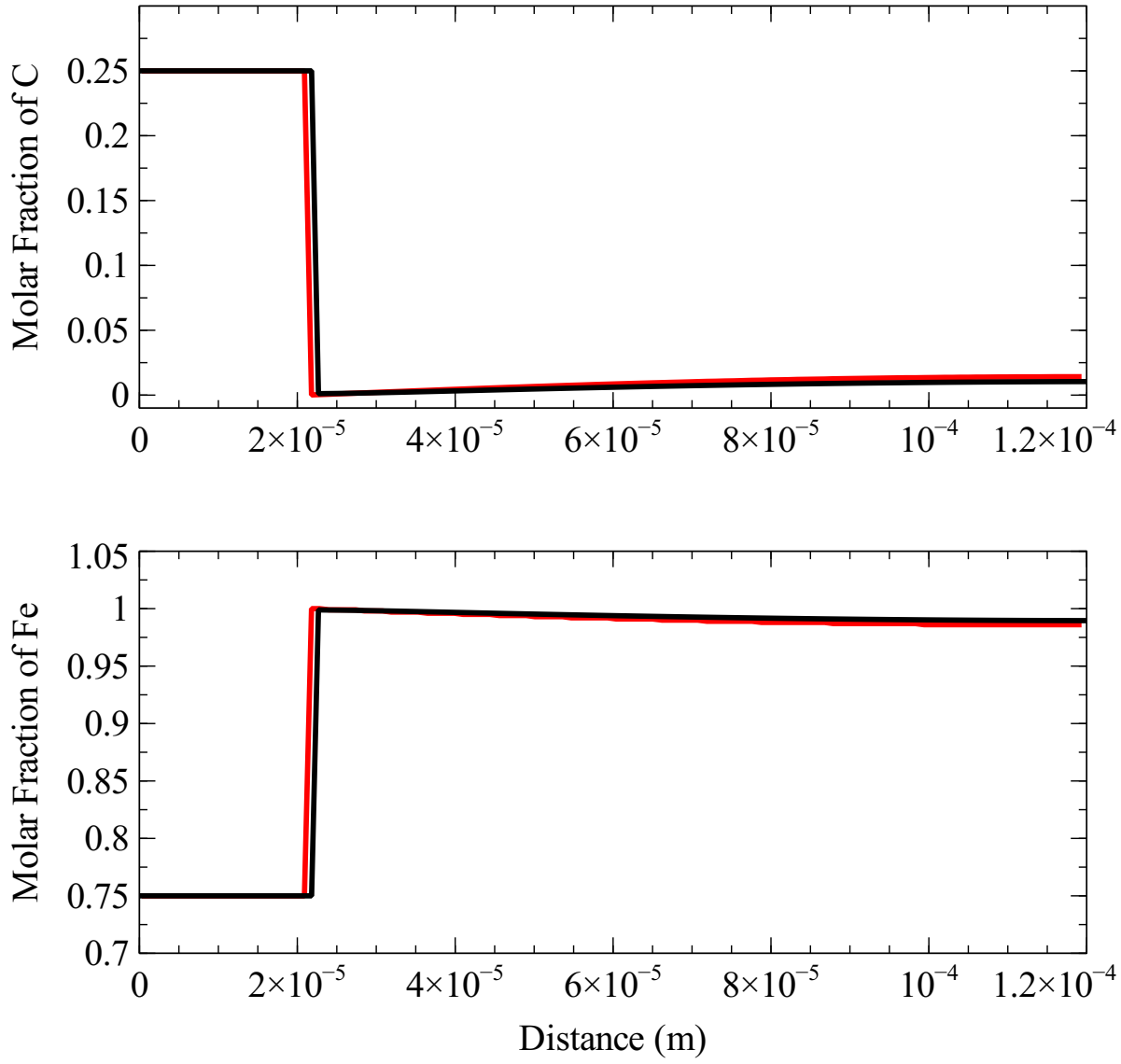

Figure 3.9: Concentration profile for carbon and iron for the resulting simulations in DICTRA (black) and the numerical model developed within this work (red). Simulations had run for 2,500s at 800K. The concentrations in the ferrite phase have a very similar profile showing the similarities between the two numerical techniques in their results. The concentration of carbon is depleted within the ferrite phase in front of the interface.

Modelling the growth of (Fe, Cr)$_3$C results in the growth of a precipitate with roughly similar concentrations of the substitutional sublattice in the solute phase; the average Cr concentration is 0.08%, and the Fe concentration is 0.67%. Figure 3.11 shows the precipitate growing preferentially with Cr, which causes the depletion of Cr at the interface. The simulated domain does not interact outside the modelled volume; the overall reaction

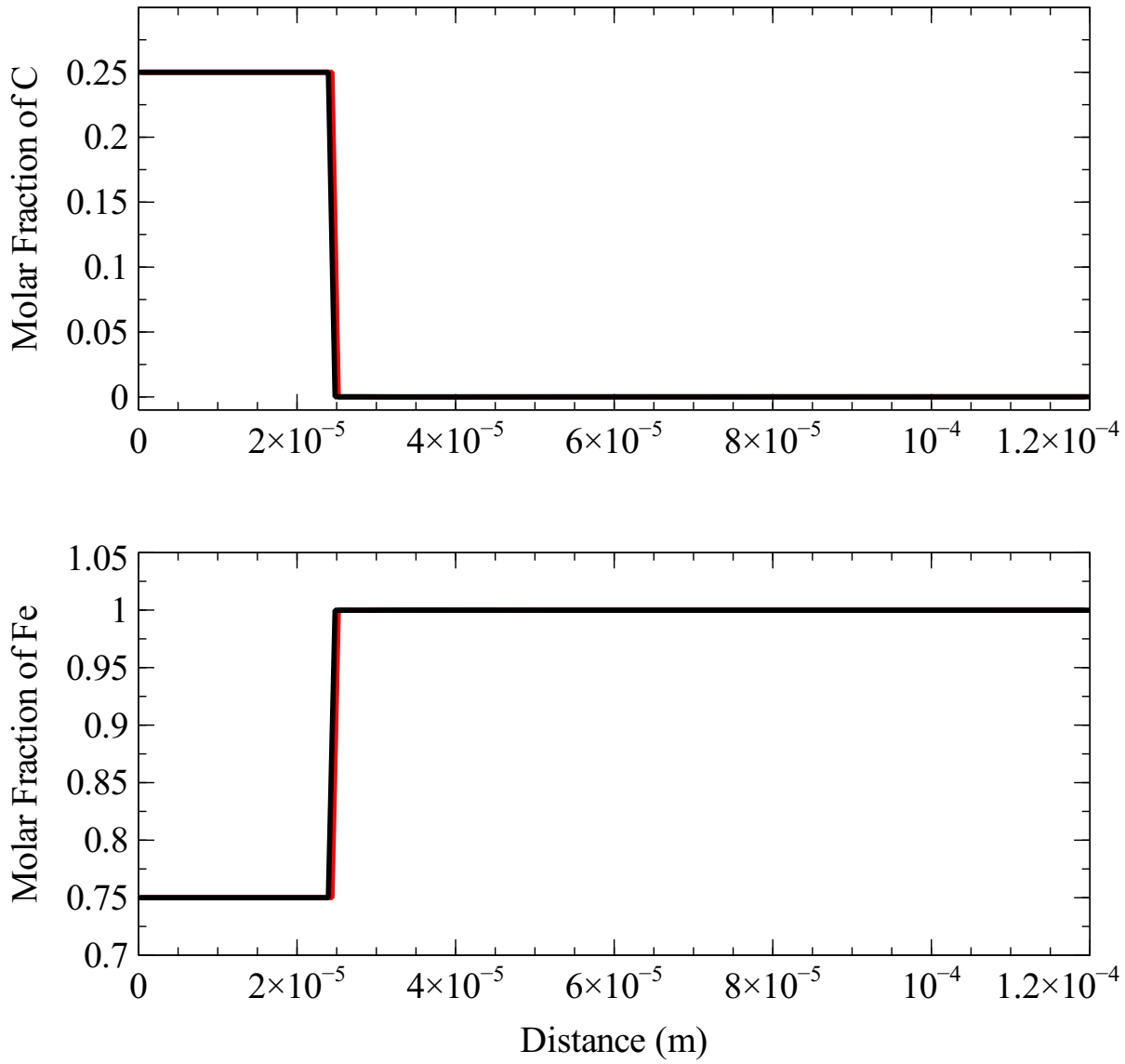

Figure 3.10: Concentration profile for carbon and iron for the resulting simulations in DICTRA (black) and the numerical model developed within this work (red). Simulations had run for 10,000s at 800K. The concentrations in the ferrite phase have a very similar profile showing the similarities between the two numerical techniques in their results. The concentration of carbon in the ferrite phase is severely reduced, indicating that all available carbon has been reacted, resulting in no further reaction occurring.

stops once the carbon in the *bcc* phase is depleted.

3.4 Discussion

Figure 3.1 shows that numerical model growing a range of different chemically ordered phases for a range of reactions, and shows that the stoichiometry bears no significant role in the reaction rate. The position of the interface, which is related to the growth of the growing phase, increases with a lower B contribution in the stoichiometry, as the solution phase has a reduced quantity of available B within the bulk. The simulations run until equilibrium; therefore, the solution phase concentration of B has been depleted. The only equilibrium within a binary system is where an element is depleted within the solute phase due to the lack of diffusion within the chemically ordered phase.

The growth of a precipitate in a ternary system has extra complexity from the need to ensure the conservation of stoichiometry whilst also allowing variation within the substitutional sublattice and influenced by the solution phases' elemental concentrations. Growing the chemically ordered phase $(A, B)_2C$ and varying the solution phase concentration of A and B, thermodynamically from the chosen end member values, the compound B_2C is the preferred phase to form. As the concentration of B increases, Figure 3.2 shows the phase growth rate decreasing because the driving force between the solution phase and chemically ordered phase is smaller than the driving force for element A. The depletion of element B at the interface causes an increase in the concentration of element A at the interface, which is the faster compound to form thermodynamically.

Increasing the initial concentration of B within the solution phase results in a decrease in the rate of the chemically ordered phase. The reduced rate of growth results from B's chemical potential within the solution phase being a smaller difference in the driving force for the reaction. As the concentration of B increases within the solution phase, the concentration of C within the solution phase increases the precipitate growth; shown in Figure 3.3. This reduced reaction rate causes a greater concentration of element C within the solution phase after the precipitate has grown. Oscillations are seen within the

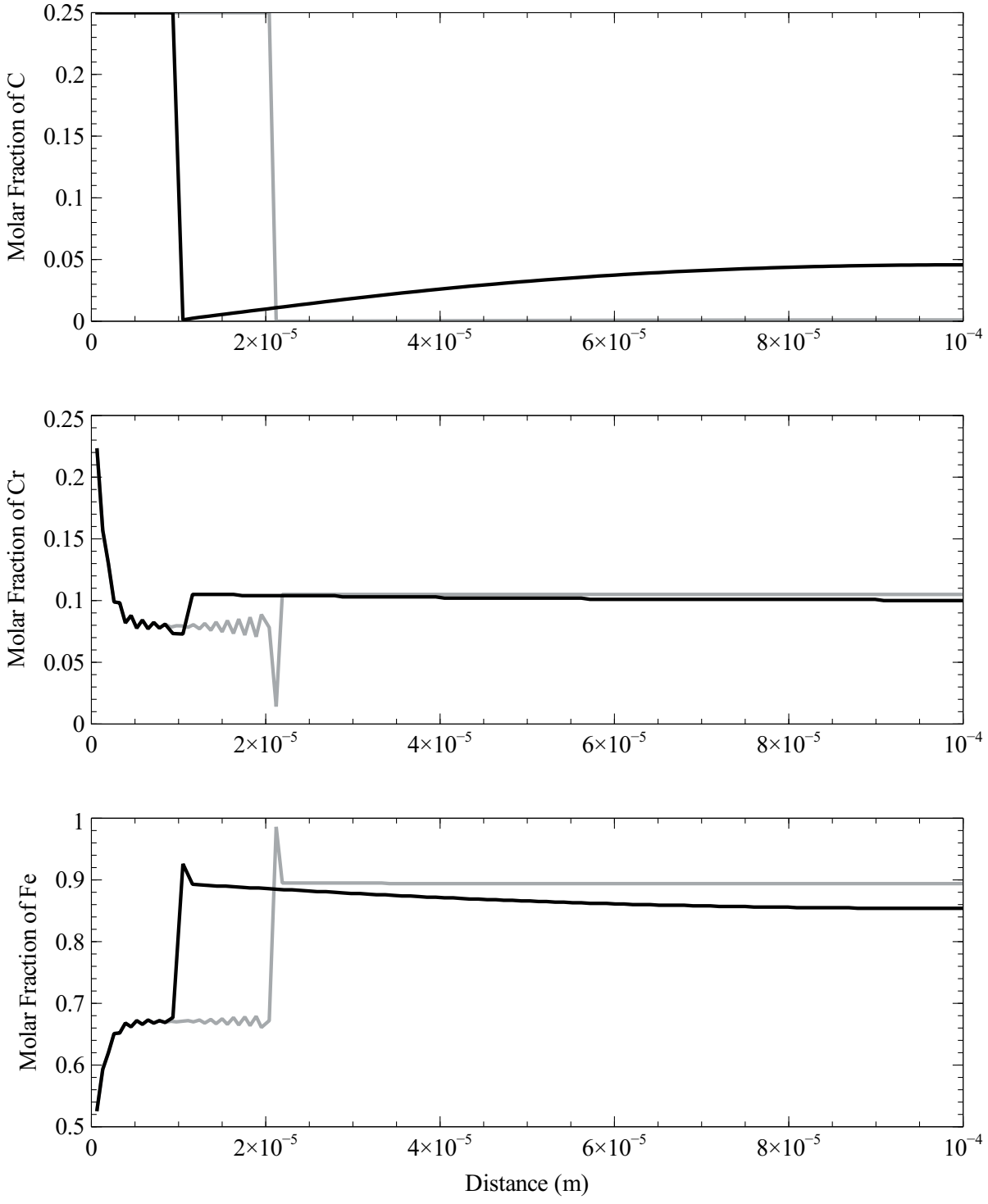

Figure 3.11: Concentration profile vs distance for a ternary growing (Fe, Cr)$_3$C at 700K. Profiles for 1,000s (black) and 10,000s (grey). Concentration profile for carbon, chromium and iron for the resulting simulation after two times (1,000s (black) and 10,000s (grey)) at 700K creating (Fe, Cr)$_3$C. Cr_3C is the preferred compound to form. As Cr_3C is the preferred compound, this decreases within the Cr concentration profile ahead of the phase interface; as the simulation proceeds, the oscillations within the iron and chromium increase. The increased oscillations are due to chromium depletion ahead of the phase interface, which is not replaced. The chromium diffuses at a similar rate to iron and is, therefore, slower than the interface motion, which is tracked with carbon; these oscillations are an artefact of the simulation set up with discrete simulation volumes.

chemically ordered phase as it grows; this is an artefact of the splitting and joining used within the model. Once sufficient mass has been moved into a chemically ordered grid volume, this volume splits equally in half. If the solution phase grid volume had a high concentration of element B, the diffusion into the chemically ordered phase would be more significant. Correspondingly, the concentration of element B within the chemically ordered phase grid volume at the interface would be higher. In the opposite case, where there was a low concentration of element B within the solution phase grid volume, the concentration of element A would be more significant in the chemically ordered phase and would be seen as less B concentration in that grid volume. Diffusion is not simulated within the chemically ordered phase, preventing the removal of the oscillatory concentration gradients.

Varying the mobility between the chemically ordered and solution phases provides an insight into what effect the interface reaction has on the growth rate; the effect of the interface mobility is shown plotting the interface position against time in Figure 3.4. For an interface mobility modification of 0.01 and 0.001 times, there is very little difference in the growth rate of the chemically ordered phase. An interface mobility modification of 0.0001 causes there to be a sufficient reduction in the rate of growth. The growth varies sufficiently to where it is nearly a linear growth relationship rather than the square root relationship.

This numerical scheme has been validated through DICTRA within Thermo-Calc for the Fe_3C system in ferrite. The interface positions are compared between the two models and show reasonably good agreement; there is a difference within the final position of 1μm within both Figure 3.5 and Figure 3.6. There is a difference in the reaction rates at 700K; the simulations have reached equilibrium at different times; 6×10^4s for the numerical scheme discussed here and 4×10^4s for DICTRA. At 800K the difference within rates is significantly less, reaching equilibrium within 1×10^3s of each other; this is because of a greater diffusivity at higher temperatures. The difference in interface position could result from the difference in the ways that the two models represent the interface and may be influenced by the conservation of mass within the presented model not able to sufficiently utilise the full amount of carbon within the solution phase. Both techniques

do not provide agreement with Thermo-Calcs single point equilibrium calculation, but this is related to a difference in molar volumes between the different calculations.

DICTRA and the presented numerical scheme agree with their concentration profiles for 700K; after $5,000$s, the difference in growth rates can be seen by a difference in the concentration profiles in Figure 3.7. Figure 3.8 shows how once the simulations have reached equilibrium, the difference between the two concentration profiles is negligible. At 800K the growth rates more closely track, therefore the difference within the concentration profiles shows less discrepancy at $2,500$s; Figure 3.9 displays the concentration profiles being close but not exactly the same. Figure 3.10 shows negligible difference between the two techniques at 800K once equilibrium has been reached.

Figure 3.11 shows the concentration profiles of the growth of a ternary precipitate. Cr_3C is the preferred precipitate to form; however, this is concentration limited within the solution phase. The characteristic oscillations can be seen within the precipitate, this is related to the modelling technique for the simulated volumes. The initial concentration of the chemically ordered phase is 0.5Fe-0.25Cr-0.25C. This initial concentration is maintained and causes a decrease in chromium concentration within the solution phase. The ternary simulation can produce a precipitate with an equilibrium composition based on the starting concentrations, which may differ from other techniques but is because of the solution phase modelling.

3.5 Conclusion

A numerical model has been developed that can describe the growth of chemically ordered phases; the model simulates the reaction across the phase interface and considers the chemical driving force for the formation of the phases to determine the rate at which the phase is grown. The Fe_3C system has been modelled because it is well studied, and there is plentiful data within the literature. Comparisons with DICTRA show a similar resulting output of composition and rate of reaction. The technique developed within this work is sufficient to model the growth of multi-element chemically-ordered phases.

Simulating multi-element chemically ordered phases allows the model to predict how the phases' composition varies during their growth rate.

Chapter 4

Modelling the Growth of Nickel Oxide

4.1 Introduction

The development of a numerical model to simulate the growth of an oxide has many different applications in optimising alloy design through more informed and less costly physical experimental methods with a drive to improve component service lifetimes, though a greater understanding of the different alloying elemental contributions to the final alloying material.

Nickel oxidation is well documented and described; the research having started in the 1950s by Wagner [102]. However, there is a lack of numerical models that describe oxidation on a macro-scale. Numerous models rely on an understanding of atomistic reactions, molecular dynamics (MD) [5, 11, 130, 136, 178, 252–254] and Density Functional Theory (DFT) [6, 253, 255]; these techniques are used to understand the mechanisms that influence the initial growth of an oxide. MD and DFT simulation results can influence the elemental choices used in the overall alloy design. MD and DFT can also be used to determine parameters that feed into other modelling techniques [256]. The lack of suitable oxidation models for describing physical oxidation experiments limits the ability of numerical simulations to play a role in influencing the alloying concentrations in alloy design; due to the lack of an understanding numerically as to each element's contribution

to oxidation. Numerical simulations into the alloying elements and concentrations with which they are added can help to influence the physical experiments into the oxidation behaviour of alloys to reach a better oxidation resultant alloy; especially as current alloys are a complex mix of more than 10 elements [8, 21–26].

This work aims to develop a simple numerical scheme suitable to model the growth of oxides that can replicate experimental oxidation data. This model will be used to simulate the growth of nickel oxidation as a wide range of experimental data is available in the literature. Nickel oxide is reasonably well understood and has little variation within stoichiometry; often, the only oxide present is NiO as the other oxides Ni_2O and Ni_3O_4 are transitional [172, 178].

4.2 Methodology

4.2.1 Model Description

Oxide growth is a complicated mix of three different contributions; the oxide-metal interface, the diffusion through the oxide and the oxide-gas interface. This model considers each of these different processes; this methodology relies heavily on the presence of vacancies within a sublattice facilitating the diffusion of ions through the oxide. The reaction which describes oxidation is defined as:

$$aMe + bO \rightleftharpoons Me_aO_b \tag{4.1}$$

Oxidation requires a source of both metal (Me) and oxygen (O) to occur (Equation 4.1). Oxidation can be classified as cationic or anionic; the predominant charge carriers determine this through the oxide. There are two distinct reaction interfaces within oxidation; the metal-oxide interface and the oxide-gas interface. Considering the reaction at the metal-oxide interface, the oxygen ions limit the amount of metal that can cross the interface into the oxide. For the oxide Me_aO_b, the reaction to produce the oxide from the base components is related to the number of vacancies on the metal sublattice of the oxide to

allow more metal to travel into the oxide. The oxidation reaction is bi-directional and therefore predicts the dissolution of the oxide should the right conditions be met.

$$aMe^{\alpha} + bVaO^{ox} \rightleftharpoons Me_aO_b \tag{4.2}$$

Equation 4.2 defines the interface reaction that occurs between the metal and oxide interface; the addition of empty oxide sites (VaO) and bulk metal atoms (Me). Assuming that the metal is becoming part of the oxide from the substrate forms from all the nearby oxygen sites where there sits a corresponding metal vacancy; the reaction thermodynamics become the difference between the thermodynamics of the pure oxide and the base metal, including oxide with no metal present on the metal sublattice. Using Equation 4.2 as the definition for the driving force ΔG for metal becoming part of the oxide phase in terms of chemical potentials μ;

$$\Delta G = \mu^{ox}_{Me_aO_b} - b\mu^{ox}_{Va_aO_b} - a\mu^{\alpha}_{Me} \tag{4.3}$$

The chemical potentials can be re-written in terms of activities [182]; activities are typically the preferential means of describing an oxides energy over chemical potentials. The following derivation provides confidence that the two methods (chemical potential and activity) for describing the thermodynamics of oxides are equivalent and that the use of chemical potentials is appropriate.

$$\mu_i = \mu^0_i + RT\ln(a_i) \tag{4.4}$$

the chemical potential is written in terms of a standard chemical potential μ^0_i and the activity a_i. Substituting Equation 4.4 into Equation 4.3 gives:

$$\Delta G = \mu^{0^{ox}_{Me_aO_b}} + RT\ln(a_{Me_aO_b}) - b\mu^{0^{ox}_{Va_aO_b}} - RT\ln(a_{Va_aO_b}) - a\mu^{0^{\alpha}_{Me}} - RT\ln(a_{Me}) \tag{4.5}$$

grouping the logarithmic terms gives in Equation 4.5 gives;

$$\Delta G = \mu^{0^{ox}_{Me_aO_b}} - b\mu^{0^{ox}_{Va_aO_b}} - a\mu^{0^{\alpha}_{Me}} + RT\left(\ln(a_{Me_aO_b}) - \ln(a_{Me}) - \ln(a_{Va_aO_b})\right) \tag{4.6}$$

the μ^0 terms within Equation 4.6 can be combined to form ΔG^0_f which is the formation energy of the reaction.

$$\Delta G = \Delta G^0_f + RT\left(\ln(a_{Me_aO_b}) - a\ln(a_{Me}) - b\ln(a_{Va_aO_b})\right) \tag{4.7}$$

Combining the logarithmic terms in Equation 4.7 into a single logarithm result in the equation:

$$\Delta G = \Delta G^f_0 + RT\ln\left(\frac{a^{ox}_{Me_aO_b}}{(a^{ox}_{Va_aO_b})^b(a^M_{Me})^a}\right) \tag{4.8}$$

The driving force is computed with the assumption that there are no metal ions within the oxide; all the metal sites in the metal sublattice are populated with vacancies. The lack of metal ions in the oxide is from the assumption that is made with Equation 4.2; where the reaction to produce an oxide requires vacancies within the metal sublattice in the oxide. The chemical potential of bulk metal atoms, becoming part of the oxide, is therefore considered an addition to an empty oxide's energy. The reaction products are filled metal and oxygen sublattices of the oxide. Having written the thermodynamic driving force for the reaction in terms of activities Equation 4.8 describes the driving force for oxidation with the mass action law.

Once the reaction describing the metal-oxide interface has been determined, a flux of metal atoms across the interface can be described though a modification of the equation described by Larsson et al. in Equation 4.9 [1].

$$j_i = -\frac{M_i x_i}{V_m}\frac{\Delta\mu_i}{\Delta Z} \tag{4.9}$$

Two simplification steps made by Larsson et al. are not suitable for modelling the growth of an oxide; these are: approximating the molar fraction of the element across the interface between the two interface phases α and β as Equation 4.10 and the assumption that the molar fraction of vacancies within each phase is constant Equation 4.11.

$$x_i = \sqrt{x_i^{\alpha} x_i^{\beta}} \tag{4.10}$$

The reaction rate depends on how much metal is within the oxide phase. As the concentration of metal within the oxide increases, the proportion of metal diffusing into the oxide decreases.

$$\sqrt{x_{Va}^{\alpha} x_{Va}^{\beta}} = constant \tag{4.11}$$

The assumption that the concentration of vacancies is constant is not applicable; as the number of vacancies within the oxide is required to be known and influence the flux of nickel into the oxide phase. The number of vacancies can be determined and vary across the oxide; as they facilitate the diffusion of nickel. Reverting the assumptions made in Equation 4.10 and Equation 4.11 modifies the flux equation to be:

$$j_i = -\frac{M_i}{V_m}\sqrt{x_i^{\alpha} x_i^{ox} x_{Va}^{\alpha} x_{Va}^{ox}}\frac{\Delta\mu_i}{\Delta Z} \tag{4.12}$$

As the concentration of vacancies within the metal is assumed to be constant, the vacancies concentration can also be assumed to be combined into the mobility term. The flux causing oxidation is between the metal within the bulk phase and the vacancies within the oxide phase; the vacancies are assumed to diffuse into the bulk once they reach the metal phase and are not explicitly tracked.

In the present model, the assumption is that new oxide formed on the surface has no metal on the metal sublattice; therefore, the metal concentration in the oxide is 0, and the site fraction of vacancies in the oxide is 1. However, the flux of the reaction is proportional to the number of sites that the metal ions can fill within the bulk oxide; this is described as the molar fraction of vacancies in the oxide x_{Va}. The flux of metal atoms across the interface is computed as follows;

$$j_{Me} = -\sqrt{x_{Me}^{\alpha} x_{Va}^{Ox}} \frac{M_{Me}}{V_m} \frac{\Delta G}{\Delta Z} \tag{4.13}$$

M_{Me} is the inter-facial mobility across the metal-oxide interface. V_m is the molar volume of the system and ΔZ is the grid spacing, ΔG is Equation 4.3 or Equation 4.8. The stoichiometric number of the oxide scales the reaction flux as the flux is for the total number of atoms that could move from the reaction; the oxygen ions are assumed to be immobile, so only consider the metal atom's motion. The assumption that oxygen ions are immobile results from the lack of an understanding of the diffusivity of oxygen within nickel oxide and the lack of a model describing vacancies on the oxygen sublattice.

Taking into consideration the difference in mobility between the bulk metal and the interface Equation 4.13 the pre-factor M^I is added; this describes any increase or decrease in mobility that occurs from the reaction. This value also includes other reactions between the bulk metal and metal in the oxide, such as ionisation from the metal phase. Further, the flux calculated assumes that the oxygen diffuses across the interface; as only metal is diffusing, the flux must be scaled appropriately $\frac{a}{a+b}$. This modifies Equation 4.13 to become;

$$j_{Me} = -\frac{a}{a+b} \sqrt{x_{Me}^{\alpha} x_{Va}^{Ox}} \frac{M_{Me} M^I}{V_m} \frac{\Delta G}{\Delta Z} \tag{4.14}$$

Once the metal atoms have become ions and are part of the oxide, these ions diffuse through the oxide towards the oxide-gas interface; this occurs via a modified version of the diffusion equation used by Larsson et al. [1]. The bulk diffusion flux within the oxide

phase requires adjusting similarly to describe the flux within a bulk phase, the assumption that vacancy concentrations are constant Equation 4.11, with the addition of reverting some of the assumptions that the vacancy content is at local equilibrium:

$$\mu_{Va} = 0 \tag{4.15}$$

Including these two modifications Equation 4.11 and Equation 4.15 related to the vacancies concentration within the reaction describes the flux of atoms within an oxide:

$$j_i = -x_i x_{Va} \frac{M_i}{V_m} \frac{\Delta\mu_i - \Delta\mu_{Va}}{\Delta Z} \tag{4.16}$$

The concentration of vacancies is not explicitly tracked within this model but is determined by knowing the oxygen and metal concentration. Stoichiometry defines the ratio between metal and oxygen. For a simple MeO oxide, the fraction of oxygen to metal must be 50%. Considering a system where vacancies only are present on the metal sublattice. The total fraction of metal and vacancies must be 50% to ensure that all available sublattice sites are occupied; otherwise, the system would have oxygen ions on the metal sublattice. The effective molar fraction (x_i') are the molar fractions scaled to be representative of the different sublattices. For a simple MeO oxide, the effective molar fractions can be written as:

$$1 = x'_{Me} + x'_{Va} + x'_O \tag{4.17}$$

knowing that the ideal value of x'_O should be 0.5, this allows the Equation 4.17 to be simplified, ignoring the oxygen concentration;

$$x'_{Va} + x'_{Me} = 0.5 \tag{4.18}$$

The effective molar fractions must be determined from the concentration of metal and

oxygen within the grid volume. As the stoichiometry of the oxide is known, the relation between the metal and oxygen sublattices is also known. The number of moles on the metal sublattice equals the number on the oxygen sublattice.

$$n_O = n_{Me} + n_{Va} \tag{4.19}$$

The total number of moles occupied by the oxide is $n_{total} = 2n_O$. n_{total} can be used as a different divisor for calculating the molar fraction; this is the effective molar fraction.

$$x_i' = \frac{n_i}{n_{total}} = \frac{n_i}{2n_O} \tag{4.20}$$

Equation 4.20 results in the effective molar fraction of oxygen being 0.5, allowing the actual molar fraction of vacancies and metal to be determined. The number of moles of vacancies can be determined as the difference between the moles in oxygen and metal;

$$n_{Va} = n_O - n_{Me} \tag{4.21}$$

which can be used to determine the molar fraction of vacancies;

$$x_{Va}' = \frac{n_O - n_{Me}}{2n_O} \tag{4.22}$$

Equation 4.16 should be rewritten in terms of effective molar fractions defined in Equation 4.20 as ordinarily the vacancy concentration is not explicitly tracked, this now becomes;

$$j_i = -x_i' x_{Va}' \frac{M_i}{V_m} \frac{\Delta\mu_i - \Delta\mu_{Va}}{\Delta Z} \tag{4.23}$$

Within the bulk oxide diffusion occurs by ionic species moving into metal vacancy sites, the mobility equation calculation for ionic diffusion [257] takes into consideration the valency

of species k (Z_k) and the charge on an electron (Q_e). D_0 is the diffusivity coefficient, and Q is the activation energy.

$$M_k = \frac{Z_k Q_e}{kT} D_0 \exp\left(\frac{-Q}{RT}\right) \tag{4.24}$$

The oxide-gas interface is controlled by the oxygen becoming included as part of the oxide phase. This process can be represented as three steps [182]. Initially, molecular oxygen becomes adsorbed onto the oxide surface on-site S; this reaction occurs at a rate k_a,

$$O_2(g) + S \overset{k_a}{\rightleftharpoons} O_2|S \tag{4.25}$$

The adsorbed molecular oxygen then subsequently splits into atomic oxygen at the oxide interface; this requires another adsorption site S; this reaction occurs at a rate k_b,

$$O_2|S + S \overset{k_b}{\rightleftharpoons} O|S + O|S \tag{4.26}$$

Atomic oxygen that is adsorbed onto the oxide surface becomes part of the oxide and takes into consideration the ionisation of the oxygen atoms; this occurs at a rate k_c,

$$O|S \overset{k_c}{\rightleftharpoons} oxide \tag{4.27}$$

Equation 4.27 can be combined with the number of available adsorption sites; M, to derive a rate of oxygen addition into the oxide. Where M is 10^{15}cm^{-2};

$$rate = \frac{M k_c (k_a k_b)^{\frac{1}{2}} P_{O_2}^{\frac{1}{2}}}{1 + (k_a k_b)^{\frac{1}{2}} P_{O_2}^{\frac{1}{2}} \left[1 + (\frac{k_a}{k_b})^{\frac{1}{2}} P_{O_2}^{\frac{1}{2}}\right]} \tag{4.28}$$

the full derivation is described within [182]. Where P_{O_2} is the partial pressure of oxygen, this oxygen addition rate can be simplified by the assumption that at higher partial pressures of oxygen, the rates of molecular and atomic oxygen need to be considered; if

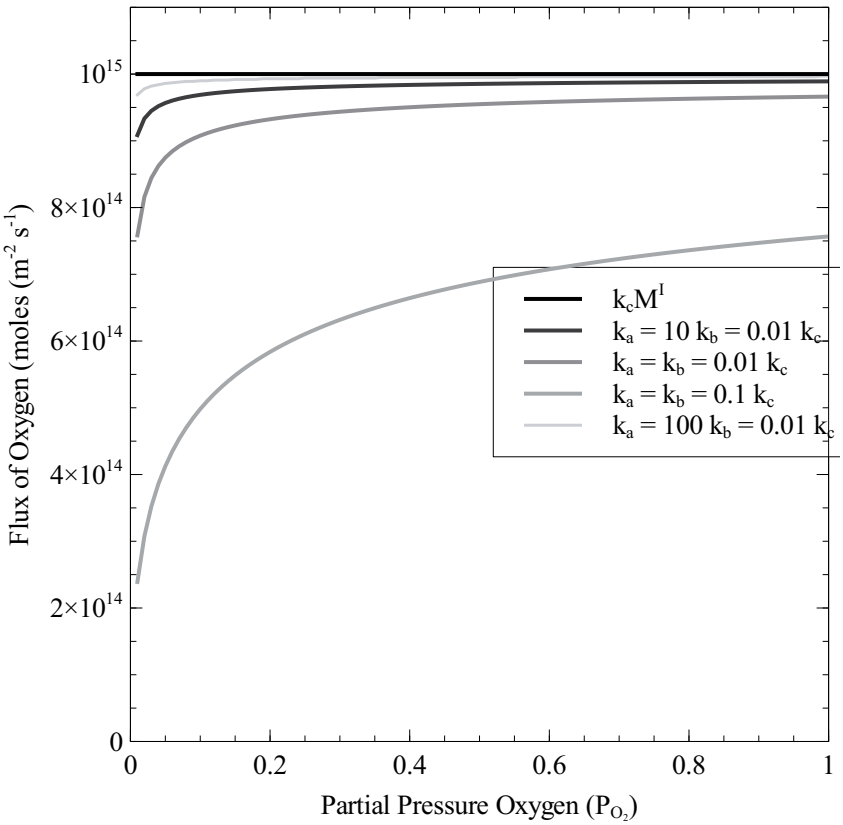

Figure 4.1: Figure showing the rate of oxygen addition to the oxide for both Equation 4.28 and Equation 4.29 (from [182]); showing the difference between the two for 4 different combinations of different rate constants k_a and k_b. At higher pressures, the difference between the majority of the curves is small; less than 2%; this assumption simplifies the equations to have one unknown rather than three.

the rate of atomic adsorption is greater than molecular adsorption then $\left(\frac{K_a}{K_b}\right)^{\frac{1}{2}} P_{O_2}^{\frac{1}{2}} << 1$. The term in the square brackets (Equation 4.28) is therefore approximately 1. If the surface is saturated by oxygen atoms and molecules ($(K_a K_b)^{\frac{1}{2}} P_{O_2}^{\frac{1}{2}} >> 1$) which reduces the oxygen addition rate to be (c.f. Figure 4.1)

$$rate = K_c M \tag{4.29}$$

Using this simplified rate equation can be turned into a flux of moles j_O by dividing by Avogadro's (N_A) constant to turn atoms into moles.

$$j_O = \frac{K_c M}{N_A} \tag{4.30}$$

The flux of oxygen ingress into the oxide Equation 4.30 only occurs when the metal concentration at the oxide-gas interface is sufficiently high; oxygen will only be added to the surface provided that there are filled metal sublattice sites. If the sites are not filled, this describes the adsorbed oxygen on the surface, preventing further oxygen from joining the oxide surface. The number of vacancies on the substrate is the difference between the moles of oxygen and metal

$$n_{Va} = n_O - n_{Me} \tag{4.31}$$

The number of moles of vacancies is modified into a volume assumed to be a single atom thick. An adjustment to ensure that oxygen is only added when the concentration of vacancies is set at 0.01 and describes unconsidered factors such as how covered in oxygen ions the surface of the material is

$$\frac{V_m}{200 r_{O^{2-}} A} (n_O - n_{Me}) \tag{4.32}$$

Putting Equation 4.32 into an exponential provides an equation that describes the addition

of oxygen at the gas-oxide interface; oxygen is added faster with a lower concentration of vacancies present at the interface. Figure 4.2 shows the total flux of oxygen at the oxide-gas interface;

$$\Delta n_O = \frac{K_c M}{N_A} A \Delta t \exp\left(\frac{-V_m(n_O - n_{Me})}{200 r_{O^{-2}} A}\right) \tag{4.33}$$

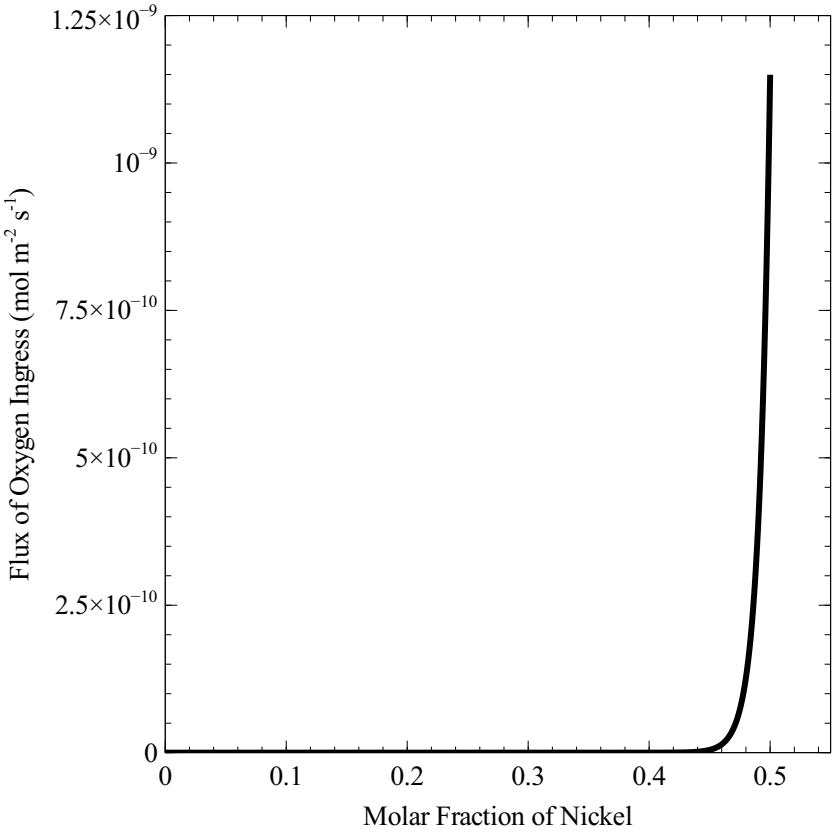

Figure 4.2: Relationship between the oxygen ingress into the oxide and the molar fraction of nickel at the oxide-gas interface (Equation 4.33). As the molar fraction of nickel reaches 0.5, the rate at which oxygen is added to the oxide increases; at around 0.45 molar fraction of nickel, the oxygen addition is reduced significantly.

where N_O and N_{Me} are the number of moles of oxygen and metal at the oxide-gas interface respectively; $r_{O^{2-}}$ is the ionic radius of an oxygen ion 140pm [257]. How these different reactions and diffusion fluxes occur along with where they act is represented in Figure 4.3, highlighting the motions of the different species within the simulation.

The fluxes from the different reaction steps are converted into a change of moles by;

$$\Delta n_i = \Delta t A j_i \tag{4.34}$$

where A is the interfacial area, Δt is the time step for the simulation, and N is the number of moles.

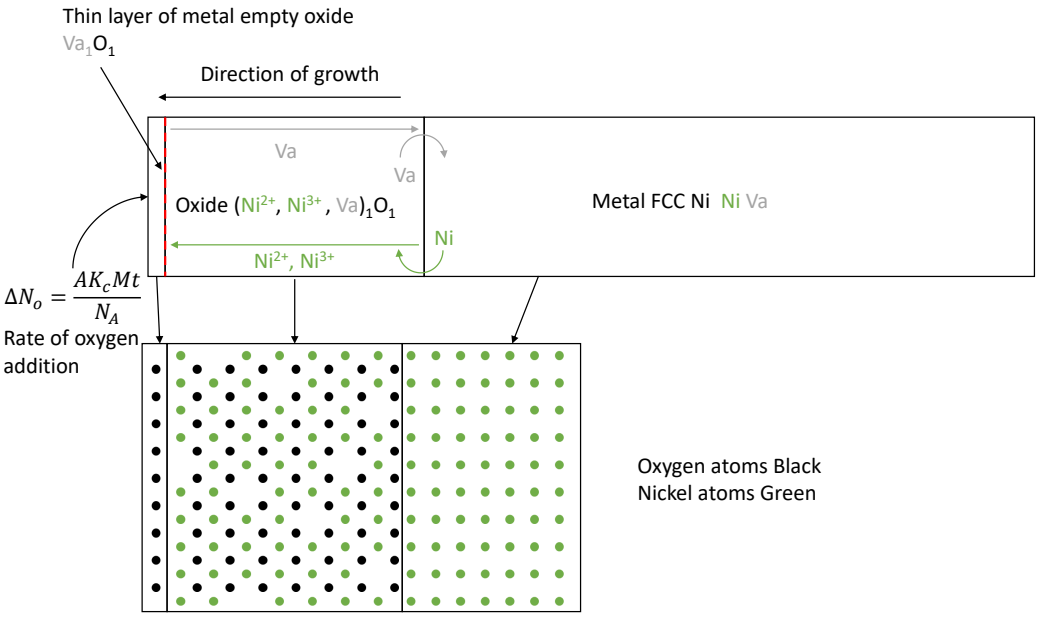

Figure 4.3: Schematic showing the simulation design with the three distinct phases; gas, oxide and metal. The oxygen-gas interface assumes that as oxygen is added to the oxide, it forms a thin layer of oxide on the surface with an empty metal sublattice, which is subsequently filled by metal diffusing into the layer from the bulk oxide. As the concentration of metal within the bulk oxide is diluted from oxygen, adding more metal diffuses into the oxide phase from the bulk metal at the metal-oxide interface. This interface takes the vacancies created when the oxygen adds onto the surface of the oxide and moves them into the bulk metal, where they diffuse to vacancy sinks.

The numerical scheme can be adapted to simulate a multi-element oxide; this requires changing the metal-oxide interface in Equation 4.14. This adaption does not allow for there to be multiple oxides that are grown; simply, it allows the composition of the resulting oxide to be modified by determining the rate of each metal that crosses the interface. The oxide-metal interface reactions are split into the individual elements, and the fluxes are correspondingly calculated;

$$\Delta G_i = \mu^{ox}_{i_aO_b} - \frac{b}{a+b}\mu^{ox}_{Va_aO_b} - \frac{a}{a+b}\mu^{\alpha}_i \tag{4.35}$$

The metal flux defined within Equation 4.14 describes how a single metal moves across the phase interface. The concentration of the metal that moves across the interface is simplified to be the elements site fraction y_{f_i}.

$$j_i = -y_{f_i} \frac{a}{a+b} \sqrt{x_i^{\alpha} x_{Va}^{Ox}} \frac{M^I M_i}{V_m} \frac{\Delta G_i}{\Delta Z} \tag{4.36}$$

The total flux is also scaled for a fraction of all elements that can move onto the sublattice.

4.2.2 Parameters and Implementation

The numerical scheme outlined in this work does not include the mechanism for oxide nucleation; therefore, a small layer of oxide is assumed to have already formed on the surface and is allowed to grow. A single thin slice of oxide is present with a small molar fraction of metal ions (1×10^{-20}). The oxide region is attached to a large section of nickel metal (1000μm); this region is divided into 1μm simulation volumes with a fixed cross-sectional area and is made up of pure nickel metal. On the edge of the outer oxide layer, oxygen ions are added to the oxide.

Bulk diffusion within the metal phase follows the original work by Larsson et al. [1] (Equation 4.9) and the equation describing the metal-oxide interface is Equation 4.16 and the oxide-gas interface is described by Equation 4.33. The fluxes, once calculated, are turned into a change of moles by Equation 4.34. The numerical scheme is computed using an explicit finite difference scheme.

In order to enhance the stability of the oxide growth, as the metal concentration within the oxide cannot exceed that of the oxygen concentration, the metal-oxide interface can result in too much metal diffusing into the region. If the amount of metal diffusing in a single time-step is too large, then the diffusion region is calculated at 0.1 times that of the original time-step to enable the model to simulate the appropriate oxygen concentration in the oxide. Reducing the time step by a factor of 10 helps to avoid the concentration of metal becoming greater than 50%; this is nonphysical, and the simulation cannot describe such a state.

The *fcc* phase of the binary simulation was comprised of 1 mole of nickel. Thermodynamics for the simulations are computed using the compound energy formalism [210] and use the

CALPHAD assessment [258]. The activation energy for Nickel diffusion in nickel oxide was used as 225kJmol^{-1} [259–261], the diffusivity coefficient used was 1.7×10^{-6}m^{2}s^{-1} [259, 261]. The activation energy for nickel self diffusion in the *fcc* phase was 287kJmol^{-1} and the diffusivity coefficient was 9.2×10^{-5}m^{2}s^{-1} [262].

Ternary simulations were set up in a similar way to the binary scheme. The *fcc* phase has a composition of 0.9 moles of nickel and 0.1moles of chromium. The thermodynamics were defined by the CALPHAD assessment [258]. The diffusivity coefficient for Chromium within nickel oxide was taken as 8.6×10^{-7}m^{2}s^{-1} and the activation energy as 282kJmol^{-1} [263]. The diffusivity coefficient for chromium in the *fcc* phase was used as 1.4×10^{-4} m^{2}s^{-1} and an activation energy of 278.2kJmol^{-1} [264].

Grid volumes dynamically resize depending on the number of moles within each volume. As the area is fixed in size, this simulates a 1-dimensional domain. These simulation volumes can dynamically split and join depending on the size. When a volume is 30% above its original starting volume, it is split into two equal volumes of half the size; if a volume is 30% of its original size, the volume is joined onto another volume of the same phase. This scheme cannot be used for the initial thin slice of oxide until the oxide slice has a thickness greater than 30% of the bulk slice to prevent the oxide from being prematurely incorporated into the bulk; this is the same as what is described within [1].

A few unknowns may influence the oxidation reaction that is not present within the literature; these are the rate k_c and the rate between the oxide and metal phases. As the diffusion of nickel in oxide is the rate-limiting step in the oxidation reaction, it is not easy to measure the rate k_c as the process happens too quickly. The rate at which a metal atom is ionised and becomes part of oxide is too quick to measure. This work considers these effects by adjusting the interface mobility M^I.

To test a variety of different parameters the values k_c and M^I are varied for temperature ranges of 1000°C to 1200°C in 100°C increments. k_c is varied between 0.01 and 100 in powers of 10, and M^I is varied between 1×10^{-5} and 1×10^{-4} in powers of 10. These unknown values seek to find the lower limit of such values; These processes defining both

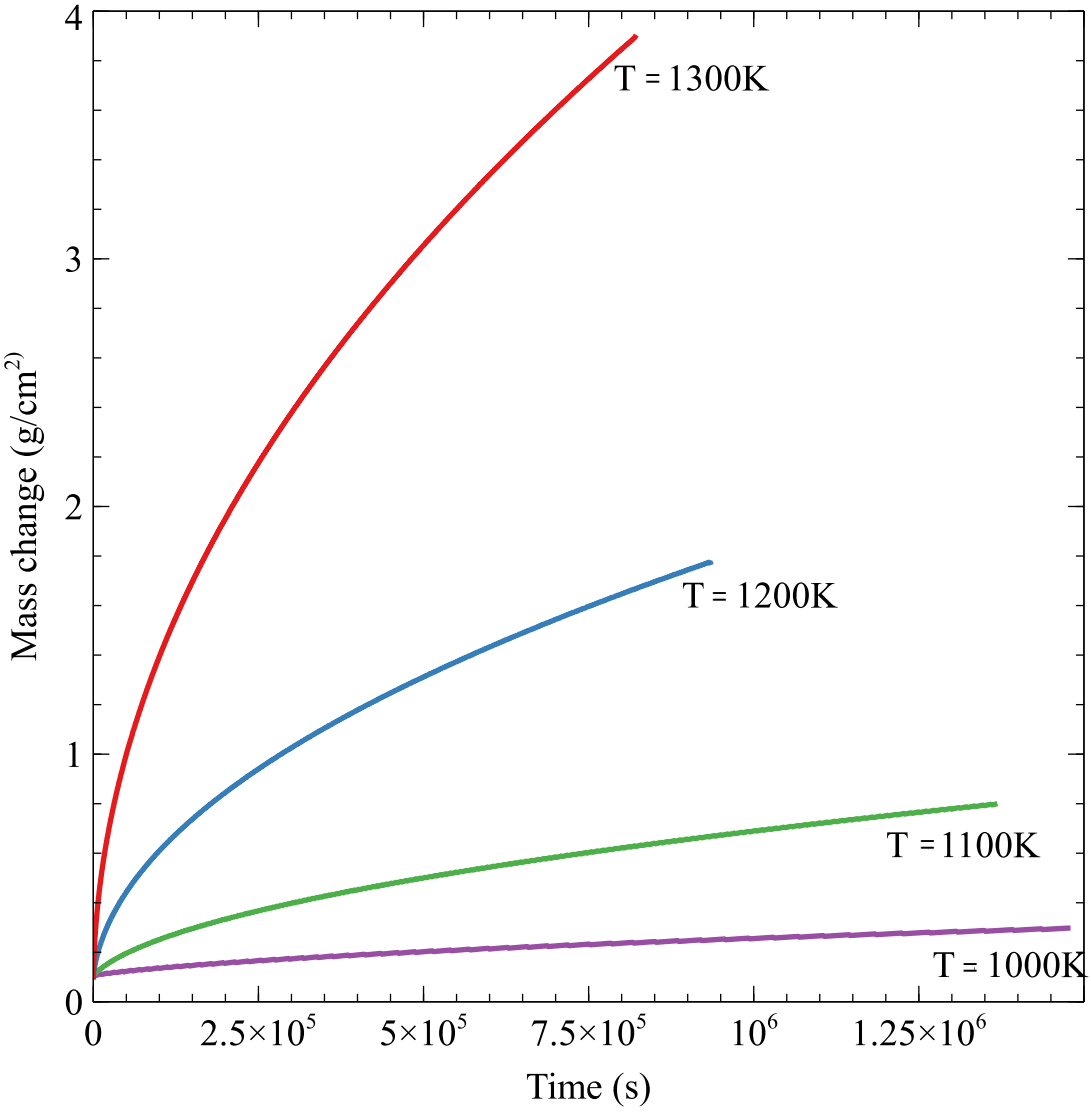

Figure 4.4: Oxidation rate against time for simulations at a range of temperatures 1000-1300K. The oxidation simulations were run with values k_c of 1 and M^I 1×10^{-4}. As the temperature increases, the rate of oxidation increases; at 1000K, the oxidation rate is reduced and closer to linear than parabolic oxidation.

interface reactions cannot fully describe how the oxidation process occurs.

4.3 Results

The simulations can determine the oxide thickness and mass change from the oxide growth, similar to that of a parabolic growth curve. Additionally, the simulation gives an idea of nickel concentration through the oxide phase; there is a slight decrease in concentration near the oxide-gas interface and an increase in concentration near the metal-oxide interface.

4.3.1 Oxidation of nickel

The oxidation reactions were used to determine the K_p of each temperature and the k_c and M^I. This data was compared against the data from [2]; this data includes oxidation at a range of temperatures and pressures for pure oxide; the experimental set-up is assumed to be the same, and therefore, the data is comparable.Figure 4.5 Shows a similar oxidation rate with the data in [2] between k_c values of $10s^{-1}$ and $100s^{-1}$ for oxidation simulations performed at 1000°C .

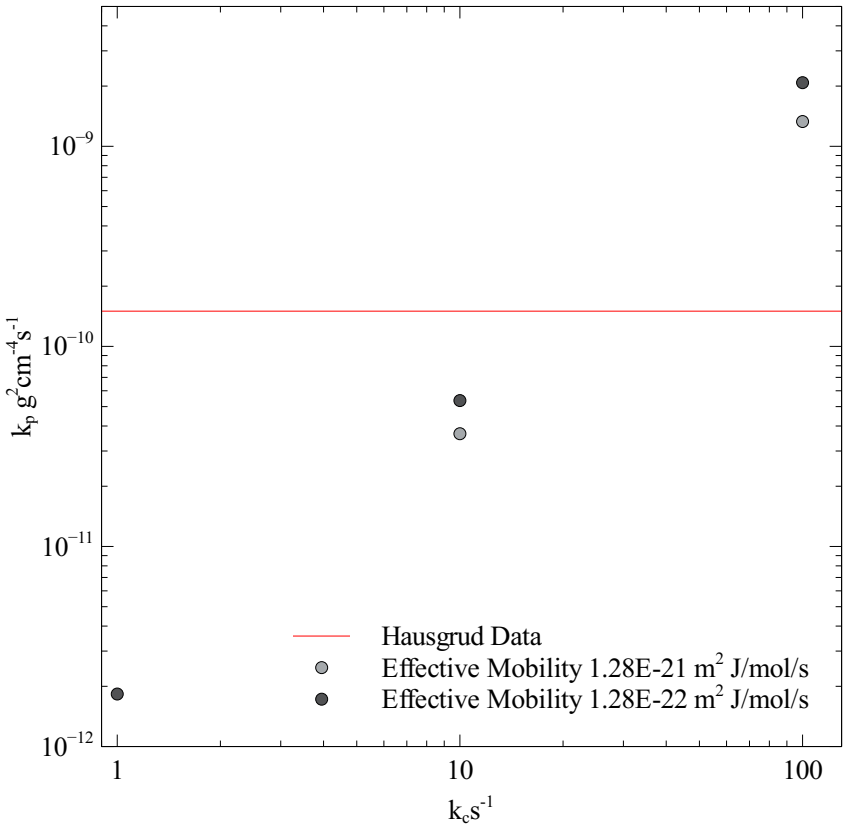

Figure 4.5: Plot of K_p against time comparing computed oxidation rates and the data at 1000°C in [2]. The effective mobility considers the mobility pre-factor M^I. The mobility pre-factor has a relatively negligible effect on the rate of the reaction; but the value of k_c lies between $10s^{-1}$ and $100s^{-1}$ for an oxidation temperature of 1000°C .

Simulations results to provide more detail between k_c values of $10s^{-1}$ and $100s^{-1}$ which were determined from Figure 4.5 as being the closest fit to experimental data. Figure 4.6 shows simulations that have been performed for k_c increments of $10s^{-1}$ between $10s^{-1}$ and $100s^{-1}$. A power law has been used to fit the data to determine the ideal value of k_c to produce the same resulting oxidation rate as [2]. Values of k_c of $18.9s^{-1}$ for a value of M^I

of 1×10^{-4} and 17.9s^{-1} for a value of M^I of 1×10^{-5}.

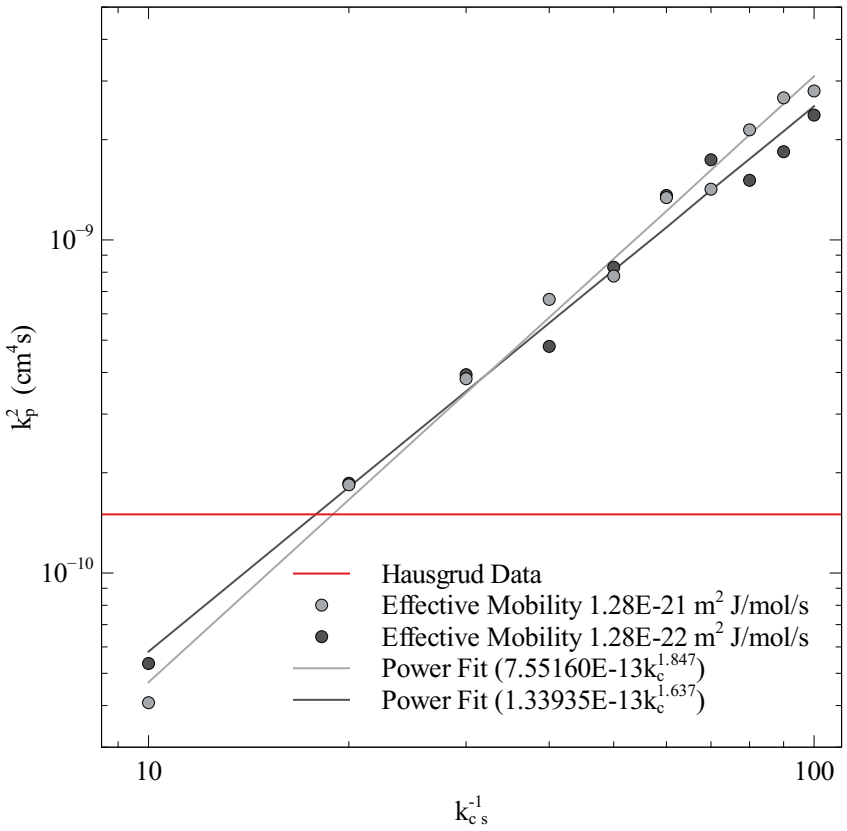

Figure 4.6: Plot of K_p against time comparing computed oxidation rates and the data at 1000°C in [2]. Investigating which value of k_c best describes parabolic oxidation for 1000°C from the data provided in [2]; including the power law fit for the simulated data; this gives an estimation as to what k_c could be; 18.9s^{-1} and 17.9s^{-1} for an effective mobility of 1.28×10^{-21}m^{2}J/mol/s and 1.28×10^{-22}m^{2}J/mol/s respectively.

Oxidation simulations performed at 1100°C show a similar oxidation rate with the data in [2] shown in Figure 4.7 by the k_c values of 10s^{-1} and 100s^{-1} resulting in a k_p value below and above that of Haugsrud et al. [2] respectively.

Simulations results which provide more detail between k_c values of 10s^{-1} and 100s^{-1} which were determined from Figure 4.7. Figure 4.8 shows simulations that have been performed for k_c increments of 10s^{-1} between 10s^{-1} and 100s^{-1}. A power law has been used to fit the data to determine the ideal value of k_c to produce the same resulting oxidation rate as [2]. Values of k_c of 30.5s^{-1} for a value of M^I of 1×10^{-4} and 30.1s^{-1} for a value of M^I of 1×10^{-5}.

Oxidation simulations performed at 1100°C ; Figure 4.9 shows a similar oxidation rate with the data in [2] between k_c values of 10s^{-1} and 100s^{-1}.

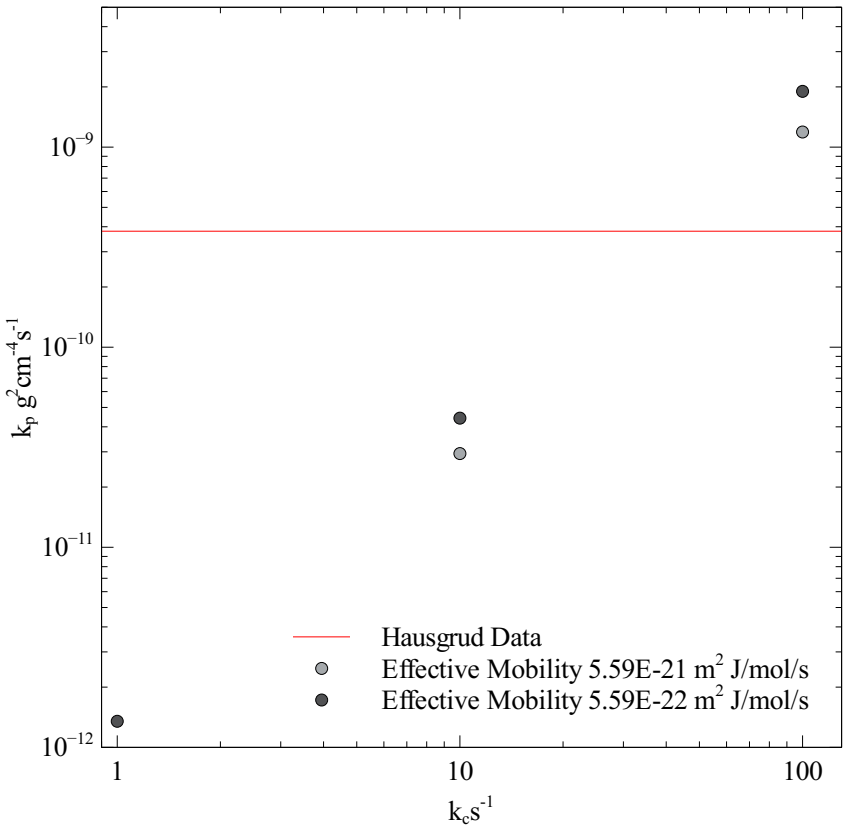

Figure 4.7: Plot of K_p against time comparing computed oxidation rates and the data at 1100°C in [2]. For two different effective mobilities and a range of different k_c values, the data which best matches the data provided by [2] is between a k_c value of $10s^{-1}$ and $100s^{-1}$.

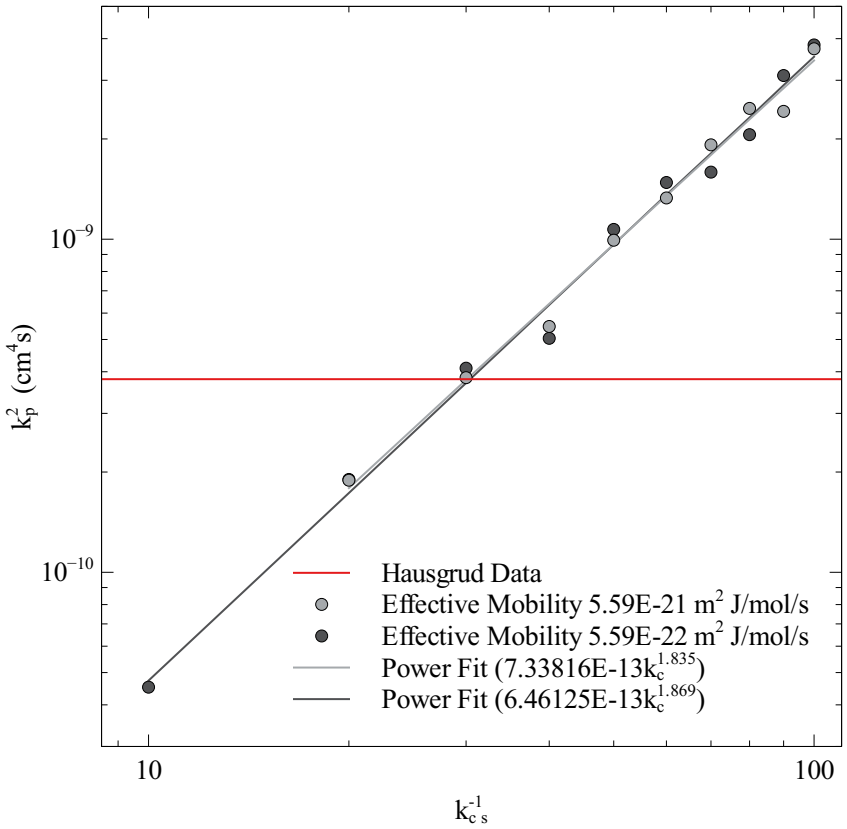

Figure 4.8: Plot of K_p against time comparing computed oxidation rates and the data at 1100°C in [2]. Finer detail between k_c values of $10s^{-1}$ and $100s^{-1}$ to determine a more approximate value of k_c for the two effective mobilities. The k_c values that best correspond to the oxidation rate described by [2] are $30.5s^{-1}$ and $30.1s^{-1}$ for an effective mobility of $5.59 \times 10^{-21}m^2J/mol/s$ and $5.59 \times 10^{-22}m^2J/mol/s$ respectively.

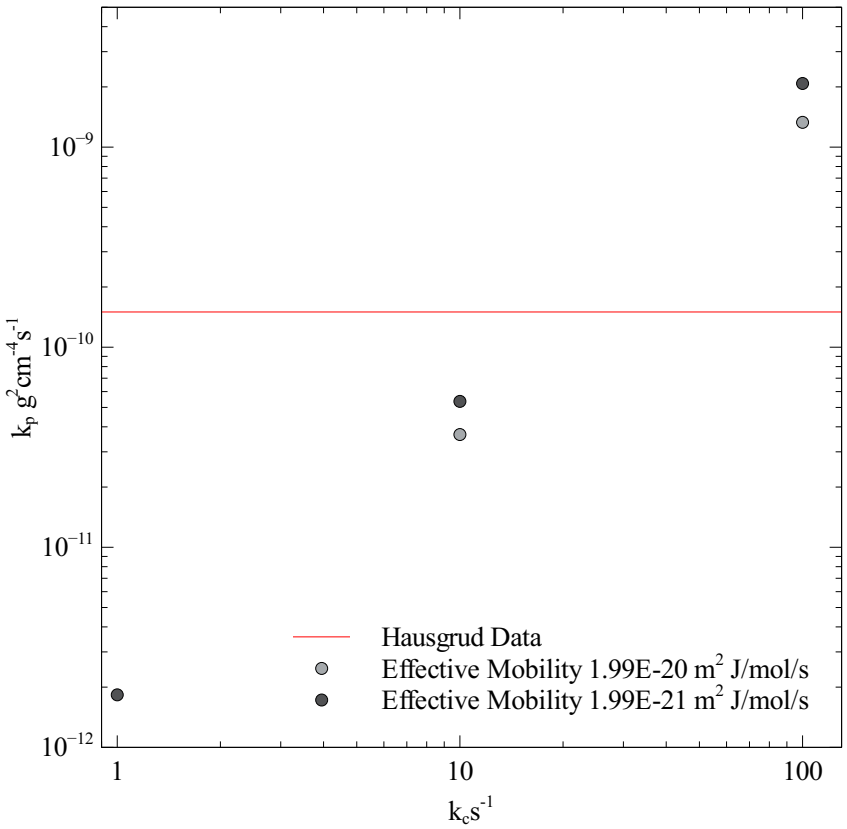

Figure 4.9: Plot of K_p against time comparing computed oxidation rates and the data at 1200°C in [2]. Two different effective mobilities and a range of k_c values are used to approximate the actual value of k_c at set effective mobilities. The value of k_c is between a k_c value of $10s^{-1}$ and $100s^{-1}$.

Simulations results which provide more detail between k_c values of $10s^{-1}$ and $100s^{-1}$ which were determined from Figure 4.9. Figure 4.10 shows simulations that have been performed for increments of $10s^{-1}$ between $10s^{-1}$ and $100s^{-1}$. A power law has been used to fit the data to determine the ideal value of k_c to produce the same resulting oxidation rate as [2]. Values of k_c of $58.6s^{-1}$ for a value of M^I of 1×10^{-5}.

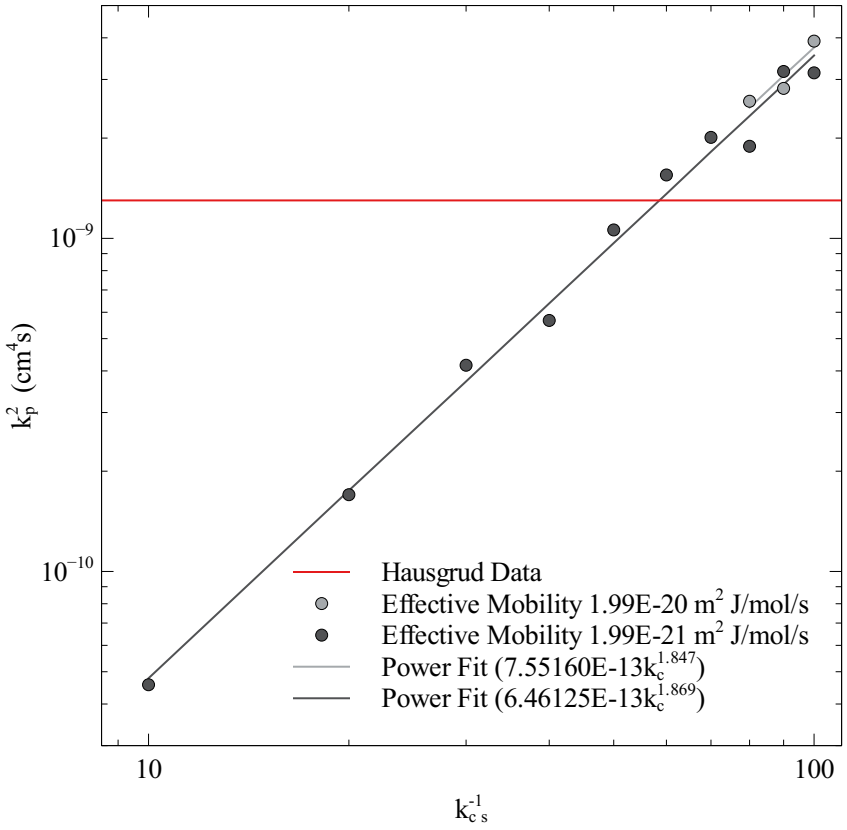

Figure 4.10: Plot of K_p against time comparing computed oxidation rates and the data at 1200°C in [2]. More simulation results for k_c values between $10s^{-1}$ and $100s^{-1}$ for two effective mobilities; the value of k_c from the power law fit has been determined to be $58.6s^{-1}$ for an effective mobility of $1.99 \times 10^{-21}m^2J/mol/s$, to match the data in [2]. The higher effective mobility does not have sufficient data to determine what effective mobility could be without excessive extrapolation.

The table of data for both M^I values including the predicted k_c values for all three tested temperatures are presented in Table 4.1 and Table 4.2. The value for k_c is missing at the M^I value of 1×10^{-4} at 1200°C due to the extrapolation to produce the power law fit. There was insufficient data to determine what the appropriate power law might be around the point such that it matched the given data from [2].

The power law fit for k_c at different temperatures are different but provide agreement in their values; the closeness in k_c values may be the result of experimental variations within

Table 4.1: Power law values for an M^I value of 1×10^{-4} following the equation Ak_c^x with the k_c value that would produce the same oxidation rate as the data in [2]. The computed k_c value increases as temperature increases; however, very similar values for A and x from the power law fit of ±2.8% and ±0.75% respectively.

Temperature (°C)	A	x	k_c
1000	7.14E-13	1.819	18.9
1100	7.34E-13	1.835	30.1
1200	7.55E-13	1.847	

Table 4.2: Power law values for an M^I value of 1×10^{-5} following the equation Ak_c^x with the k_c value that would produce the same oxidation rate as the data in [2]. The computed k_c value increases as the temperature increase the values of A and x are relatively similar at temperatures of 1100°C and 1200°C but are different at 1000°C ; this could show a difference in oxidation reactions at lower temperatures from being more oxygen limited than oxygen limited.

Temperature (°C)	A	x	k_c
1000	1.34E-12	1.637	17.9
1100	6.34E-13	1.835	30.5
1200	6.49E-13	1.869	58.6

Hausgruds data. The power law fit for k_c at 1100°C is used to predict what the k_c value would be for all temperatures k'$_c$. The values are plotted in Figure 4.11. The gradient can be used to determine a more representative power law fit for this data; a single k_c equation for matching closer to experimental data. The highlighted data point indicates an extrapolated data point as the simulation was not stable to match experimental data. For an M^I value of 1×10^{-4} the best fit from Figure 4.11 is $kc = 1.0858k_c' - 2.46$; this results in the equation for k_c being

$$k_c = 1.0858 \left(\frac{k_p}{7.34 \times 10^{-13}} \right)^{\frac{1}{1.835}} - 2.46 \tag{4.37}$$

At the lower mobility M^I 1×10^{-5} the best fit from Figure 4.11 is $kc = 1.1014k_c' - 1.2916$; this results in the equation for k_c being

$$k_c = 1.1014 \left(\frac{k_p}{6.34 \times 10^{-13}} \right)^{\frac{1}{1.835}} - 1.2916 \tag{4.38}$$

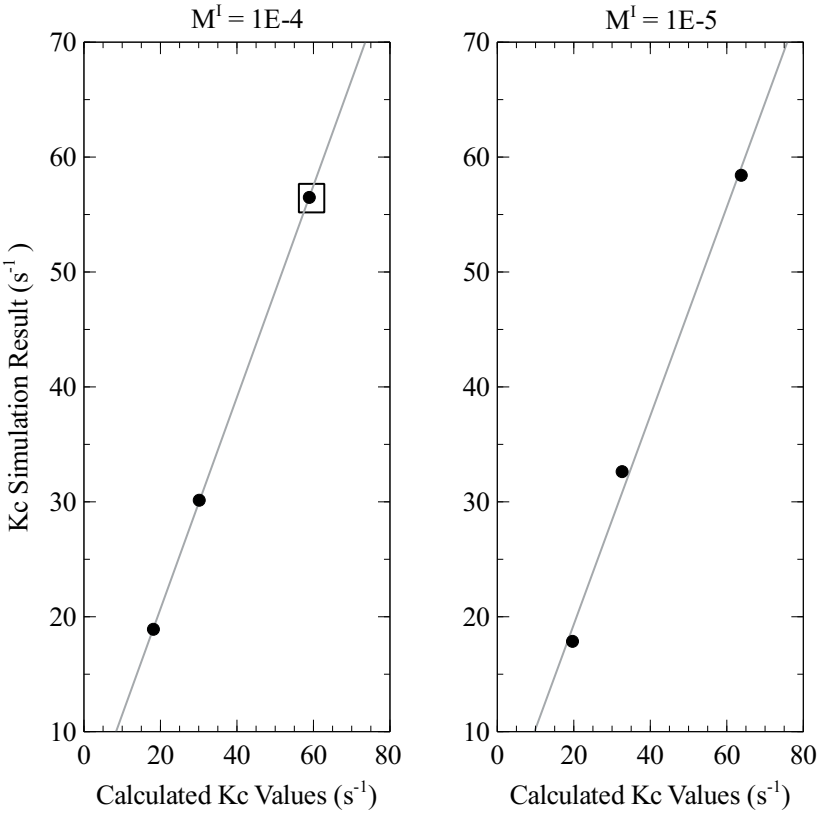

Figure 4.11: Graph determining the relation between the actual k_c value determined from the simulation and the k_c value computed from the power law fit. This is used to determine what the value of k_c is from the parabolic rate constant k_p of (4.37) and (4.38) for the mobility pre-factors M^I of 1×10^{-4} and 1×10^{-5} respectively. At a M^I value of 1×10^{-4} and a k_c value around 60, which is marked on the graph; this is an extrapolated data point and so may be inaccurate which has an influence on the k_c vs k_p equation (4.37).

4.3.2 Ternary Oxidation

The growth of a ternary oxide was simulated with little success; some instabilities in the simulation resulted in insufficient data for analysis. The intention was to understand how Cr influenced the formation and resulting oxidation rate of oxidation. Simulations show the beginnings of the simulation as both Cr and Ni diffuse into the oxide to simulate oxide growth. Figure 4.12 is the last concentration profile before the simulation was unstable; at which point it was unable to produce any meaningful results.

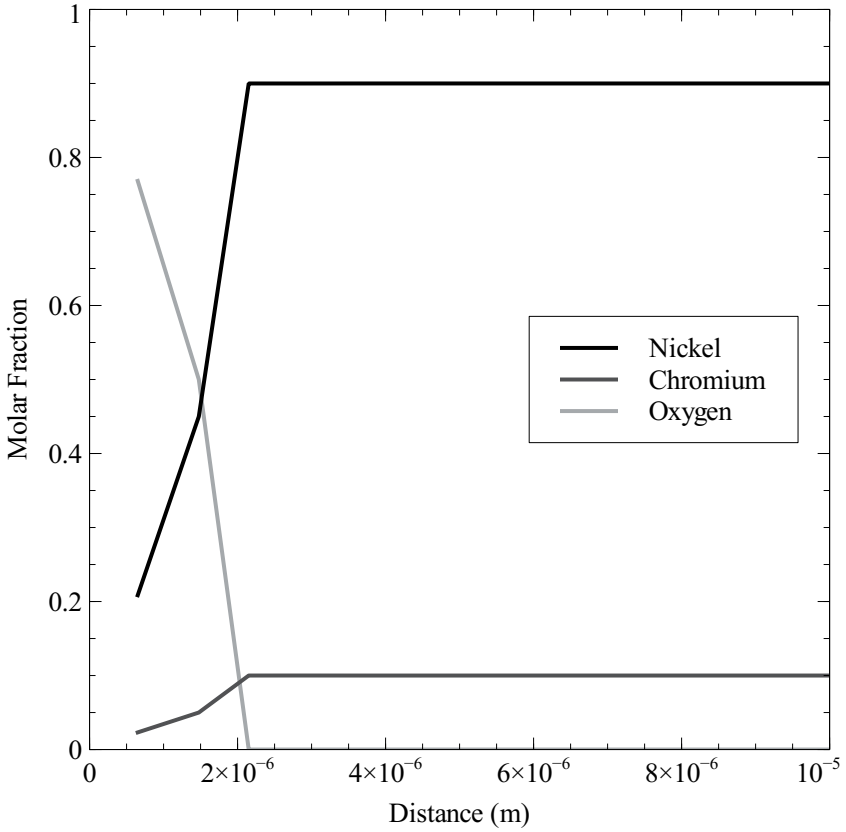

Figure 4.12: Concentration profile for a ternary oxide growth of Ni-Cr-O; using (4.36). Only a small amount of oxide is produced during the reaction before the simulation becomes unstable and cannot produce sufficient oxide.

4.4 Discussion

The numerical simulations can reproduce similar oxidation rates (K_p). The simulations are varied in three different conditions; the value of k_c; the rate at which oxygen becomes part of the oxide. The mobility at the metal-oxide interface and the temperature. Figure 4.5,

Figure 4.7 and Figure 4.9 show data validation at 1000, 1100 and 1200°C respectively, with the starting parameters of k_c between $10s^{-1}$ and $100s^{-1}$; M^I of 1×10^{-4} and 1×10^{-5} produce data that matches closest with the experimental data from [2]. Further detail for all temperatures are shown in Figure 4.6, Figure 4.8 and Figure 4.10 between the k_c values of $10s^{-1}$ and $100s^{-1}$ in increments of $10s^{-1}$ to give a greater insight into what value of k_c produces oxidation rates that match experimental data.

Power laws with the form Ak_c^x have been fitted to the higher detailed simulations to estimate the k_c value that would produce oxidation that matches experimental data. The power law values are comparable at a M^I value of 1×10^{-4}; the variation for the prefix and exponent agree with differences of $\pm 2.8\%$ and $\pm 0.75\%$ respectively. Table 4.1 contains the simulations power law fit values, however the value at 1200°C is not known fully as the simulations did not provide enough information; due to simulation instability. Table 4.2 contains the power law fit value for a value of M^I these values match closer between temperatures 1100°C and 1200°C with a greater difference at 1000°C . This difference is from a difference within the mechanism for the oxidation reaction; it is likely a result of a decreased oxygen concentration, changing the mechanism from being diffusion-limited to oxygen-limited.

In oxidation science, comparisons of the K_p values of materials are the standard way to compare oxidation behaviour; therefore, the values that are used for comparison given in [2] do not provide a suitable validation for this numerical model. The standard reporting does not consider how close the experimental data was to being parabolic and instead forces the data to be assumed to be parabolic. The numerical simulations fit closely with the K_p value but may simulate a linear oxidation process. An approximation for what equation would represent the value of k_c for the range of M^I values shows a slight linear increase. There is insufficient data to determine whether the variation is experimental or if the k_c value increases with temperature. If experimental data included the parabolic number n determined from the experiments, this would provide greater confidence in the numerical simulation's ability to model a real-world oxide.

Simulations that ran with a M^I greater than 1×10^{-4} were unstable and resulted from the metal-oxide interface becoming diffusion limited rather than reaction limited. The diffusion of nickel across the interface was sufficiently fast that the diffusion within the oxide bulk was insufficient to remove the metal that was added, resulting in a non-stoichiometric compound that was un-computable with the assumption of no vacancies on the oxygen sublattice.

The determined value for M^I and k_c are upper bounds for what possible values these might be. By allowing the simulation to become rate-limited by one of these values, the other value is not influencing how the reaction occurs. To provide an idea of what effect each value has on the reaction rate requires the interface reactions to be the rate-limiting step, which is a process that cannot be determined for both values.

Attempts at developing the oxide-metal interface description to simulate the growth of a ternary oxide; Figure 4.12 shows the simulation before it becomes unstable. This lack of stability results from the complexity of different diffusing elements' ionization within the oxide phase. The addition of an element without variation in ionization state, such as chromium, is added into the oxide; the charge balance is not maintained through the defined method. The lack of charge balance causes the simulations to become unstable; this only manifests itself as the concentration of vacancies is depleted in the oxide to be sufficiently low to allow a single flux of metal into the oxide to break the number of vacancies on the metal sublattice and equally the charge balance.

Other CALPHAD databases based on simple oxide stoichiometries were looked for to investigate this modelling technique's ability to simulate more than just nickel. Work by Chen [265] to develop a cobalt CALPHAD assessment assumed that any variation of cobalt on the metal sublattice within CoO was negligible. This assumption results in the CALPHAD assessment being unsuitable for this modelling technique, as the technique is based on the variations within the metal sublattice. When considering more complex alloy systems, understanding how elemental additions influence the diffusivity of the base metal and the additional alloying elements is essential to model experimental data accurately.

To assist further with greater understanding and refinements to the numerical scheme discussed within this chapter could be aided by experimental data stating what parabolic exponent was gathered from the experimental data to ensure a greater comparison in terms of the data fitting.

4.5 Conclusion

A numerical model has been developed to simulate the growth of nickel oxide; this work considers the reactions at the metal-oxide and oxide-gas interfaces. Nickel oxide has been chosen for the study due to the availability of experimental data and the well-studied system. The computational data has been used to compare to experimental data [2] which has been used to validate this model and give an idea of the unknown variables k_c and M^I. The interface mobility modifier was found to be suitable for both 1×10^{-4} and 1×10^{-5} times the bulk metal diffusivity, the rate for oxygen addition k_c was determined to be Equation 4.37 and Equation 4.38 respectively. Validation with experimental data was conducted in the standard manner for comparing oxidation simulations; however, this approach misses certain information; the parabolic number n would increase the confidence within these results. The simulation of ternary oxide growth was simulated but was not stable enough to produce any results.

Chapter 5

Phase Field Model of Nickel Oxide Growth

5.1 Introduction

Phase field models have been in development since Kobayashi's work in the 1990s [229, 230]; this work described the growth of a dendrite through a series of simple equations. This foundation has led to phase field models being used to simulate a wide range of metallurgical effects [104, 105, 227] with growing interest in a range of other areas of science [225, 232, 233].

The existing oxidation phase field model was developed by Kim [97]; this model builds on the work by Guyer [236], which is a charge-dependent model describing the oxidation process by the motion of electrons and holes. This work is built on the MOOSE framework. The work developed by Guyer is computationally intensive and is complicated to solve in 1-dimension; as such, the work by Kim et al. [97] uses several strategies within the MOOSE framework to enable massively multi-threaded workloads that are used to describe the oxidation process. The model developed by Kim et al. is also limited to not simulate the growth of multi-element systems because of how diffusers are defined.

This work seeks to develop the work described in Chapter 4 seeking to convert the sharp

interface model into something suitable to be described by a phase field model. This technique enables the simulation to be scaled to consider more complex shapes and higher dimensions as the grid volumes are fixed volume. Moving the work in Chapter 4 to a phase-field model allows the inclusion of other contributions in terms of grain boundaries and stress into the model developed within the literature. The currently available phase-field models used within the literature are not defined in a manner suitable for using standard thermodynamic and kinetic principles used within the sharp-interface numerical models. To produce a phase-field model capable of using work in Chapter 4; the creation of a phase-field model defined with physical parameters in mid is developed.

The model developed within this thesis seeks to be a part of a more comprehensive collection of phase-field models that can provide users with a more comprehensive and complete understanding of oxidation. Due to the ability to combine multiple phase-field models, other material effects important to understand regarding oxidation can be included and combined to give a more full and comprehensive numerical result. Other material effects to be considered are stress-strain, grain boundaries and temperature effects, to name a few.

5.2 Methodology

A phase field model has been developed based on the work by Larsson et al. [1, 249, 250], building upon the principle that an interfaces velocity, v, can be tracked from the sum of the fluxes across a phase interface;

$$v = -V_m \sum j_i^{\alpha\beta} \tag{5.1}$$

where the flux used in Equation 5.1 across the phase interface is the flux defined within the work by Larsson et al. [1];

$$j_i^{\alpha\beta} = -\frac{M_i x_i}{V_m} \frac{\Delta \mu_i^{\alpha\beta}}{\Delta z} \tag{5.2}$$

This method aims to create an expression for the driving force of the atomic flux across the interface in a consistent phase-field manner. The velocity of a phase field interface is defined as the product of the interfacial mobility μ and the thermodynamic driving force ΔG. This expression links the velocity in Equation 5.2 to phase field variables ϕ [219];

$$v = \frac{\dot{\phi}}{|\nabla \phi|} = \mu \Delta G \tag{5.3}$$

the phase order parameter $\dot{\phi}$ is the time derivative of the free energy functional ϕ as defined by Kobayashi [229, 230]; it can be written in terms of the current phase order parameter ϕ, the thermodynamic description used within these equations is simplified.

$$\tau \dot{\phi} = \epsilon \nabla^2 \phi - \gamma \phi (1 - \phi)(\frac{1}{2} - \phi) + m \phi (1 - \phi) \tag{5.4}$$

Equation 5.4 can be rewritten in terms of physical material constants interfacial energy σ and interfacial width η [219] where; $\epsilon = \sigma \eta$, $\gamma = 72 \frac{\sigma}{\eta}$, $m = -6 \Delta G$ and $\tau = \frac{\eta}{\mu}$; combining these terms with Equation 5.4 produces:

$$\dot{\phi} = \mu \sigma \left[\nabla^2 \phi - \frac{36}{\eta^2} \phi (1 - \phi)(\frac{1}{2} - \phi) \right] + \mu \frac{6}{\eta} \phi (1 - \phi) \Delta G \tag{5.5}$$

The variational derivative of ϕ in Equation 5.5 can be written in terms of a curvature $\dot{\phi}_{curv}$ and thermodynamic $\dot{\phi}_{curv}$ contribution; each of these terms cause atoms to move between the interface;

$$\dot{\phi} = \dot{\phi}_{curv} + \dot{\phi}_{therm} \tag{5.6}$$

the separation of Equation 5.5 into separate thermodynamic and curvature terms (Equation 5.6) classifies the different terms in the equation as contributing the both individual aspects. The first term in Equation 5.4 is independent of thermodynamics ΔG and so is classed as being the curvature term:

$$\dot{\phi}_{curv} = \mu\sigma \left[\nabla^2\phi - \frac{36}{\eta^2}\phi(1-\phi)(\frac{1}{2}-\phi) \right] \tag{5.7}$$

the second term that is influenced by thermodynamics is classed as the thermodynamic term:

$$\dot{\phi}_{therm} = \mu\frac{6}{\eta}\phi(1-\phi)\Delta G \tag{5.8}$$

For steady state or a stationary profile, using the double well, potential can show that:

$$|\nabla\phi| = \frac{6}{\eta}\phi(1-\phi) \tag{5.9}$$

a similar expression can be used for the second derivative of the phase order parameter to be

$$|\nabla^2\phi| = \frac{36}{\eta^2}\phi(1-\phi)\left(\frac{1}{2}-\phi\right) \tag{5.10}$$

substituting Equation 5.9 into Equation 5.8 gives:

$$\dot{\phi}_{therm} = \mu|\nabla\phi|\Delta G \tag{5.11}$$

from Equation 5.3; $\mu\Delta G$ is the interfacial velocity; this converts Equation 5.11 into:

$$\dot{\phi}_{therm} = |\nabla\phi|v_{therm} \tag{5.12}$$

using Equation 5.1 the velocity term within Equation 5.12 can be written in terms of interfacial diffusion fluxes; these fluxes may be written in the chemical potential difference across the interface Equation 5.2:

$$\dot{\phi}_{therm} = |\nabla\phi|(-V_m)\sum_i \frac{-M_i x_i}{V_m}\frac{\Delta G_{therm,i}}{\Delta z} \tag{5.13}$$

Assuming that the interfacial mobility M_{int} for the elements is the same; and that each element has the same molar volume, additionally that $\Delta G_{therm,i} = \Delta\mu_i^{\alpha\beta}$ Equation 5.13 can be simplified:

$$\dot{\phi}_{therm} = |\nabla\phi|\frac{M_{int}}{\Delta z}\sum_i x_i \Delta\mu_i^{\alpha\beta} \tag{5.14}$$

Equation 5.3 allows $\dot{\phi}$ to be written in terms of a thermodynamic driving force; this allows Equation 5.14 to be written in terms of ΔG_{therm}:

$$\Delta G_{therm} = \frac{1}{\mu}\frac{M_{int}}{\Delta z}\sum_i x_i \Delta\mu_i^{\alpha\beta} \tag{5.15}$$

Chemical potentials are defined as the intersect of the tangent to the Gibbs energy curve [182];

$$\Delta G^{\alpha} = \sum x_i^{\alpha}\Delta\mu_i^{\alpha} \tag{5.16}$$

therefore Equation 5.16 can be used with Equation 5.15 to determine the value of the interfacial mobility assuming that $\Delta G^{\alpha} = \Delta G_{therm}$:

$$\mu = \frac{-M_{int}}{\Delta z} \tag{5.17}$$

The curvature contribution to the phase field model Equation 5.7 can be written as a function of ΔG_{curv} through the relation in Equation 5.3

$$\dot{\phi}_{curv} = \mu\sigma\left[\nabla^2\phi - \frac{36}{\eta^2}\phi(1-\phi)(\frac{1}{2}-\phi)\right] = \mu|\nabla\phi|\Delta G_{curv} \tag{5.18}$$

the interfacial mobility μ in Equation 5.18 cancels out and can be rearranged in terms of ΔG_{curv};

$$\Delta G_{curv} = \sigma \frac{\nabla^2 \phi - \frac{36}{\eta^2}\phi(1-\phi)(\frac{1}{2}-\phi)}{|\nabla \phi|} = \frac{\dot{\phi}_{curv}}{\mu |\nabla \phi|} \tag{5.19}$$

Equation 5.19 is undefined in the bulk regions, at the condition where ϕ is either 1 or 0; this is something which will be addressed later in the derivation. From Equation 5.3 allows $\dot{\phi}_{curv}$ to be expressed in terms of the interface velocity and from Equation 5.1 in terms of interface fluxes;

$$\dot{\phi}_{curv} = -|\nabla \phi| V_m \sum j_i^{\alpha\beta} \tag{5.20}$$

the interfacial velocity occurring from curvature, v_{curv}, in Equation 5.20 can subsequently be written in terms of chemical potential using Equation 5.2 and using $\Delta \mu^{\alpha\beta}$ as ΔG_{curv};

$$\dot{\phi}_{curv} = -|\nabla \phi| V_m \Delta G_{curv} \sum -\frac{M_i x_i}{\Delta z} \tag{5.21}$$

substituting ΔG_{curv} from Equation 5.19 into Equation 5.21

$$\dot{\phi}_{curv} = |\nabla \phi| \left(\sigma \frac{\nabla^2 \phi - \frac{36}{\eta^2}\phi(1-\phi)(\frac{1}{2}-\phi)}{|\nabla \phi|} \right) (-V_m) \sum \frac{M_i x_i}{\Delta z} \tag{5.22}$$

Now Equation 5.22 simplifies such that the $|\nabla \phi|$ cancels out simplifying the equation to;

$$\dot{\phi}_{curv} = \left(\sigma \nabla^2 \phi - \frac{36}{\eta^2}\phi(1-\phi)(\frac{1}{2}-\phi) \right) (-V_m) \sum \frac{M_i x_i}{\Delta z} \tag{5.23}$$

Substituting Equation 5.23 and Equation 5.14 into Equation 5.6 as well as substituting the velocity using Equation 5.1

$$\dot{\phi} = \left(\sigma\nabla^2\phi - \frac{36}{\eta^2}\phi(1-\phi)(\frac{1}{2}-\phi)\right)(-V_m)\sum\frac{M_i x_i}{\Delta z} + |\nabla\phi|\frac{M_{int}}{\Delta z}\sum_i x_i\Delta\mu_i^{\alpha\beta} \tag{5.24}$$

Equation 5.24 describes the Equation 5.5 with mobilities, M, molar fractions, x, chemical potentials, μ and the phase variable ϕ. The equation is defined such that it is defined within the interface and bulk regions.

The driving force across the interface for both the curvature and thermodynamic contributions can be substituted into Equation 5.2 as $\Delta\mu_i^{\alpha\beta}$;

$$j_i^{\alpha\beta} = -\frac{x_i M_i}{V_m}\frac{\Delta G_{curv} + \Delta G_{therm,i}}{\Delta z} \tag{5.25}$$

Equation 5.25 defines the flux across the interface from the curvature and thermodynamic contributions separately. Considering only the $\Delta G_{therm,i}$ term in Equation 5.25 provides the same equation as that in Equation 5.2; therefore

$$\Delta G_{therm,i} = \Delta\mu_i^{\alpha\beta} \tag{5.26}$$

5.2.1 Mutli Phase Field

The multi-phase field method allows the interaction of multiple phases at the same point; this modifies several equations to consider the different interactions. These are Equation 5.19 function and Equation 5.9; these become

$$\Delta G_{curv} = \sigma_{ij}\left[\phi_j\nabla\phi_i - \phi_i\nabla\phi_j - \frac{36}{\eta^2}(\phi_i - \phi_i)\phi_i\phi_j\right] \tag{5.27}$$

$$\nabla\phi_{ij} = \frac{6}{\eta}\phi_i\phi_j \tag{5.28}$$

Equation 5.27 and Equation 5.28 are actually the more complex versions of Equation 5.19

and Equation 5.9 respectively; the derivation showing the equivalence of the two phases in a binary case is shown in Appendix A.

The interface reaction not determined (metal-oxygen) is ignored from calculating as σ is set to 0 in these cases.

5.2.2 Metal-Oxide Interface

To describe the metal-oxide interface, the driving force for the interface between the metal and oxide ΔG_{therm};

$$\Delta G_{therm} = \Delta G_{products} - \Delta G_{reactants} \tag{5.29}$$

can be re-written in terms of chemical potentials; where the assumption made is that the new oxide forming is as if there was no original oxide present; this, therefore, creates the reaction

$$Ni^{fcc} + VaO^{Ox} \leftrightharpoons NiO^{Ox} + Va^{fcc} \tag{5.30}$$

The compound VaO is the compound that would form if the metal sublattice of the oxide was vacant of any metal ions, whereas the oxygen sublattice is full of oxygen ions. The interfacial reactions thermodynamics thus become

$$\Delta G_{therm} = \mu^{ox}_{Ni:O} - \mu^{fcc}_{Ni} - \mu^{Ox}_{Va:O} \tag{5.31}$$

The vacancy concentration within the *fcc* phase is assumed to be within equilibrium conditions as they are assumed to diffuse rapidly towards vacancy sinks within the material; therefore, the chemical potential of vacancies within the metal is ignored as it is a constant at sufficiently low concentrations to not be of concern.

The fluxes of the elements are appropriately distributed as ΔG_{therm} is the total number

of moles that move across the interface, assuming that all elements are mobile. Therefore the calculated flux of nickel is half of that calculated due to stoichiometry of nickel oxide.

5.2.3 Oxide-Gas Interface

The following flux for oxygen ingress is used and is discussed in Chapter 4; Equation 4.30) incorporates oxygen into the oxide in a phase-field consistent manner;

$$j_O = \frac{k_c M}{N_A} \tag{5.32}$$

Equation 5.32 adds oxygen only at the oxide-gas interface; therefore, it needs to be adjusted to only apply during the interface region; this is done through the use of $|\nabla\phi|$ to ensure the correct flux units this is multiplied by the distance the oxygen flux is travelling over, Δz;

$$j_O = \frac{k_c M}{N_A}|\nabla\phi|\Delta z \tag{5.33}$$

The oxygen flux in Equation 5.33 needs to be adjusted to only add oxygen to the system when the concentration of vacancies gets sufficiently low that the oxide surface is composed of metal oxide. This adjustment is made by the term $\exp(-y_{f_{Va}} + \sum y_{f_i})$; as

$$j_O = \frac{k_c M}{N_A}|\nabla\phi|\Delta z \exp(-y_{f_{Va}} + \sum y_{f_i}) \tag{5.34}$$

The sum of all the components on the sublattice is equal to 1;

$$1 = y_{f_{Va}} + \sum y_{f_i} \tag{5.35}$$

rearranging Equation 5.35 and defining $\sum y_{f_i}$ as $y_{f_{Me}}$ in terms of the vacancy site fractions;

$$y_{f_{Va}} = 1 - y_{f_{Me}} \tag{5.36}$$

Substituting Equation 5.36 into Equation 5.34 adjusts the flux of oxygen to not be dependent on the site fraction of vacancies;

$$j_O = \frac{k_c M}{N_A} |\nabla \phi| \Delta z \exp(-(1 - y_{f_{Me}}) + y_{f_{Me}}) \tag{5.37}$$

Equation 5.37 can be simplified to

$$j_O = -\frac{k_c M}{N_A} |\nabla \phi| \Delta z \exp(1 - 2y_{f_{Me}}) \tag{5.38}$$

Looking at the reverse reaction where oxygen disassociates from the oxide, the same assumption for the rate of oxygen ingress is used however reversed;

$$j_O = \frac{k_c M}{N_A} |\nabla \phi| \Delta z \exp(1 - 2y_{f_{Me}}) \tag{5.39}$$

Combining both the positive Equation 5.38 and negative Equation 5.39 fluxes results in the total overall flux being;

$$j_O = -\frac{k_c M}{N_A} |\nabla \phi| \Delta z \left(\exp\left(1 - 2y_{f_{Me}}\right) - \exp\left(1 - 2y_{f_{Me}}\right)\right) \tag{5.40}$$

further simplification for combining the exponential terms in Equation 5.40 into sinh resulting in the oxygen diffusion being;

$$j_O = -\frac{k_c M}{2N_A} |\nabla \phi| \Delta z \sinh\left(1 - 2y_{f_{Me}}\right) \tag{5.41}$$

If the system being modelled has a single element on the metal sublattice, then $y_{f_{Me}}$ is the site fraction of the element, whereas if the model simulates multiple elements, then $y_{f_{Me}}$ is expressed as $\sum y_{f_i}$.

$$j_O = -\frac{k_c M}{2N_A} |\nabla \phi| \Delta z \sinh\left(1 - 2y_{f_{Me}}\right) \tag{5.42}$$

Equation 5.25 assumes that the thermodynamic diffusion occurs via a chemical potential driven mechanism which is not the case at the oxide-gas interface; therefore, $\Delta G_{therm} = 0$ and Equation 5.41 is added to compute the addition of oxygen into the oxide;

$$j_O = -\frac{x_O M_{Me}}{V_m}\frac{\Delta G_{curv}}{\Delta z} - \frac{k_c M}{N_A}|\nabla\phi|\Delta z \sinh(1 - 2y_{f_{Me}}) \tag{5.43}$$

as oxygen's mobility within the oxide is not known, the mobility of the metal is used to determine the flux of oxygen across the interface for the curvature term.

5.2.4 Computation

The movement of mass for these phase-field simulations is calculated by Equation 5.25 and the respective bulk flux equations Equation 4.9 and Equation 4.23 are used in the *fcc* and halite phases respectively. Once the fluxes have been determined, the fluxes are changed into a change in moles

$$\Delta n_i = j_i A t \tag{5.44}$$

where the area that the atoms flow through is defined as;

$$A = \int |\nabla\phi| dV = |\nabla\phi| \int dV = \frac{6}{\eta}\phi(1-\phi)V \tag{5.45}$$

5.2.5 Parameters and Simulation Numerics

Simulations used a 1nm grid spacing. The simulation domain for a 1-dimensional simulation was comprised of 40 regions; 2-dimensional simulations were made up of 160 volumes in a 40x40 grid. Zero flux boundary conditions were used. The phase field parameters η and σ were used as 3nm and 100 $\frac{mJ}{m^2}$ respectively. Simulations where these parameters varied were with values of $2 - 5$nm and 1, 10 and 100 $\frac{mJ}{m^2}$. The simulation used a time step of 1×10^{-6}s and was used to simulate 1s and 10s. The molar volume in all three

phases was assumed to be constant for simplicity, and the value used was 1×10^{-5}. The temperature was 1100K, and the pressure was 1×10^{5}Pa. The value of k_c used was 100s^{-1} and the value of M^I used was 1×10^{-5}.

The thermodynamic database used for the simulations was by Taylor [258], the diffusivity data for the oxide phase was taken from [259, 261] as Q being 225kJmol^{-1} and D_O being 1.7×10^{-6}m^{2}s^{-1}and the diffusivity data in the *fcc* phase was from [262], as Q being 287kJmol^{-1} and D_0 being 9.2×10^{-5}m^{2}s^{-1}. There was assumed to be no diffusivity of oxygen within the system domain.

The *fcc* phase comprised 0.857143 moles of nickel in the *fcc* phase and 1×10^{-20} moles of oxygen in the *fcc* phase, and 1×10^{-20} moles of nickel and oxygen in the oxide and gas phase. The halite phase comprised 0.52 moles of oxygen and 0.48 moles of nickel, and 1×10^{-20} moles of nickel and oxygen in the *fcc* and gas phases. The gas phase comprised of 0.857143 moles of oxygen and 1×10^{-20} moles of nickel, and 1×10^{-20} moles of nickel and oxygen in the *fcc* and oxide phase.

Thick oxide films comprised 4 grid points of oxide transitioning linearly into the *fcc* and gas phases over 3 grid points. A linear fraction of the moles was used to define the transition and avoid a sharp interface. Thin oxide films were comprised of a single fully oxide grid point. Simulating the triple point of the different phases was undertaken where the largest fraction of oxide was at 50%.

5.3 Results

Simulations were run to show the ability of the developed model to simulate the growth of nickel oxide from an initial oxide coating. A thin and thick layer was started initially, and there were no interactions between the *fcc* and gas phases during the start of the simulation. Figure 5.1 shows how the oxide grows on a thin interface between the oxide and gas phase. As the simulation steps proceed, there is a large growth of initial oxide at the gas-oxide interface; this can be seen from the peak in oxygen molar fraction in the oxide. As the oxide grows, the interface between the oxide-gas phase and the interface

profile at the oxide side of the interface becomes flat and sharp (c.f. Figure 5.2 ϕ at 10s), which reduces the phase-field model's ability for the interface to move. The same effect is present when the initial layer of oxide is thick. Figure 5.2 exhibits the same behaviour as Figure 5.1 where the initial growth causes a large amount of oxide to move into the oxide. The peak is smaller and more spread out across the oxide as there is a greater ability for nickel to diffuse within the oxide. In Figure 5.1 and Figure 5.2 at 1s of the simulation, there is a mixture of oxide and gas at the oxide-metal interface, as the interface reaction transforms a small amount of gas becomes trapped within the oxide and is seen by a slight spike just next to the oxide interface in Figure 5.1 and Figure 5.2.

To investigate the effect of changing the interfacial width η from $2 - 5$; to see what influence η has on the oxide-gas phase interface forming a sharp interface into the oxide seen in Figure 5.1 and Figure 5.2. Figure 5.5 and Figure 5.3 shows thick and thin initial oxide films respectively; the curvature into the gas phase works as intended producing a sigmoidal profile. Further investigation into the molar fraction for a thin initial oxide; Figure 5.4 shows an increase in the oxygen concentration within the oxide that drives the model away from an equilibrium state. As η is increased, oxygen's peak is increased; however, this is related to the reduced fluxes of oxygen and is paired with the greater spread of the interfaces over a wider range. The oxygen concentration in the gas phase in the interface region is greater as η is increased; this is evidence of the reduced oxygen flux across the interface. For an initial thick oxide shown in Figure 5.6, the higher values of η transform slower again and result in a greater difference in nickel and oxygen molar fractions at the oxide-gas interface. The oxygen diffusion into the gas side of the oxide-gas interface is not seen in either initial oxides.

Changing the oxide-gas interfacial energy (σ) whilst maintaining a constant η value has been conducted for both initially thin and thick oxides and shown in Figure 5.7 and Figure 5.8 respectively. As σ increases, the reaction rate increases; therefore, the comparison has been normalised over the same numerical time steps. As the simulations are allowed to proceed, the resulting ϕ profiles in Figure 5.7 and Figure 5.8 after 1s for initial thin and thick respectively oxides are similar, showing the same behaviour at the oxide-gas

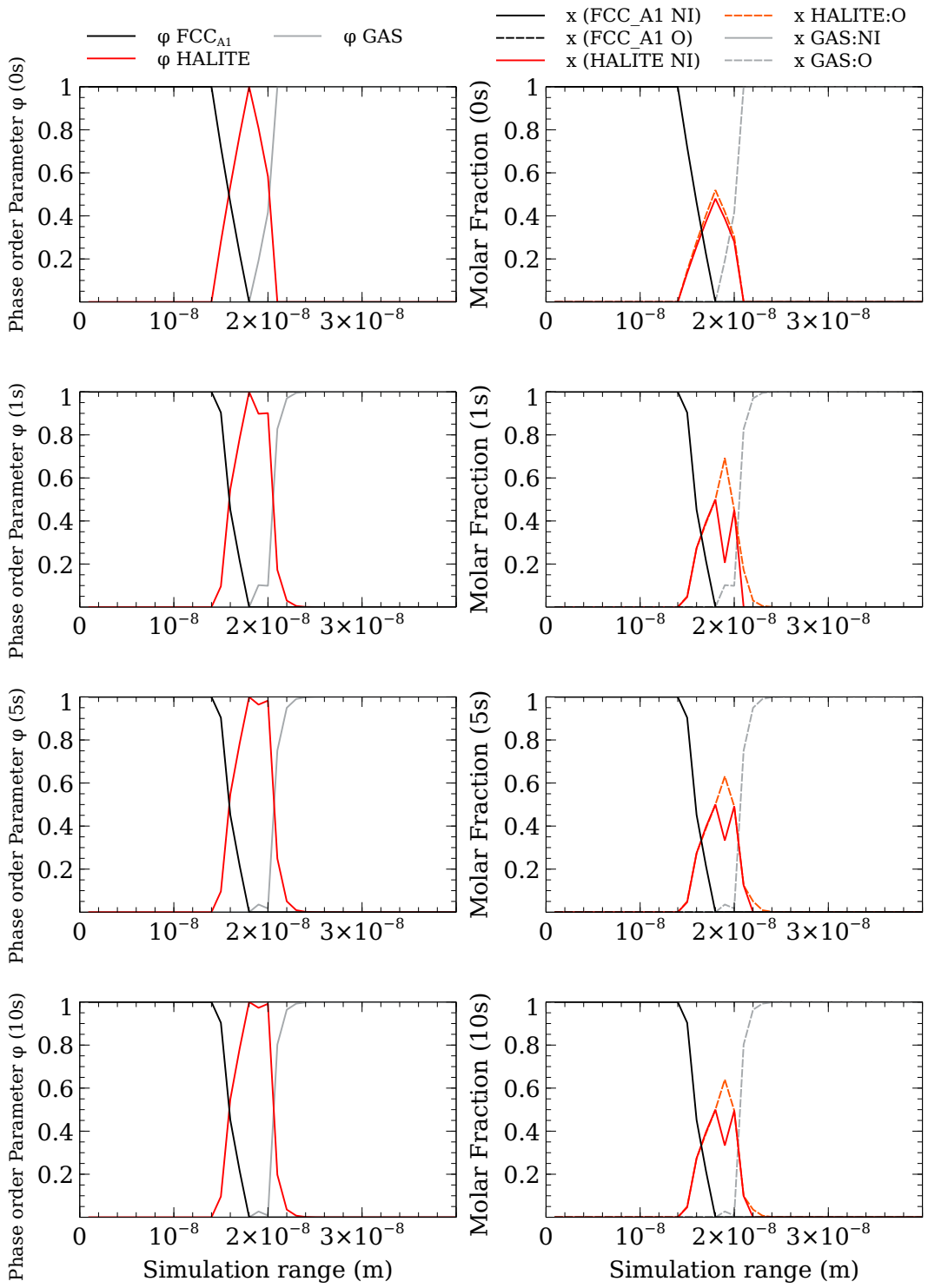

Figure 5.1: Plots showing the phase order parameter and molar fractions at four different times 0s, 1s, 5s and 10s for a thin initial oxide. The simulation domain for the phase order parameter is made up of *fcc* (black), oxide (red) and gas (grey), and the molar fractions are made up of The simulation domain from left to right is made up of *fcc* (black), oxide (red) and gas (grey). The oxygen molar fraction (orange) increases within the oxide as the simulation begins as oxygen from the oxide overlapping with the oxide is transformed into the oxide. As the simulation proceeds, this decreases. A small amount of gas is left within the oxide (a small grey peak at 10s), and the oxide side of the oxide-gas interface remains step-like.

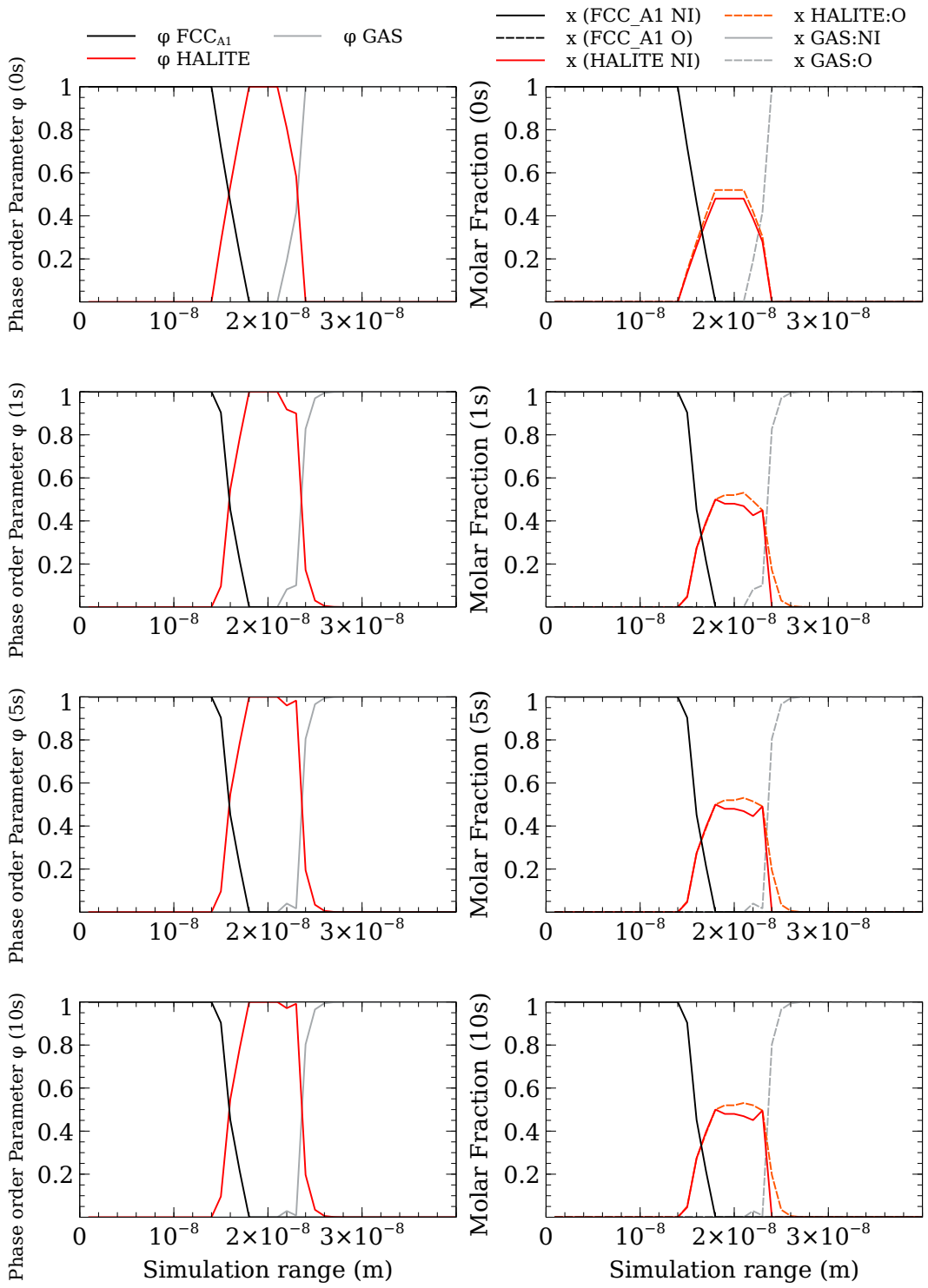

Figure 5.2: Plots showing the phase order parameter and molar fractions at four different times 0s, 1s, 5s and 10s for a thick initial oxide. The simulation domain for the phase order parameter is made up of *fcc* (black), oxide (red) and gas (grey), and the molar fractions are made up of The simulation domain from left to right is made up of *fcc* (black), oxide (red) and gas (grey). The oxygen molar fraction (orange) increases slightly within the oxide phase as the simulation proceeds, and a small volume of gas becomes trapped in the oxide (small grey peak at 10s) as the interface becomes a step at the oxide side of the interface.

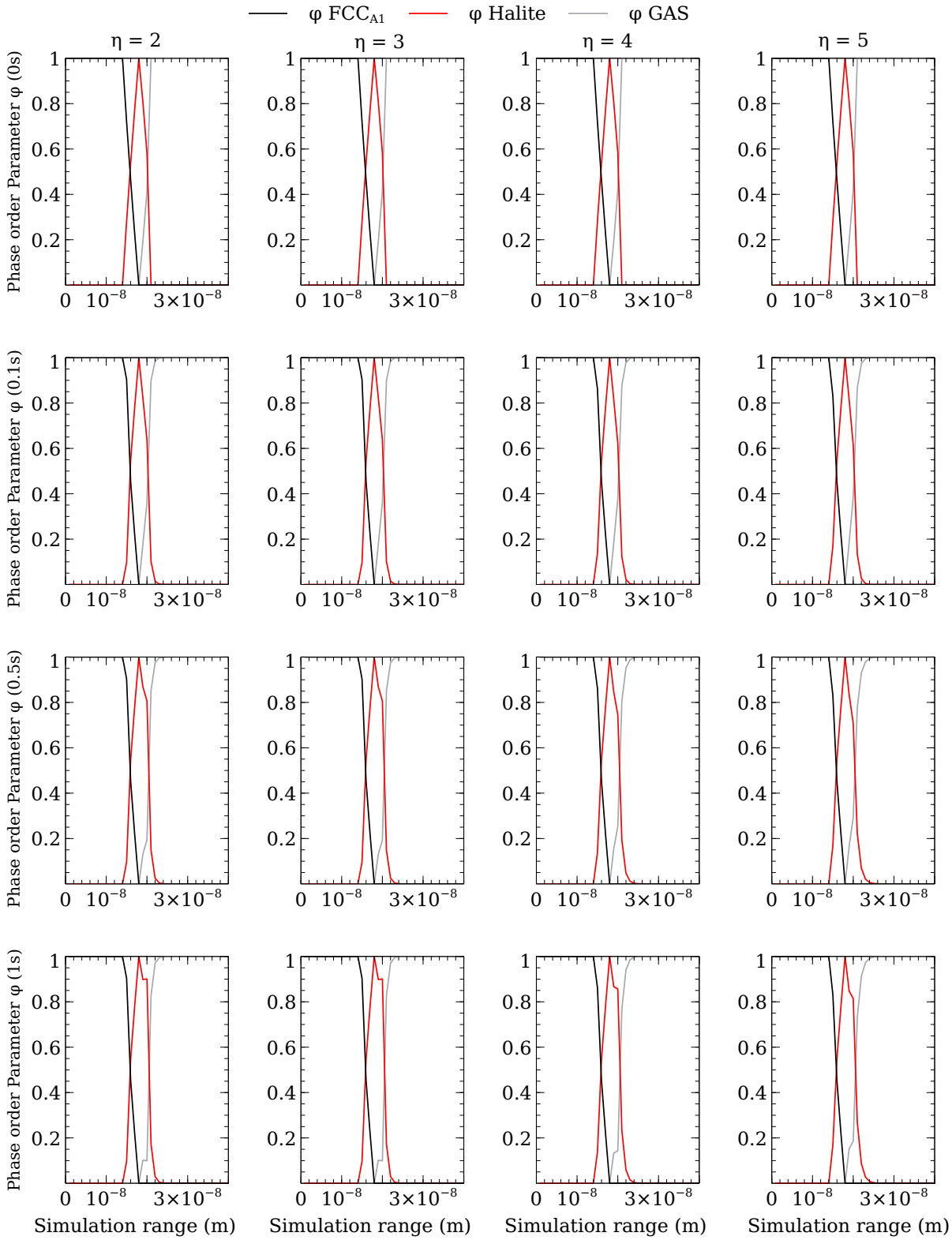

Figure 5.3: Plots showing four different η values from left to right $2-5$ at four different times 0s, 0.1s, 0.5s and 1s for a thin initial oxide. The simulation domain from left to right is made up of *fcc* (black), oxide (red) and gas (grey). As the time increases, a step begins to form and grow at the oxide-gas interface; this step is more pronounced for lower values of η but is present within all simulations.

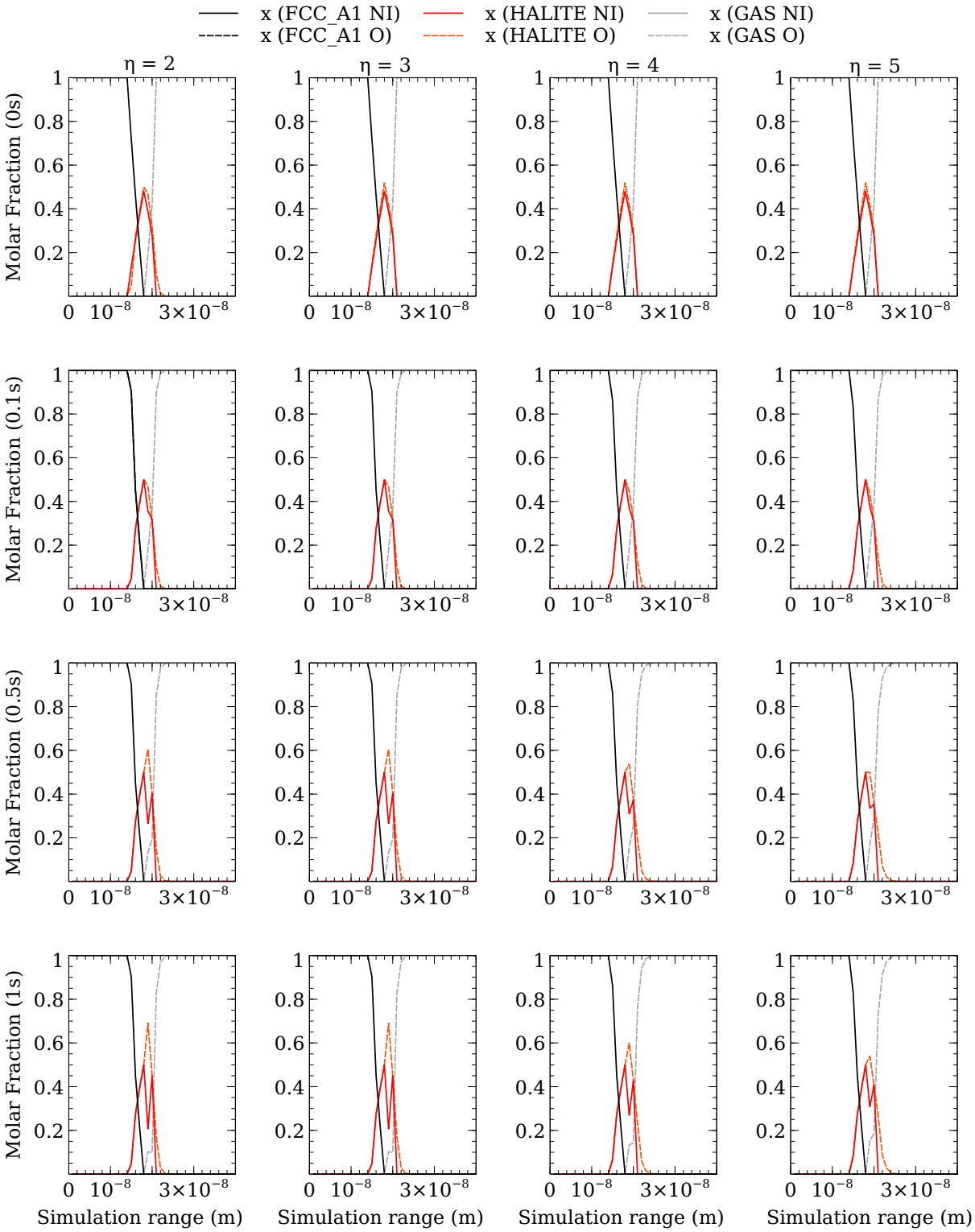

Figure 5.4: Plots showing four different η values from left to right $2-5$ at four different times 0s, 0.1s, 0.5s and 1s for a thin initial oxide. The simulation domain from left to right is made up of *fcc* Ni (black), *fcc* O (black dashed), oxide Ni (red), oxide O (orange dashed), gas Ni (grey) and gas O (grey dashed). The oxygen concentration in the oxide increases, decreasing the nickel fraction. At higher η values, the rate of oxygen increase is decreased, resulting in a greater step in the oxygen gas content.

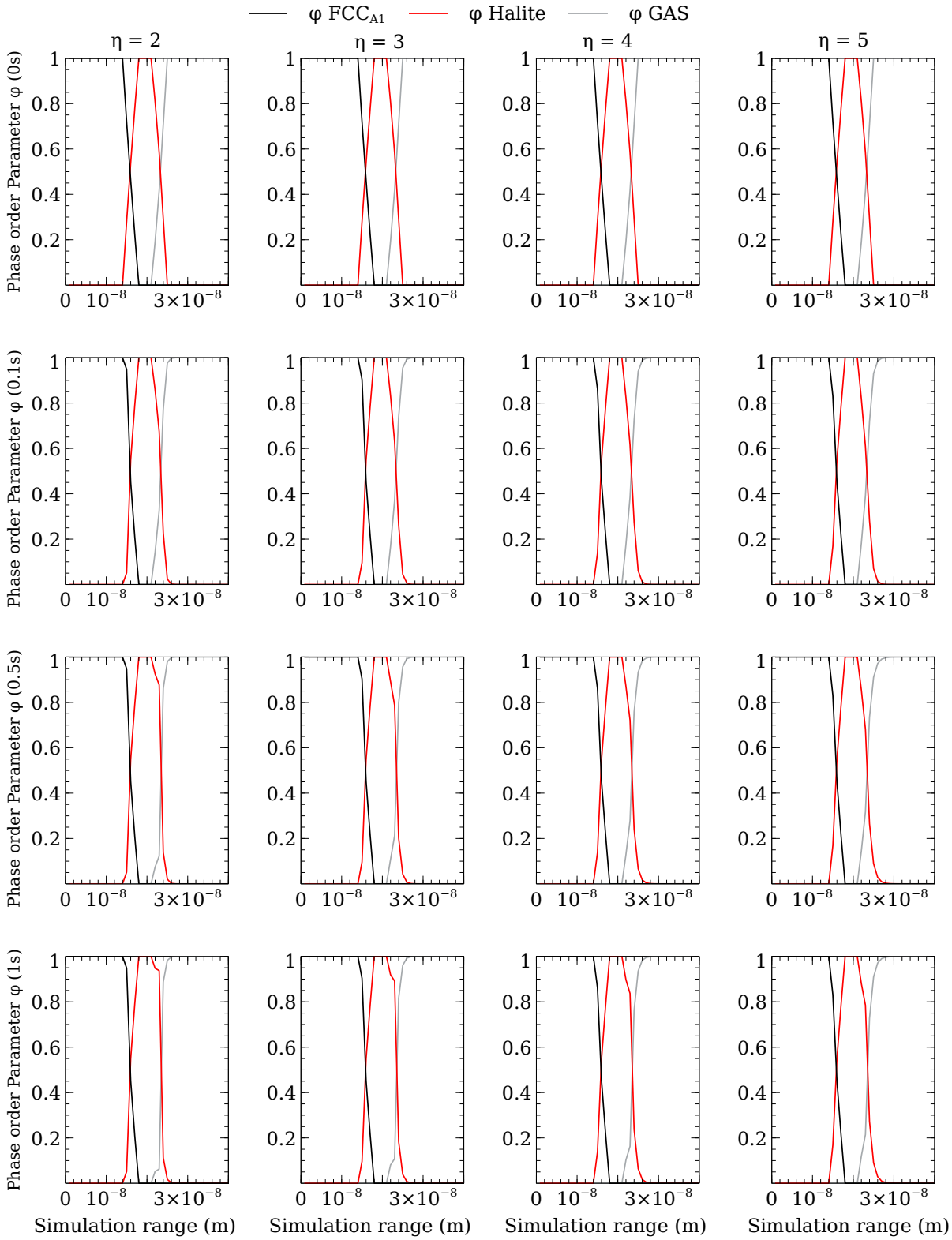

Figure 5.5: Plots showing four different η values from left to right $2-5$ at four different times 0s, 0.1s, 0.5s and 1s for a thick initial oxide. The simulation domain from left to right is made up of *fcc* (black), oxide (red) and gas (grey). As η increases, the formation of a step in the oxide interface at the oxide-gas interface becomes less pronounced.

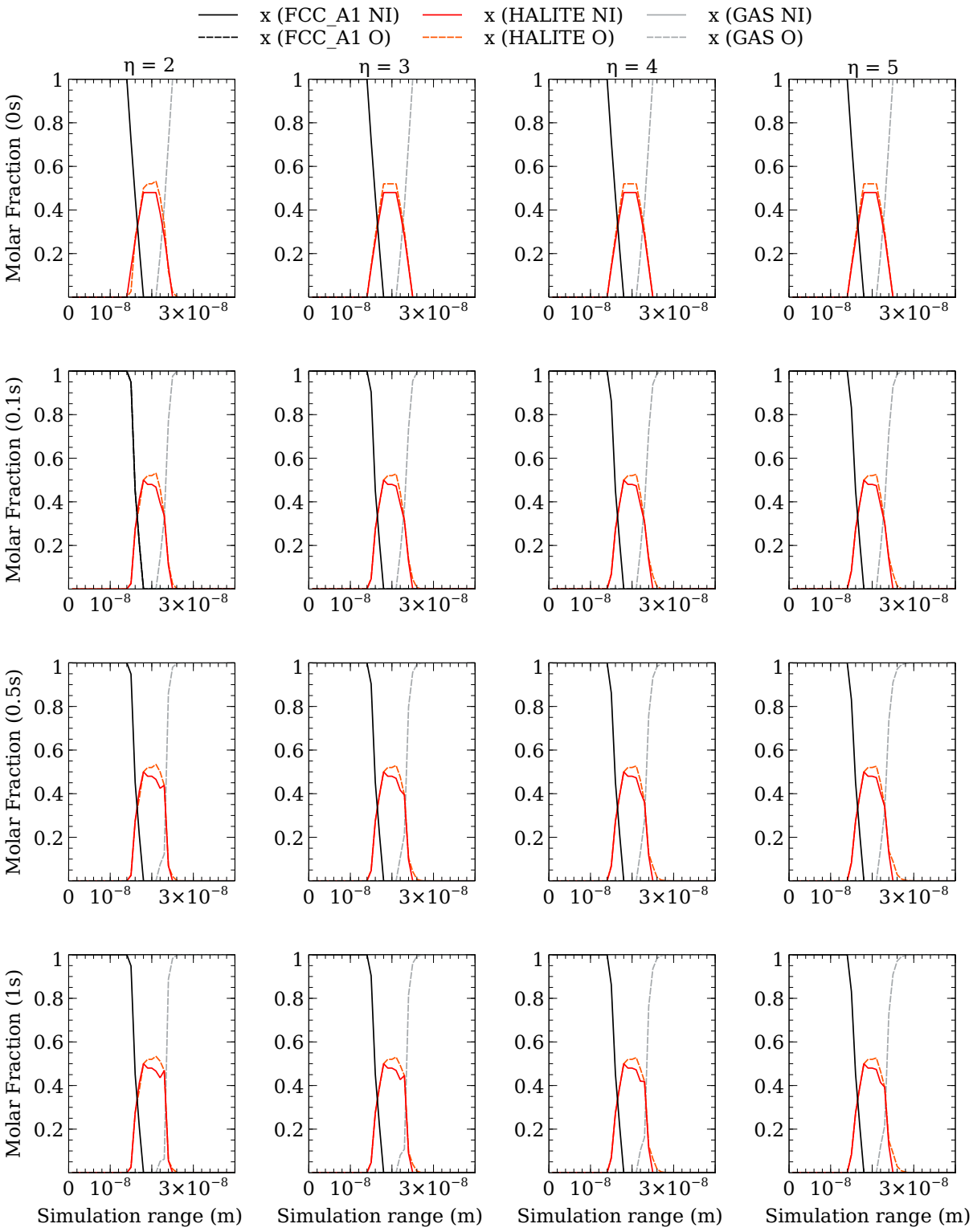

Figure 5.6: Plots showing four different η values from left to right $2-5$ at four different times 0s, 0.1s, 0.5s and 1s for a thick initial oxide. The simulation domain from left to right is made up of *fcc* Ni (black), *fcc* O (black dashed), oxide Ni (red), oxide O (orange dashed), gas Ni (grey) and gas O (grey dashed). As η is increased, the oxygen addition into the oxide decreases, resulting in a smaller difference within the oxides concentrations. As the oxide-gas interface transforms at lower values of η, there is a step of gaseous oxygen still present. At higher values of η, the simulation has not transformed sufficiently for this to be seen.

interface. A step is present at this interface where oxygen in the gas phase is concentrated within the oxide. σ variations do not influence the issue with the simulation stability.

The phase-field model developed within this work is done in a manner consistent with a multi-phase-field model. Basing this work on a multi-phase-field model allows for the possibility of an initially thin oxide being present on the surface of the metal, and the model can simulate the growth of the initial oxide seed. A simulation for a 1D example of this triple point simulation has been run in Figure 5.9. As the simulation runs, the oxide formed has a composition that is made up of 50% nickel and oxygen. There is an increase in the nickel oxide concentration in the bulk metal; there is no increase in oxygen to accommodate this nickel increase. The oxide's region is reduced as the simulation produces the ideal curvature state from the initial conditions.

Simplified simulations that only consider the oxide-gas interface have been conducted in situations where the interface initially is sharp (c.f. Figure 5.10) and also already in the form of a sigmoidal profile (c.f. Figure 5.11). These simulations show the oxide interface side forming the sharp interface rather than maintaining the rounded and curved sigmoidal shape. In front of the interface, the oxygen concentration is increased; the oxygen increase in the oxide is more significant during the initial sigmoidal profile than during the sharper interface.

Figure 5.12 shows simulation results for the 2D version of the phase-field model, highlights issues with the interactions of the different phases in multiple directions, and the resulting *fcc* -oxide interface becomes full of metal whilst there is no oxygen, almost forming a metallic phase. The oxygen within the oxide shows signs of variation within the oxide, regions of high oxygen concentration and other regions where the oxygen concentration is reduced.

5.4 Discussion

Simulations were run for thin and thick initial oxides and shown in Figure 5.1 and Figure 5.2 respectively; these figures show the simulations both show the interfaces between

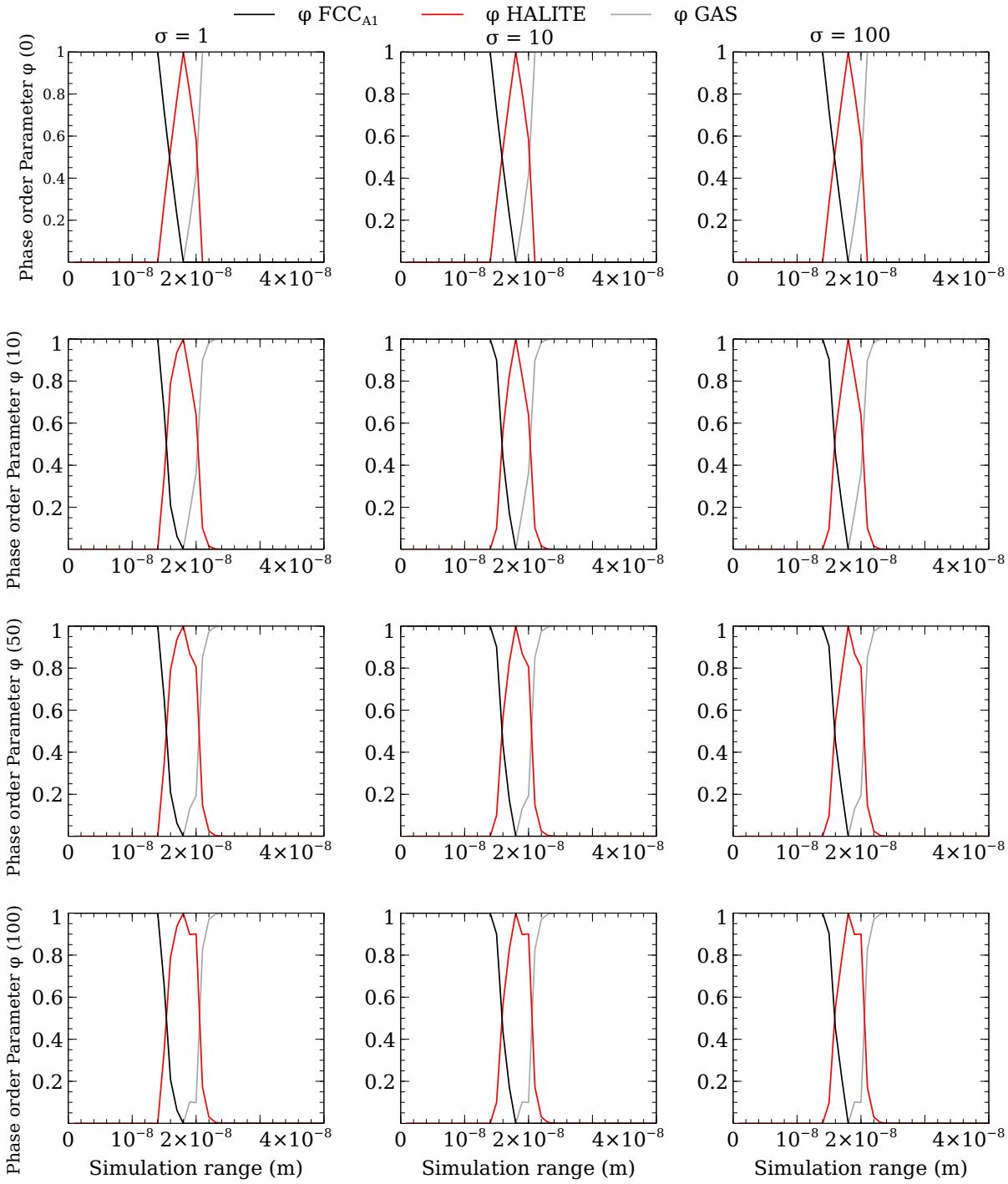

Figure 5.7: Plots showing three different σ values for the oxide-gas interface from left to right $1-100$ at four different times 0s, 0.1s, 0.5s and 1s for a thin initial oxide. The simulation domain from left to right is made up of *fcc* (black), oxide (red) and gas (grey). Simulations were scaled for the number of time steps as the interface reaction rate varies based on the σ value. As the simulations proceed, the oxide-gas interface forms a step as the gas is retained within the oxide. The *fcc* -oxide interface transforms faster at a σ value of 1 as the time step increases to ensure good comparison.

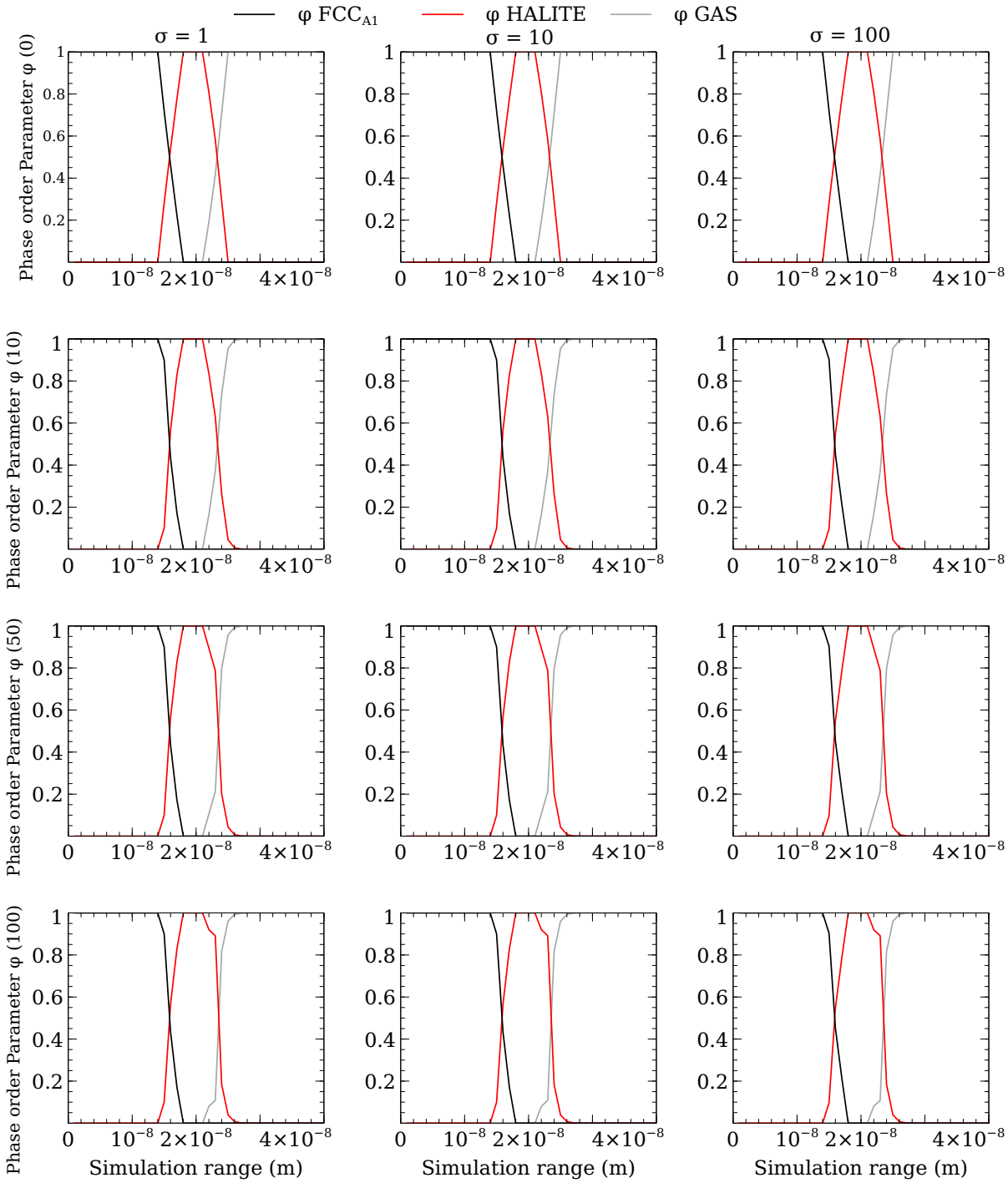

Figure 5.8: Plots showing three different σ values for the oxide-gas interface from left to right $1-100$ at four different times 0s, 0.1s, 0.5s and 1s for a thick initial oxide. The simulation domain from left to right is made up of *fcc* (black), oxide (red) and gas (grey). Simulations were scaled for the number of time steps as the interface reaction rate varies based on the σ value. As the simulations proceed, the oxide-gas interface forms a step as the gas is retained within the oxide.

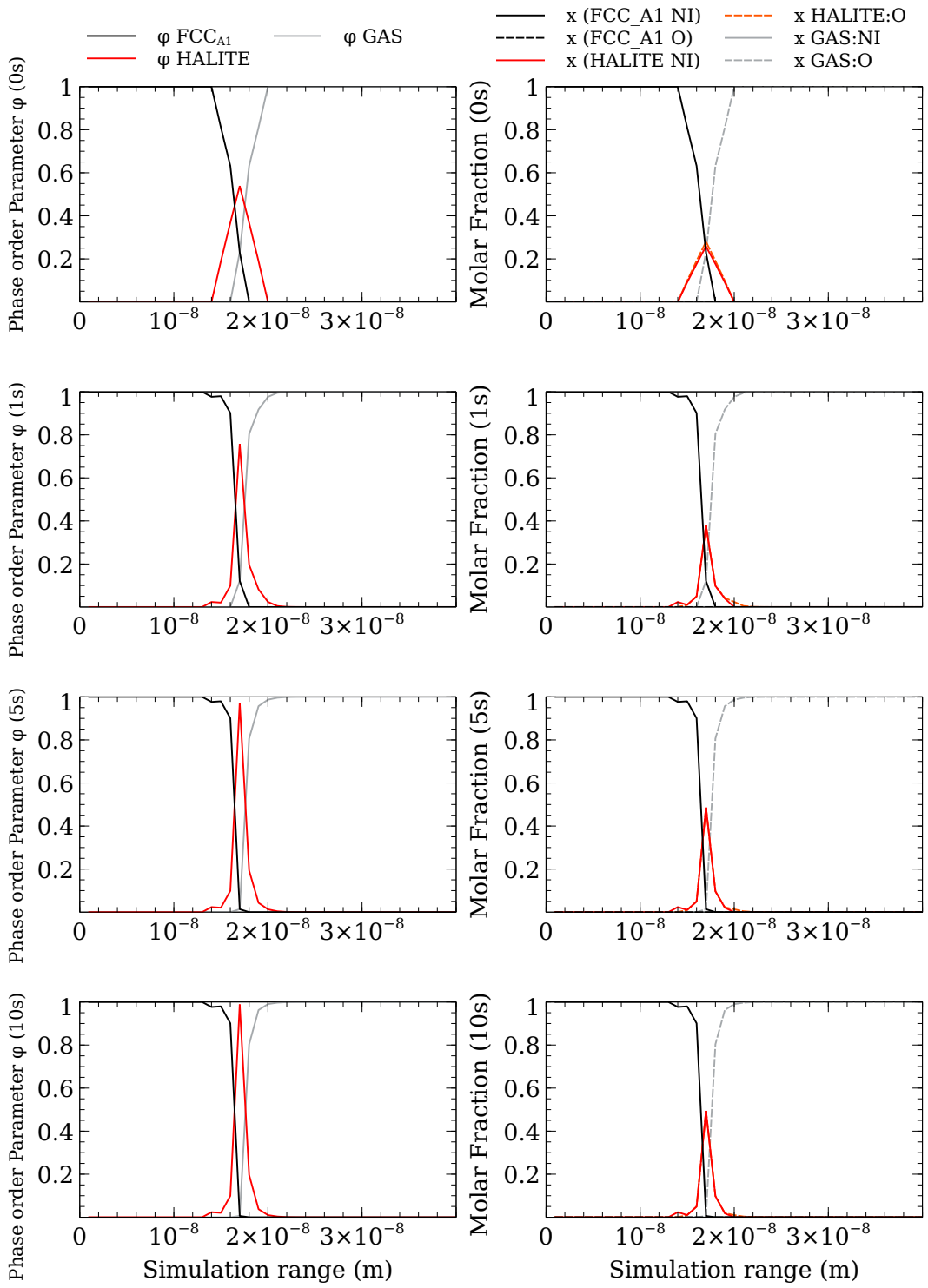

Figure 5.9: Plots showing the phase order parameter and molar fractions at four different times 0s, 1s, 5s and 10s for a thin initial oxide ensuring all three phases interact. The simulation domain for the phase order parameter is made up of *fcc* (black), oxide (red) and gas (grey), and the molar fractions are made up of The simulation domain from left to right is made up of *fcc* (black), oxide (red) and gas (grey). As the simulation proceeds, the oxide phase grows as the interface curvature occurs. There is a small region of oxide composed of nickel in the *fcc* phase; this is a result of the curvature terms influence at the *fcc* -oxide interface.

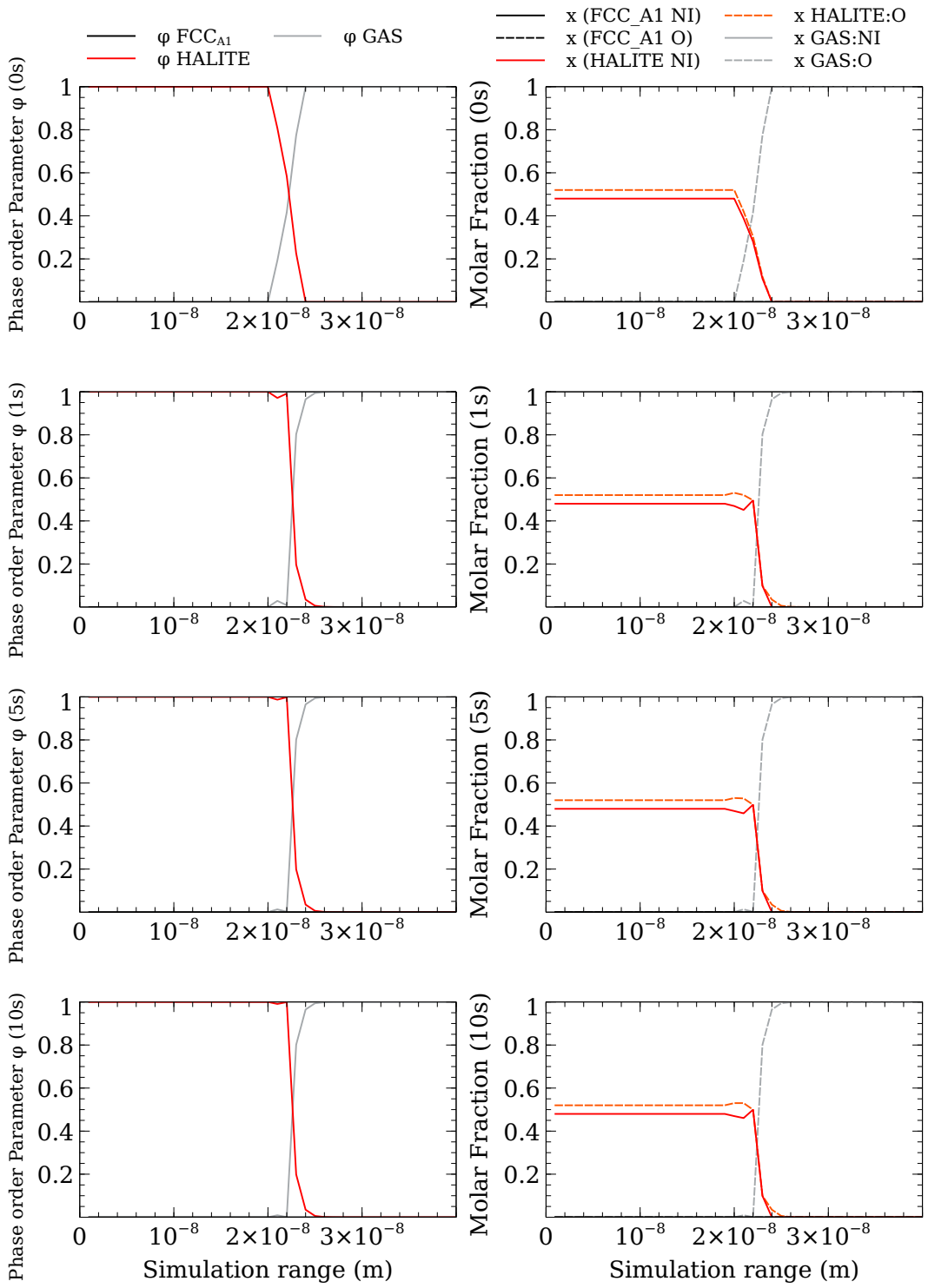

Figure 5.10: Plots showing the phase order parameter and molar fractions at four different times 0s, 1s, 5s and 10s for the interaction between the oxide and gas phases with a linear distribution between the two phases. The simulation domain for the phase order parameter is made up of *fcc* (black), oxide (red) and gas (grey), and the molar fractions are made up of The simulation domain from left to right is made up of *fcc* (black), oxide (red) and gas (grey). At the interface between the two phases, the oxygen fraction increases as the interface between the phases transform. A small amount of trapped gas within the oxide gradually dissipates as the simulation proceeds, but the resulting interface is sharp.

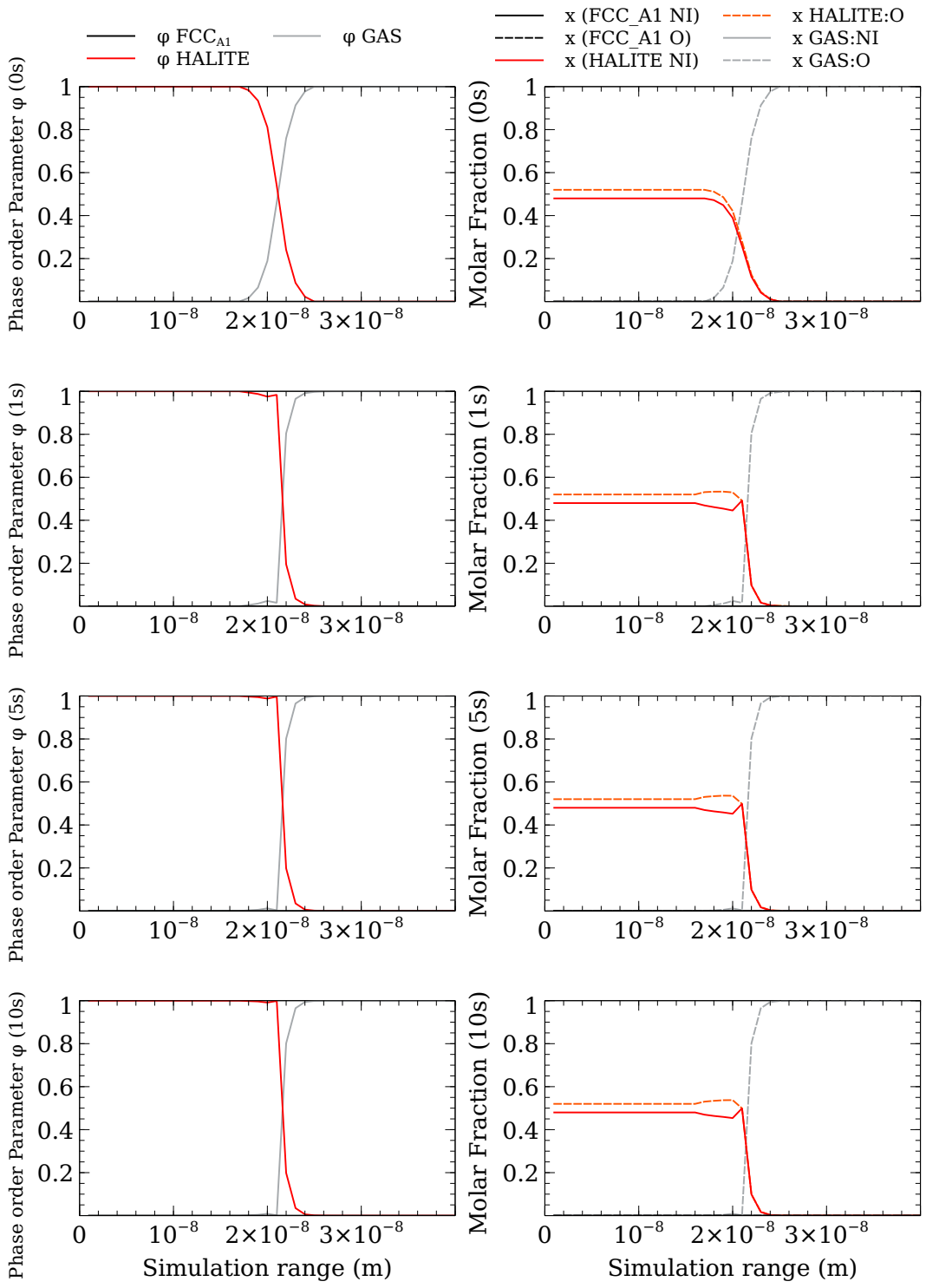

Figure 5.11: Plots showing the phase order parameter and molar fractions at four different times 0s, 1s, 5s and 10s for the interaction between the oxide and gas phases with a sigmoidal distribution between the two phases. The simulation domain for the phase order parameter is made up of *fcc* (black), oxide (red) and gas (grey), and the molar fractions are made up of The simulation domain from left to right is made up of *fcc* (black), oxide (red) and gas (grey). At the interface between the two phases, the oxygen fraction increases as the interface between the phases transform; there is a large increase in oxygen concentration in the oxide phase due to the more spread-out nature of the sigmoidal interface. A small fraction of gas becomes trapped in the oxide and dissipates as the simulation proceeds.

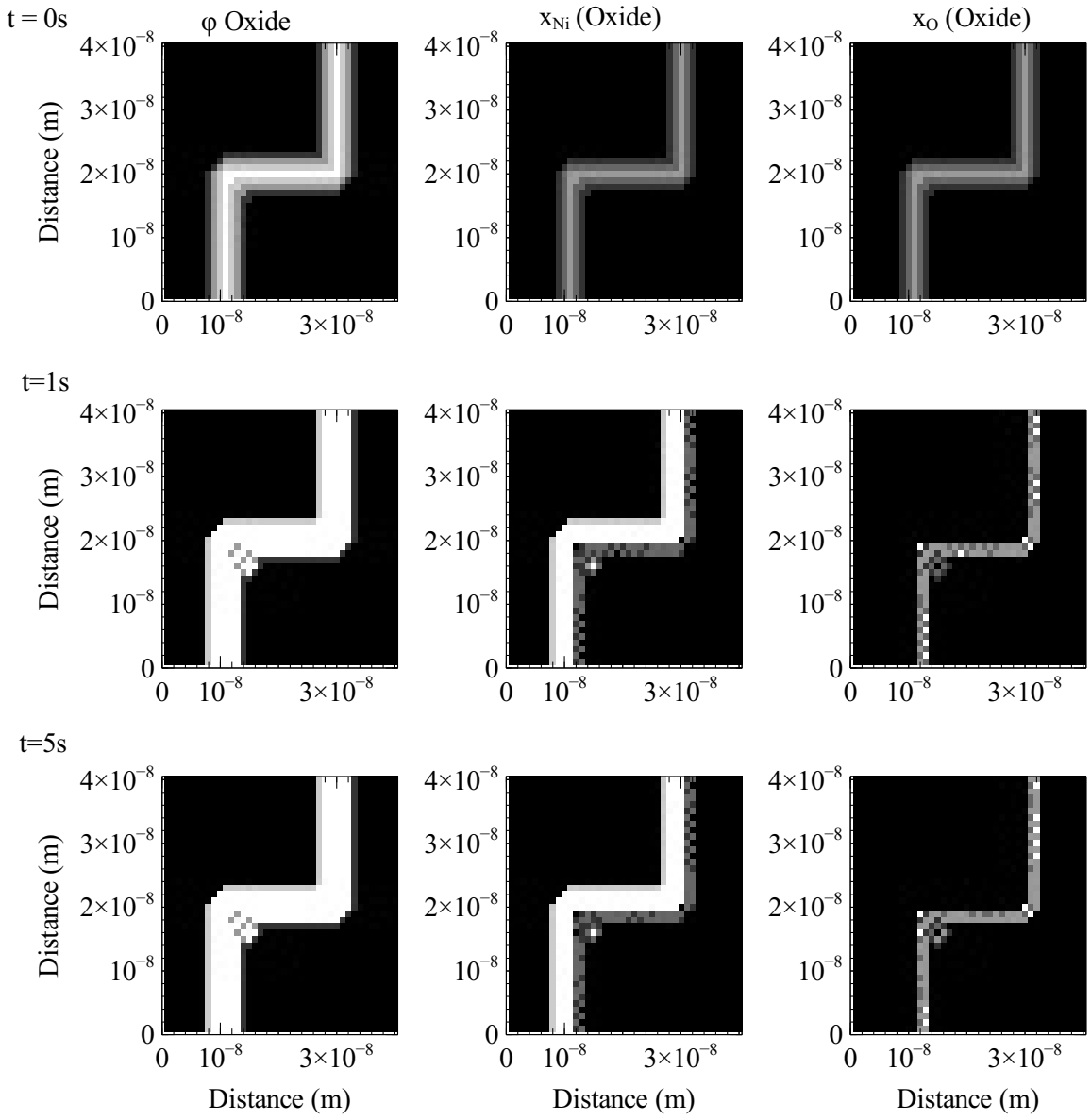

Figure 5.12: 2-Dimensional phase-field simulation growing nickel oxide, after 0, 1 and 5 seconds of simulated time. The nickel concentration within the oxide grows rapidly but without there being any oxygen present within the oxide to form an oxide. The oxygen concentration varies throughout the oxide, with high and low oxygen concentration areas.

the *fcc* , oxide and gas phases changing and becoming more spread out. This feature of the phase-field model is not carried forward into the oxide from the oxide-gas interface. A step forms in the oxide associated with increased oxygen concentration. The increase in oxygen concentration step results in a small volume of gaseous oxygen trapped within the oxide. This interface reaction is not working as intended; the model is designed such that the oxygen increase into the oxide would drive the diffusion of metal away from the *fcc* phase interface towards the gas interface, causing more oxygen to become part of the oxide. Particularly in Figure 5.1 the sharp increase in oxygen concentration does begin to decrease but should not have reached such a high concentration from the initial diffusion of the oxide. Both simulations show a lack of nickel diffusing into the oxide formed on the outer edge of the oxide; this is something that needs further investigation to determine the cause. There are three possible causes for the step-like nature of the gas-oxide phase interface into the oxide phase; the value of the interfacial width η could be incorrect, and the value of the interfacial energy σ could be too large, or the curvature term could be incorrect. Simulations varying both η and σ have been run to determine whether either is the cause of the simulations not being stable.

η has been varied for initial thin (c.f. Figure 5.3 and Figure 5.4) and thick (c.f. Figure 5.5 and Figure 5.6) oxide films. As the value of η increases, the rate of diffusion across the interfaces decreases; therefore, the results for higher values of η show less reaction taking place. There is a greater spread of the interface region for higher values of η; this is seen further into the simulated time. The molar fractions for the thin (c.f. Figure 5.4) simulation shows an increase in oxygen into the oxide at the oxide-gas interface, which reacts and grows slowly. The influence of η on the diffusion rate is clear when looking at the difference between the oxygen and nickel molar fractions after the simulation has been run, as the ratio of oxygen to nickel is sufficiently higher at lower η values. Thicker initial oxides in Figure 5.6 show less of a spike in oxygen concentration within the oxide; there is greater availability of nickel within the oxide than initially seen; this allows nickel already within the oxide to diffuse towards the oxide-gas interface and reduce the concentration of oxygen. At lower values of η, nickel concentration at the interface region is higher than

at higher values of η; a greater diffusivity within the oxide influences this.

Variations for the interfacial energy, σ, have been compared based on the number of simulation steps run. As the value of σ increases, the rate at which the oxide-gas interface has transformed increases. To ensure that the same curvature has occurred, they are compared at the same time step rather than time. In both the thin and thick simulations (c.f. Figure 5.7 and Figure 5.8), there is no noticeable difference at the oxide-gas interface. The lack of difference at the oxide-gas interface also does not show any signs that these effects are influencing the oxide-gas interface reaction producing a step in the phase parameter. Therefore the value of σ is not the cause for the undesirable behaviour in the oxide simulations.

Simulating a region of oxide between the bulk metal and gas phases, assuming that interaction between the three phases in Figure 5.9 causes the oxide region to become thinner and more pronounced. The curvature terms from the two interfaces drive the simulation domain to have sigmoidal forms. As the *fcc* -oxide interface transforms, a small amount of oxide forms within the *fcc* phase, with a composition purely of nickel; this is unphysical and is caused by the initial curvature terms at the interface.

Simulations focusing on the oxide-gas interface show oxygen transport into the oxide from the gas phase; this increase in oxygen drives nickel towards the gas phase. As nickel travels from the bulk oxide to the gas phase, it allows nickel to diffuse from the bulk metal into the oxide. In both situations, the oxide side of the interface becomes more step-like; this is intended to be a sigmoidal shape. Figure 5.11 shows how for greater amounts of oxygen in the initially sigmoidal-shaped simulation results in a greater amount of oxygen moving into the oxide than the sharper initial step between the two phases in Figure 5.10.

Figure 5.12 shows 2-Dimensional results with undesirable oxide growth, the issues addressed with the oxide-gas curvature influencing and distorting the results produced from the 2D simulation. Regions within the oxide have both high and low concentrations, resulting from the curvature term within the phase-field model being unsuitable. The nickel diffusion into the oxide seems to be irrespective of any oxygen within the oxide; such issues

will be investigated once the unknown regarding the oxygen-gas interface curvature issue is resolved. This 2D simulation results in sharp interfaces on the oxide phase, whereas previously in Figure 5.1, only a sharp interface was seen at the oxide-gas interface. Despite the result being unimpressive, it shows that the model can simulate more complex geometries and morphologies once the issues in the model are resolved.

5.5 Conclusion

A phase field model has been developed that considers the oxidation reaction's thermodynamics, including the ability to simulate the three different phase interactions. This work uses nickel oxide, using the same thermodynamics and mobilities used within Chapter 4. Furthermore the modelling method has been shown to work for 2-dimensional simulation domains in Figure 5.12. The current state of the numerical model's curvature term at the oxide-gas interface is insufficient to describe the oxidation as it creates an interface that does not exhibit the expected sigmoidal profile. A phase field model that is capable of modelling the growth of oxide using thermodynamically available data that works in a manner that enables the scaling of the model to include multiple elements allows the possibility for more complex compositions to be modelled. Expanding the phase-field model to include different effects such as grain boundaries and stresses within the oxide would enable the work currently developed to be suitable for describing complex 2D and 3D structures to provide an understanding of different morphologies and alloying contributions to oxidation.

Chapter 6

Conclusion

Within this thesis, work has been undertaken to incorporate interfacial reactions into a diffusion equation [1]; Figure 3.11 shows the model simulating the growth of precipitates phases with a variety of different alloying contributions. The reaction equation has been modified to simulate oxidation growth at the metal-oxide interface. The oxide-gas interface reaction has been developed; Figure 4.4 shows these interfacial reactions being used together to simulate the growth of pure nickel oxide. These flux equations have been modified to be phase-field consistent and subsequently used to create a phase-field model to simulate the growth of nickel oxide. Figure 5.1 and Figure 5.12 has simulated both 1D and 2D simulation domains respectively; including the three phases interacting together in Figure 5.9.

Figure 3.7 shows the developed precipitate growth model suitable for simulating the growth of precipitates being suitable to provide a similar growth profile to that provided by DICTRA. The simulations have been used to simulate a ternary precipitate; however, there is an artefact within the simulations that is undesirable; Figure 3.11 shows oscillating concentration of the metallic phases in the oxide, which is the result of the way that the simulation is set up. The growth of nickel oxide has been simulated with similar conditions to [2], giving the best opportunity for comparison. The calculated k_p values from the simulations were at temperatures between $1000 - 1200°C$. These k_p results are used

to determine the rate at which oxygen is included in the oxide (k_c) and what interface mobility modifier (M^I) is needed at the metal-oxide interface. The value of k_c increased from approximately 15 to 60s^{-1} (c.f. Figure 4.10) as the temperature increased. At the metal-oxide interface, the interface diffusivity was found to be $1 \times 10^{-4} - 1 \times 10^{-5}$ times bulk metal diffusion within the metal phase for all simulated temperatures. Currently, the curvature contribution for the interface reaction between the oxide and gas phases is not working as intended; the interface into the oxide becomes step-like rather than the expected diffuse sigmoidal interface. Investigations into what effect the interfacial energy (σ) has on thin and thick initial oxides are shown in Figure 5.7 and Figure 5.8 respectively. Additionally the effect of interfacial width (η) on thin and thick initial oxides shown in Figure 5.3 and Figure 5.5 respectively have been performed, these simulations show the issue is with the curvature contribution.

Work conducted for this thesis now has provided a thermodynamical method for determining the interface reaction, for the reaction between metal and precipitate phases and metal and oxide phases. Such a method can use the chemical potential driving force for the different elements or the mass action law. The oxidation scheme developed is suitable for simulating the growth of nickel oxide with an agreement to experimental data. There, however, is a requirement to change how experimental data is reported by providing the parabolic number n. The parabolic number n provides numerical models to be more accurate in simulating the correct kinetic and thermodynamic processes. Oxidation work was done by comparing the k_p values provides a good agreement, but the experimental data cannot be used to compare the kinetic and thermodynamic processes occurring within the model. This work has produced a phase field model that can simulate oxidation, taking into consideration effects from the bulk metal and the gas phase and is computed based on the concentrations and chemical potentials of the different elements. The model can be slightly adjusted to consider the effects of multiple elements, provided that there is suitable thermodynamic data.

The work to develop a precipitate growth model is sufficient to model systems with greater complexity than a binary case; a ternary example has been shown within this work. The

model is defined, allowing it to be scaled depending upon the system to be modelled. Developing an oxidation model can provide a greater understanding of estimated values of k_c value and M^I. This technique addresses the problem by not stating the exponent n from the experiment, as only k_p was provided. Having greater detail in the experimental results would only increase the confidence within the k_c and M^I values. The oxide diffusion scheme requires CALPHAD assessments to consider the presence of vacancies more in their data to be suitable for modelling numerically. The Cobalt-Oxide CALPHAD assessment [265] disregarded this non-stoichiometry as it was low and therefore negligible; such an assumption limits the relevant data for modelling within these techniques. A diffusion consistent phase field model based on the reaction's thermodynamics and diffusion flux; allows the model to be suitable for modelling diffusion fluxes that are the result of thermodynamic driving forces and interface reactions. Demonstrations of simulating an oxide's growth consider the thermodynamic reaction at the oxide-metal interface.

Ternary simulations for modelling oxides need some further work to ensure that the correct molar fractions are arrived at and that no charge balancing issues are causing the simulations to be unstable. Running experimental oxidation simulations with known k_p and exponent n values to ensure that the correct k_c and M^I values are achieved during the simulations to provide further confidence in the simulated values. The effects of electric fields on the diffusion of metal across the oxide scale are not included in this work; the adjustment of the chemical potentials to consider the moving charge's possibilities would influence the diffusion rates and should be included. A binary case for the phase-field model has been simulated; increasing the complexity of such an oxide to simulate a ternary or greater system would be beneficial to show the ability of the model to scale based on the alloy complexity. Including a range of different physical effects in the phase field model, such as grain boundaries, stress and strain and creep, would enable the phase field model to be more suitable for creating a realistic model for the growth and effects of oxides on a variety of different metals.

References

[1] H. Larsson, H. Strandlund, and M. Hillert, "Unified treatment of kirkendall shift and migration of phase interfaces," *Acta Materialia*, vol. 54, no. 4, pp. 945–951, 2006.

[2] R. Haugsrud, "On the high-temperature oxidation of nickel," *Corrosion Science*, vol. 45, no. 1, pp. 211–235, 2003.

[3] N. Das, "Advances in nickel-based cast superalloys," *Transactions of the Indian Institute of Metals*, vol. 63, no. 2, pp. 265–274, 2010.

[4] R. Ali, T. Shehbaz, and E. Bemporad, "Investigation on failure in thermal barrier coatings on gas turbine first-stage rotor blade," *Journal of Failure Analysis and Prevention*, vol. 18, no. 5, pp. 1062–1072, 2018.

[5] S. Garruchet, O. Politano, P. Arnoux, and V. Vignal, "Diffusion of oxygen in nickel: A variable charge molecular dynamics study," *Solid State Communications*, vol. 150, no. 9-10, pp. 439–442, 2010.

[6] E. H. Megchiche, M. Amarouche, and C. Mijoule, "First-principles calculations of the diffusion of atomic oxygen in nickel: thermal expansion contribution," *Journal of Physics: Condensed Matter*, vol. 19, no. 29, p. 296201, 2007.

[7] C. Athreya, K. Deepak, D.-I. Kim, B. de Boer, S. Mandal, and V. S. Sarma, "Role of grain boundary engineered microstructure on high temperature steam oxidation behaviour of ni based superalloy alloy 617," *Journal of Alloys and Compounds*, vol. 778, pp. 224 – 233, 2019.

[8] F. A. Pérez-González, J. H. Ramírez-Ramírez, M. Terock, N. F. Garza-Montes-de Oca, U. Glatzel, and R. Colás, "High-temperature oxidation of a nickel base superalloy at different oxygen partial pressures," *Corrosion Engineering, Science and Technology*, vol. 51, no. 7, pp. 513–521, 2016.

[9] J. Sun, S. M. Jiang, H. J. Yu, S. B. Liu, J. Gong, and C. Sun, "Oxidation behaviour of Pt modified aluminized NiCrAlYSi coating on a Ni-based single crystal superalloy," *Corrosion Science*, 2018.

[10] A. de Vasconcelos Varela, H. D. de Deus, M. C. ao de Siqueira, M. C. Rezende, and L. H. de Almeida, "Oxidation assisted intergranular cracking in 718 Nickel Superalloy: on the mechanism of dynamic embrittlement," *Journal of Materials Research and Technology*, 2018.

[11] C. Zou, Y. Kyung Shin, A. C. T. van Duin, H. Fang, and Z.-K. Liu, "Molecular dynamics simulations of the effects of vacancies on nickel self-diffusion, oxygen diffusion and oxidation initiation in nickel, using the ReaxFF reactive force field," *Acta Materialia*, vol. 83, pp. 102–112, 2015.

[12] T. D. Reynolds, M. P. Taylor, D. J. Child, and H. E. Evans, "The effect of elevated air pressure on the oxidation properties of the nickel-based superalloy, RR1000, at 650°C with different surface modifications," *Materials at High Temperatures*, vol. 35, no. 1-3, pp. 130–140, 2018.

[13] B. Albert, R. Völkl, and U. Glatzel, "High-temperature oxidation behavior of two nickel-based superalloys produced by metal injection molding for aero engine applications," *Metallurgical and Materials Transactions A*, vol. 45, no. 10, pp. 4561–4571, 2014.

[14] B. J. Foss, M. C. Hardy, D. J. Child, D. S. McPhail, and B. A. Shollock, "Oxidation of a commercial nickel-based superalloy under static loading," *JOM*, vol. 66, no. 12, pp. 2516–2524, 2014.

[15] F. Yuan, E. Han, C. Jo, T. Li, and Z. Hu, "The effect of crystallographic orientation on the oxidation behavior of a single-crystal nickel-base superalloy," *Oxidation of Metals*, vol. 60, no. 3, pp. 211–224, 2003.

[16] M. Yang, J. Zhang, H. Wei, W. Gui, H. Su, T. Jin, and L. Liu, "A phase-field model for creep behavior in nickel-base single–crystal superalloy: Coupled with creep damage," *Scripta Materialia*, vol. 147, pp. 16–20, 2018.

[17] A. Sato, H. Harada, T. Yokokawa, T. Murakumo, Y. Koizumi, T. Kobayashi, and H. Imai, "The effects of ruthenium on the phase stability of fourth generation Ni-base single crystal superalloys," *Scripta Materialia*, vol. 54, no. 9, pp. 1679–1684, 2006.

[18] N. Ta, L. Zhang, Y. Tang, W. Chen, and Y. Du, "Effect of temperature gradient on microstructure evolution in Ni–Al–Cr bond coat/substrate systems: A phase-field study," *Surface and Coatings Technology*, vol. 261, pp. 364–374, 2015.

[19] H. Zhang, Y. Liu, X. Chen, H. Zhang, and Y. Li, "Microstructural homogenization and high-temperature cyclic oxidation behavior of a Ni-based superalloy with high–Cr content," *Journal of Alloys and Compounds*, vol. 727, pp. 410–418, 2017.

[20] A. Srivastava, S. Gopagoni, A. Needleman, V. Seetharaman, A. Staroselsky, and R. Banerjee, "Effect of specimen thickness on the creep response of a Ni-based single-crystal superalloy," *Acta Materialia*, vol. 60, no. 16, pp. 5697 – 5711, 2012.

[21] A. Sato, Y. L. Chiu, and R. C. Reed, "Oxidation of nickel-based single-crystal superalloys for industrial gas turbine applications," *Acta Materialia*, vol. 59, no. 1, pp. 225–240, 2011.

[22] A. Sato, Y. lung Chiu, E. A. Marquis, and R. C. Reed, "Characterisation of oxide scale formation on a new single crystal superalloy for power generation applications," *Materials at High Temperatures*, vol. 29, no. 3, pp. 272–278, 2012.

[23] B. G. Cade, W. F. Caley, and N. L. Richards, "Comparison of oxidation performance of two nickel base superalloys for turbine applications," *Canadian Metallurgical Quarterly*, vol. 53, no. 4, pp. 460–468, 2014.

[24] Z. Zhu, H. Basoalto, N. Warnken, and R. C. Reed, "A model for the creep deformation behaviour of nickel-based single crystal superalloys," *Acta Materialia*, vol. 60, no. 12, pp. 4888–4900, 2012.

[25] D. J. Crudden, B. Raeisinia, N. Warnken, and R. C. Reed, "Analysis of the chemistry of ni-base turbine disk superalloys using an alloys-by-design modeling approach," *Metallurgical and Materials Transactions A*, vol. 44, no. 5, pp. 2418–2430, 2013.

[26] H. ur Rehman, K. Durst, S. Neumeier, A. B. Parsa, A. Kostka, G. Eggeler, and M. Göken, "Nanoindentation studies of the mechanical properties of the μ phase in a creep deformed Re containing nickel-based superalloy," *Materials Science and Engineering: A*, vol. 634, pp. 202 – 208, 2015.

[27] H. Long, S. Mao, Y. Liu, Z. Zhang, and X. Han, "Microstructural and compositional design of Ni-based single crystalline superalloys – A review," *Journal of Alloys and Compounds*, vol. 743, pp. 203–220, 2018.

[28] D. W. Yun, S. M. Seo, H. W. Jeong, and Y. S. Yoo, "Effect of refractory elements and Al on the high temperature oxidation of Ni-base superalloys and modelling of their oxidation resistance," *Journal of Alloys and Compounds*, vol. 710, pp. 8 – 19, 2017.

[29] R. Wu, K. Kawagishi, H. Harada, and R. Reed, "The retention of thermal barrier coating systems on single-crystal superalloys: Effects of substrate composition," *Acta Materialia*, vol. 56, no. 14, pp. 3622 – 3629, 2008.

[30] S.-J. Park, S.-M. Seo, Y.-S. Yoo, H.-W. Jeong, and H. Jang, "Effects of Al and Ta on the high temperature oxidation of Ni-based superalloys," *Corrosion Science*, vol. 90, pp. 305 – 312, 2015.

[31] K. A. Unocic, D. Shin, R. R. Unocic, and L. F. Allard, "NiAl oxidation reaction processes studied in situ using MEMS–based closed–cell gas reaction transmission electron microscopy," *Oxidation of Metals*, vol. 88, no. 3, pp. 495–508, 2017.

[32] H. Pei, Z. Wen, Z. Li, Y. Zhang, and Z. Yue, "Influence of surface roughness on the oxidation behavior of a Ni–4.0Cr–5.7Al single crystal superalloy," *Applied Surface Science*, 2018.

[33] X.-F. Zhou, G. Chen, Y.-Y. Feng, Z.-X. Qi, M.-Z. Wang, P. Li, and J.-L. Cheng, "Isothermal oxidation behavior of a new Re-free nickel-based single-crystal superalloy at 950 °C," *Rare Metals*, vol. 36, no. 8, pp. 617–621, 2017.

[34] J. Johnson, J. Nicholls, R. Hurst, and P. Hancock, "The mechanical properties of surface oxides on nickel-base superalloys—i. oxidation," *Corrosion Science*, vol. 18, no. 6, pp. 527 – 541, 1978.

[35] T. Boll, K. A. Unocic, B. A. Pint, A. Mårtensson, and K. Stiller, "Grain boundary chemistry and transport through alumina scales on NiAl alloys," *Oxidation of Metals*, vol. 88, no. 3, pp. 469–479, 2017.

[36] Y. Ru, H. Zhang, Y. Pei, Y. Fu, S. Li, S. Gong, and H. Xu, "New type of γ' phase in Ni based single crystal superalloys: Its formation mechanism and strengthening effect," *Materials & Design*, vol. 145, pp. 181–195, 2018.

[37] M. Perrut, P. Caron, M. Thomas, and A. Couret, "High temperature materials for aerospace applications: Ni-based superalloys and γ-TiAl alloys," *Comptes Rendus Physique*, vol. 19, no. 8, pp. 657 – 671, 2018. New trends in metallic alloys / Alliages métalliques : nouvelles tendances.

[38] M. Huang and J. Zhu, "An overview of rhenium effect in single-crystal superalloys," *Rare Metals*, vol. 35, no. 2, pp. 127–139, 2016.

[39] A. Evangelou, K. A. Soady, S. Lockyer, N. Gao, and P. A. S. Reed, "Oxidation behaviour of single crystal nickel-based superalloys: intermediate temperature effects at 450–550°C," *Materials Science and Technology*, vol. 34, no. 14, pp. 1–14, 2018.

[40] C. S. Giggins and F. S. Pettit, "Oxidation of Ni-Cr-Al alloys between 1000° and 1200°C," *Journal of The Electrochemical Society*, vol. 118, no. 11, p. 1782, 1971.

[41] Z.-y. Zhu, Y.-f. Cai, Y.-j. Gong, G.-p. Shen, Y.-g. Tu, and G.-f. Zhang, "Isothermal oxidation behavior and mechanism of a nickel-based superalloy at 1000°C," *International Journal of Minerals, Metallurgy, and Materials*, vol. 24, no. 7, pp. 776–783, 2017.

[42] N. Sheng, K. Horke, A. Meyer, M. R. Gotterbarm, R. Rettig, and R. F. Singer,

"Surface recrystallization and its effect on oxidation of superalloy C263," *Corrosion Science*, vol. 128, pp. 186–197, 2017.

[43] P. Berthod and L. Toubal, "Dependence of titanium carbide stability at elevated temperatures on Co content in Co(Ni)-25Cr-1.6Ti-0.4C superalloys," *Materials Chemistry and Physics*, vol. 212, pp. 260–267, 2018.

[44] F. H. Stott, "Influence of alloy additions on oxidation," *Materials Science and Technology*, vol. 5, no. 8, pp. 734–740, 1989.

[45] D. Ram, G. Tatlock, and U. Falke, "Segregation of reactive elements at oxide grain boundaries in FeCrAlRE alloys," *Materials at High Temperatures*, vol. 22, no. 3-4, pp. 497–503, 2005.

[46] Q. Wu, H. M. Chan, J. M. Rickman, and M. P. Harmer, "Effect of Hf 4+ concentration on oxygen grain-boundary diffusion in alumina," *Journal of the American Ceramic Society*, vol. 98, no. 10, pp. 3346–3351, 2015.

[47] T. M. Angeliu and G. S. Was, "The effect of chromium, carbon, and yttrium on the oxidation of nickel-base alloys in high temperature water," *Journal of The Electrochemical Society*, vol. 140, no. 7, pp. 1877–1883, 1993.

[48] Y. xin Xu, W. ya Li, and X. wei Yang, "Influence of alloyed Fe on corrosion of Ni–Cr alloys in molten silicates and the effects of pre–oxidation treatment," *Corrosion Science*, vol. 134, pp. 179–188, 2018.

[49] R. C. Reed, *Superalloys - Fundamentals and Applications.* Cambridge University Press, 2006.

[50] W. Huang and Y. A. Chang, "Thermodynamic properties of the Ni–Al–Cr system," *Intermetallics*, vol. 7, no. 8, pp. 863–874, 1999.

[51] H. T. Mallikarjuna, W. F. Caley, and N. L. Richards, "Oxidation kinetics and oxide scale characterization of nickel-based superalloy IN738LC at 900°C," *Journal of Materials Engineering and Performance*, vol. 26, no. 10, pp. 4838–4846, 2017.

[52] M. T. Lapington, D. J. Crudden, R. C. Reed, M. P. Moody, and P. A. J. Bagot, "Characterization of phase chemistry and partitioning in a family of high-strength nickel-based superalloys," *Metallurgical and Materials Transactions A*, vol. 49, no. 6, pp. 2302–2310, 2018.

[53] Y. Hu, L. Zhang, T. Cao, C. Cheng, P. Zhao, G. Guo, and J. Zhao, "The effect of thickness on the creep properties of a single-crystal nickel-based superalloy," *Materials Science and Engineering: A*, vol. 728, pp. 124–132, 2018.

[54] D. Cao, N. Ta, and L. Zhang, "Unit-cell design for two-dimensional phase-field

simulation of microstructure evolution in single-crystal Ni-based superalloys during solidification," *Progress in Natural Science: Materials International*, vol. 27, no. 6, pp. 678–686, 2017.

[55] J.-D. Cao, J.-S. Zhang, Y.-Q. Hua, Z. Rong, R.-F. Chen, and Y.-X. Ye, "High temperature oxidation behavior of Ni-based superalloy GH586 in air," *Rare Metals*, vol. 36, no. 11, pp. 878–885, 2017.

[56] M. Roy, "Approaches to enhance elevated temperature erosion resistance of Ni-base superalloys," *Materials at High Temperatures*, vol. 36, no. 2, pp. 142–156, 2019.

[57] Y. L. Guével, B. Grégoire, M. Cristóbal, X. Feaugas, A. Oudriss, and F. Pedraza, "Dissolution and passivation of aluminide coatings on model and Ni-based superalloy," *Surface and Coatings Technology*, vol. 357, pp. 1037 – 1047, 2019.

[58] L. Klein, B. von Bartenwerffer, M. Killian, P. Schmuki, and S. Virtanen, "The effect of grain boundaries on high temperature oxidation of new γ'–strengthened Co–Al–W–B superalloys," *Corrosion Science*, vol. 79, pp. 29 – 33, 2014.

[59] C. Li, X. Xu, S. Wang, C. Cai, S. Ju, J. Huang, and S. Yang, "Microstructure and properties of Al and Al-Cr coatings on nickel-based superalloy GH625 by a thermal diffusion process," *Materials Research Express*, vol. 6, no. 4, p. 046426, 2019.

[60] X.-x. Yu, A. Gulec, C. M. Andolina, E. J. Zeitchick, K. Gusieva, J. C. Yang, J. R. Scully, J. H. Perepezko, and L. D. Marks, "In situ observations of early stage oxidation of Ni-Cr and Ni-Cr-Mo alloys," *CORROSION*, vol. 74, no. 9, pp. 939–946, 2018.

[61] R. Wang, B. Zhang, D. Hu, K. Jiang, J. Mao, and F. Jing, "A critical-plane-based thermomechanical fatigue lifetime prediction model and its application in nickel-based single-crystal turbine blades," *Materials at High Temperatures*, vol. 36, no. 4, pp. 325–334, 2019.

[62] X. Yu, P. Song, X. He, A. Khan, T. Huang, C. Li, Q. Li, K. Lü, K. Chen, and J. Lu, "Influence of the combined-effect of NaCl and Na2SO4 on the hot corrosion behaviour of aluminide coating on Ni-based alloys," *Journal of Alloys and Compounds*, vol. 790, pp. 228 – 239, 2019.

[63] R. S. Bangari, S. Sahu, and P. C. Yadav, "Comparative evaluation of hot corrosion resistance of nanostructured AlCrN and TiAlN coatings on cobalt-based superalloys," *Journal of Materials Research*, pp. 1–9, 2018.

[64] B. Yu, Y. Li, Y. Nie, and H. Mei, "High temperature oxidation behavior of a novel cobalt-nickel-base superalloy," *Journal of Alloys and Compounds*, vol. 765, pp. 1148–1157, 2018.

[65] G. Teodorescu, P. D. Jones, R. A. Overfelt, and B. Guo, "High temperature, spectral-directional emittance of high purity nickel oxidized in air," *Journal of Materials Science*, vol. 41, no. 21, pp. 7240–7246, 2006.

[66] A. Karabela, L. G. Zhao, B. Lin, J. Tong, and M. C. Hardy, "Oxygen diffusion and crack growth for a nickel-based superalloy under fatigue-oxidation conditions," *Materials Science and Engineering: A*, vol. 567, pp. 46–57, 2013.

[67] Y. Hu, C. Cheng, L. Zhang, T. Cao, G. Guo, X. Meng, and J. Zhao, "Microstructural evolution of oxidation film on a single crystal nickel–based superalloy at 980°C," *Oxidation of Metals*, pp. 303–317, 2018.

[68] R. Jiang, S. Everitt, N. Gao, K. Soady, J. W. Brooks, and P. A. S. Reed, "Influence of oxidation on fatigue crack initiation and propagation in turbine disc alloy N18," *International Journal of Fatigue*, vol. 75, pp. 89–99, 2015.

[69] A. Karabela, L. Zhao, J. Tong, N. Simms, J. Nicholls, and M. Hardy, "Effects of cyclic stress and temperature on oxidation damage of a nickel-based superalloy," *Materials Science and Engineering: A*, vol. 528, no. 19, pp. 6194 – 6202, 2011.

[70] M. Petrenec, J. Polák, J. Tobiáš, M. Šmíd, A. Chlupová, and R. Petráš, "Analysis of cyclic plastic response of nickel based IN738LC superalloy," *International Journal of Fatigue*, vol. 65, pp. 44 – 50, 2014. Fatigue of Metallic Materials - Mechanisms and Life Estimation.

[71] C. Xu, Z.-H. Yao, J.-X. Dong, and Y.-K. Jiang, "Mechanism of high-temperature oxidation effects in fatigue crack propagation and fracture mode for FGH97 superalloy," *Rare Metals*, 2018.

[72] S. Everitt, R. Jiang, N. Gao, M. J. Starink, J. W. Brooks, and P. A. S. Reed, "Comparison of fatigue crack propagation behaviour in two gas turbine disc alloys under creep–fatigue conditions: evaluating microstructure, environment and temperature effects," *Materials Science and Technology*, vol. 29, no. 7, pp. 781–787, 2013.

[73] G. Altinkurt, M. Fèvre, G. Geandier, M. Dehmas, O. Robach, and J.-S. Micha, "Local strain redistribution in a coarse-grained nickel-based superalloy subjected to shot-peening, fatigue or thermal exposure investigated using synchrotron x-ray laue microdiffraction," *Journal of Materials Science*, 2018.

[74] L. Valle, A. Santana, M. Rezende, J. Dille, O. Mattos, and L. de Almeida, "The influence of heat treatments on the corrosion behaviour of nickel-based alloy 718," *Journal of Alloys and Compounds*, vol. 809, p. 151781, 2019.

[75] J. J. deBarbadillo and S. K. Mannan, "Alloy 718 for oilfield applications," *JOM*, vol. 64, no. 2, pp. 265–270, 2012.

[76] Y. Xie, J. Zhang, and D. J. Young, "Temperature effect on oxidation behavior of Ni-Cr alloys in CO2 gas atmosphere," *Journal of The Electrochemical Society*, vol. 164, no. 6, pp. C285–C293, 2017.

[77] A. Sato, J. J. Moverare, M. Hasselqvist, and R. C. Reed, "On the oxidation resistance of nickel-based superalloys," in *Euro Superalloys 2010*, vol. 278 of *Advanced Materials Research*, pp. 174–179, Trans Tech Publications, 2011.

[78] S. Pedrazzini, E. S. Kiseeva, R. Escoube, H. M. Gardner, J. O. Douglas, A. Radecka, P. M. Mignanelli, G. M. Hughes, G. Chapman, P. D. Edmondson, H. J. Stone, D. De Lille, and P. A. J. Bagot, "In–service oxidation and microstructural evolution of a nickel superalloy in a formula 1 car exhaust," *Oxidation of Metals*, pp. 375–394, 2017.

[79] P. Stoyanov, L. Dawag, W. J. Joost, D. G. Goberman, and S. Ivory, "Insights into the static friction behavior of Ni-based superalloys," *Surface and Coatings Technology*, vol. 352, pp. 634 – 641, 2018.

[80] L. S. Araujo, D. S. dos Santos, S. Godet, J. Dille, A. L. Pinto, and L. H. de Almeida, "Analysis of grain boundary character in a fine-grained nickel-based superalloy 718," *Journal of Materials Engineering and Performance*, vol. 23, no. 11, pp. 4130–4135, 2014.

[81] A. P. Gordon, M. D. Trexler, R. W. Neu, T. J. Sanders, and D. L. McDowell, "Corrosion kinetics of a directionally solidified Ni-base superalloy," *Acta Materialia*, vol. 55, no. 10, pp. 3375 – 3385, 2007.

[82] J. Lv, "Effect of grain size on mechanical property and corrosion resistance of the Ni-based alloy 690," *Journal of Materials Science & Technology*, vol. 34, no. 9, pp. 1685–1691, 2018.

[83] S. B. Mishra, K. Chandra, and S. Prakash, "Studies on erosion-corrosion behaviour of plasma sprayed Ni3Al coating in a coal-fired thermal power plant environment at 540°C ," *Anti-Corrosion Methods and Materials*, vol. 64, no. 5, pp. 540–549, 2017.

[84] T. R. Dewa, H. J. Park, J. S. Kim, and Y. S. Lee, "High-temperature creep-fatigue behavior of alloy 617," *Metals*, vol. 8, no. 2, 2018.

[85] R. Zhu, J. Wang, H. Ming, Z. Zhang, and E.-H. Han, "Evaluation of stress corrosion cracking susceptibility of forged 316 stainless steel in simulated primary water," *Materials and Corrosion*, vol. 69, no. 3, pp. 328–336, 2018.

[86] P. Kontis, D. M. Collins, A. J. Wilkinson, R. C. Reed, D. Raabe, and B. Gault, "Microstructural degradation of polycrystalline superalloys from oxidized carbides and implications on crack initiation," *Scripta Materialia*, vol. 147, pp. 59–63, 2018.

[87] I. W. Vance and P. C. Millett, "Phase-field simulations of pore migration and morphology change in thermal gradients," *Journal of Nuclear Materials*, vol. 490, pp. 299–304, 2017.

[88] J. Jiang, T. Zhou, W. Shao, and C. Zhou, "Interdiffusion behavior and lifetime prediction of Co-Al coating on Ni-based superalloy," *Journal of Alloys and Compounds*, vol. 786, pp. 920 – 929, 2019.

[89] S.-L. Li, H.-Y. Qi, and X.-G. Yang, "Oxidation-induced damage of an uncoated and coated nickel-based superalloy under simulated gas environment," *Rare Metals*, 2017.

[90] B. Cassenti and A. Staroselsky, "The effect of thickness on the creep response of thin-wall single crystal components," *Materials Science and Engineering: A*, vol. 508, no. 1, pp. 183 – 189, 2009.

[91] H. Chi, M. T. Curnan, M. Li, C. M. Andolina, W. A. Saidi, G. Veser, and J. C. Yang, "In situ environmental TEM observation of two-stage shrinking of Cu2O islands on Cu(100) during methanol reduction," *Phys. Chem. Chem. Phys.*, pp. –, 2020.

[92] F. Hess, A. Farkas, A. P. Seitsonen, and H. Over, ""first-principles" kinetic monte carlo simulations revisited: CO oxidation over RuO2(110)," *Journal of Computational Chemistry*, vol. 33, no. 7, pp. 757–766, 2012.

[93] Y. Fu, J. G. Michopoulos, and J.-H. Song, "Bridging the multi phase-field and molecular dynamics models for the solidification of nano-crystals," *Journal of Computational Science*, vol. 20, pp. 187–197, 2017.

[94] L. Ai, Y. Zhou, H. Huang, Y. Lv, and M. Chen, "A reactive force field molecular dynamics simulation of nickel oxidation in supercritical water," *The Journal of Supercritical Fluids*, vol. 133, pp. 421–428, 2018.

[95] S. Alavi, J. W. Mintmire, and D. L. Thompson, "Molecular dynamics simulations of the oxidation of aluminum nanoparticles," *The Journal of Physical Chemistry B*, vol. 109, no. 1, pp. 209–214, 2005. PMID: 16851006.

[96] H. Larsson, T. Jonsson, R. Naraghi, Y. Gong, R. C. Reed, and J. Ågren, "Oxidation of iron at 600°C - experiments and simulations," *Materials and Corrosion*, vol. 68, no. 2, pp. 133–142, 2016.

[97] K. Kim, Q. C. Sherman, L. K. Aagesen, and P. W. Voorhees, "Phase-field model of oxidation: Kinetics," *Phys. Rev. E*, vol. 101, p. 022802, 2020.

[98] B. Lesage, A. M. Huntz, and P. Lacombe, "Relation between cationic self-diffusion in nickel oxide and nickel oxidation," *Solid State Ionics*, vol. 12, pp. 359–363, 1984.

[99] A. M. Huntz, A. Lefeuvre, M. Andrieux, C. Severac, G. Moulin, R. Molins, and F. Jomard, "Stress and oxidation of nickel according to its purity," *Materials at High Temperatures*, vol. 20, no. 4, p. 639, 2003.

[100] Y. H. Wen, J. P. Simmons, C. Shen, C. Woodward, and Y. Wang, "Phase-field modeling of bimodal particle size distributions during continuous cooling," *Acta Materialia*, vol. 51, no. 4, pp. 1123–1132, 2003.

[101] T. Kitashima, "Coupling of the phase-field and CALPHAD methods for predicting multicomponent, solid-state phase transformations," *Philosophical Magazine*, vol. 88, no. 11, pp. 1615–1637, 2008.

[102] C. Wagner, "Theoretical analysis of the diffusion processes determining the oxidation rate of alloys," *Journal of The Electrochemical Society*, vol. 99, no. 10, pp. 369–380, 1952.

[103] B. Sundman, Q. Chen, and Y. Du, "A review of calphad modeling of ordered phases," *Journal of Phase Equilibria and Diffusion*, vol. 39, no. 5, pp. 678–693, 2018.

[104] M. Yang, J. Zhang, H. Wei, Y. Zhao, W. Gui, H. Su, T. Jin, and L. Liu, "Study of γ' rafting under different stress states – a phase-field simulation considering viscoplasticity," *Journal of Alloys and Compounds*, vol. 769, pp. 453 – 462, 2018.

[105] X. Wang, B. Wang, M. Meyerson, C. B. Mullins, Y. Fu, L. Zhu, and L. Chen, "A phase-field model integrating reaction-diffusion kinetics and elasto-plastic deformation with application to lithiated selenium-doped germanium electrodes," *International Journal of Mechanical Sciences*, 2018.

[106] G. Haveroth, M. Vale, M. Bittencourt, and J. Boldrini, "A non-isothermal thermodynamically consistent phase field model for damage, fracture and fatigue evolutions in elasto-plastic materials," *Computer Methods in Applied Mechanics and Engineering*, vol. 364, p. 112962, 2020.

[107] R. T. Wu, R. Zhu, L. T. Wu, Y. M. Nie, R. C. Reed, K. Kawagishi, and H. Harada, "Thermodynamic assessment of ternary NiCrAl alloys: from calculations to experiments," *Canadian Metallurgical Quarterly*, vol. 50, no. 3, pp. 291–294, 2011.

[108] J. C. Yang, M. Yeadon, B. Kolasa, and J. M. Gibson, "Oxygen surface diffusion in three-dimensional Cu2O growth on Cu(001) thin films," *Applied Physics Letters*, vol. 70, no. 26, pp. 3522–3524, 1997.

[109] R. A. Rapp, "The high temperature oxidation of metals forming cation-diffusing scales," *Metallurgical Transactions A*, vol. 15, no. 5, pp. 765–782, 1984.

[110] F. Gesmundo and F. Viani, "The parabolic rate constant for the high-temperature

oxidation of pure or slightly alloyed nickel and the defect structure of nickel oxide," *Solid State Ionics*, vol. 6, no. 1, pp. 33–42, 1982.

[111] S. F. Frederick and I. Cornet, "The effect of cobalt on the high temperature oxidation of nickel," *Journal of The Electrochemical Society*, vol. 102, no. 6, pp. 285–291, 1955.

[112] A. Kursumovic, R. Tomov, R. Hühne, B. A. Glowacki, J. E. Everts, A. Tuissi, E. Villa, and B. Holzapfel, "High temperature growth kinetics and texture of surface-oxidised NiO for coated superconductor applications," *Physica C: Superconductivity*, vol. 385, no. 3, pp. 337–345, 2003.

[113] F. Stott and G. Wood, "The mechanism of oxidation of dilute Ni–Al alloys at 800–1200°C," *Corrosion Science*, vol. 17, no. 8, pp. 647 – 670, 1977.

[114] F. H. Stott, I. G. Wright, T. Hodgkiess, and G. C. Wood, "Factors affecting the high-temperature oxidation behavior of some dilute nickel- and cobalt-base alloys," *Oxidation of Metals*, vol. 11, no. 3, pp. 141–150, 1977.

[115] T. D. Tribbeck, J. W. Linnett, and P. G. Dickens, "Oxidation of metals and alloys. part 1.—oxidation of nickel containing small amounts of chromium," *Trans. Faraday Soc.*, vol. 65, pp. 890–895, 1969.

[116] Z. Halem, N. Halem, M. Abrudeanu, S. Chekroude, C. Petot, and G. Petot-Ervas, "Transport properties of Al or Cr-doped nickel oxide relevant to the thermal oxidation of dilute Ni-Al and Ni-Cr alloys," *Solid State Ionics*, vol. 297, pp. 13–19, 2016.

[117] N. Halem, M. Abrudeanu, and G. Petot-Ervas, "Al effect in transport properties of nickel oxide and its relevance to the oxidation of nickel," *Materials Science and Engineering: B*, vol. 176, no. 13, pp. 1002 – 1009, 2011.

[118] A. Atkinson, "Transport processes during the growth of oxide films at elevated temperature," *Reviews of Modern Physics*, vol. 57, pp. 437–470, 1985.

[119] A. Atkinson, R. I. Taylor, and P. D. Goode, "Transport processes in the oxidation of ni studied using tracers in growing NiO scales," *Oxidation of Metals*, vol. 13, no. 6, pp. 519–543, 1979.

[120] G. Petot-Ervas and C. Petot, "The influence of impurities segregation phenomena on the oxido-reduction kinetics of oxides," *Journal of Physics and Chemistry of Solids*, vol. 51, no. 8, pp. 901 – 906, 1990.

[121] A. Huntz, M. Andrieux, and R. Molins, "Relation between the oxidation mechanism of nickel, the microstructure and mechanical resistance of NiO films and the nickel

purity: I. oxidation mechanism and microstructure of NiO films," *Materials Science and Engineering: A*, vol. 415, no. 1, pp. 21 – 32, 2006.

[122] N. N. Khoi, W. W. Smeltzer, and J. D. Embury, "Growth and structure of nickel oxide on nickel crystal faces," *Journal of The Electrochemical Society*, vol. 122, no. 11, pp. 1495–1503, 1975.

[123] P. Y. Hou and R. M. Cannon, "Spallation behavior of thermally grown nickel oxide on nickel," *Oxidation of Metals*, vol. 71, no. 5, p. 237, 2009.

[124] P. Y. Hou and R. Cannon, "The stress state in thermally grown NiO scales," *Materials Science Forum*, vol. 251, pp. 325–332, 10 1997.

[125] F. Czerwinski, G. Palumbo, and J. A. Szpunar, "Textures of oxide films grown on nickel electrodeposits," *Scripta Materialia*, vol. 39, no. 10, pp. 1359–1364, 1998.

[126] P. Berthod, Z. Himeur, and P.-J. Panteix, "Influences of the Co content and of the level of high temperature on the microstructure and oxidation of cast Ni, Co-based Cr-rich TaC-containing cast alloys," *Journal of Alloys and Compounds*, vol. 739, pp. 447–456, 2018.

[127] A. Akhtar, S. Hegde, and R. C. Reed, "The oxidation of single-crystal nickel-based superalloys," *JOM*, vol. 58, no. 1, pp. 37–42, 2006.

[128] R. P. Oleksak, C. S. Carney, G. R. Holcomb, and Ö. N. Doğan, "Structural evolution of a Ni alloy surface during high-temperature oxidation," *Oxidation of Metals*, vol. 90, no. 1, pp. 27–42, 2018.

[129] L. Luo, Y. Kang, J. C. Yang, and G. Zhou, "Nucleation and growth of oxide islands during the initial-stage oxidation of (100)Cu-Pt alloys," *Journal of Applied Physics*, vol. 117, no. 6, p. 065305, 2015.

[130] Q. Zhu, W. A. Saidi, and J. C. Yang, "Enhanced mass transfer in the step edge induced oxidation on Cu(100) surface," *J. Phys. Chem. C*, vol. 121, no. 21, pp. 11251–11260, 2017.

[131] H. V. Atkinson, "Evolution of grain structure in nickel oxide scales," *Oxidation of Metals*, vol. 28, no. 5, pp. 353–389, 1987.

[132] A. Atkinson and R. I. Taylor, "The diffusion of Ni in the bulk and along dislocations in NiO single crystals," *Philosophical Magazine A*, vol. 39, no. 5, pp. 581–595, 1979.

[133] A. Atkinson and R. I. Taylor, "The diffusion of 63Ni along grain boundaries in nickel oxide," *Philosophical Magazine A*, vol. 43, no. 4, pp. 979–998, 1981.

[134] F. N. Rhines, R. G. Connell, and M. S. Choi, "Microstructural evolution of the inner

layer of the high temperature oxide scale on nickel," *Journal of The Electrochemical Society*, vol. 126, no. 6, pp. 1061–1066, 1979.

[135] M. C. Noh, K. Jeongjin, W. H. Doh, K.-J. Kim, and J. Y. Park, "Reversible oxygen–driven nickel oxide structural transition on the nickel(1 1 1) surface at near-ambient pressure," *ChemCatChem*, vol. 10, pp. 1–6, 2018.

[136] N. Amiri and H. Behnejad, "Oxidation of nickel surfaces through the energetic impacts of oxygen molecules: Reactive molecular dynamics simulations," *The Journal of Chemical Physics*, vol. 144, no. 14, p. 144705, 2016.

[137] F. Yang, D.-N. Fang, and B. Liu, "A theoretical model and phase field simulation on the evolution of interface roughness in the oxidation process," *Modelling and Simulation in Materials Science and Engineering*, vol. 20, no. 1, pp. 1–12, 2012.

[138] S. Mrowec, "On the mechanism of high temperature oxidation of metals and alloys," *Corrosion Science*, vol. 7, no. 9, pp. 563 – 578, 1967.

[139] G. Zhou, X. Chen, D. Gallagher, and J. C. Yang, "Percolating oxide film growth during Cu(111) oxidation," *Applied Physics Letters*, vol. 93, no. 12, p. 123104, 2008.

[140] L. Luo, Y. Kang, J. C. Yang, and G. Zhou, "Influence of the surface morphology on the early stages of Cu oxidation," *Applied Surface Science*, vol. 259, pp. 791 – 798, 2012.

[141] G. Zhou and J. C. Yang, "In situ UHV-TEM investigation of the kinetics of initial stages of oxidation on the roughened Cu(110) surface," *Surface Science*, vol. 559, no. 2, pp. 100 – 110, 2004.

[142] C.-Q. Cheng, Y.-B. Hu, T.-S. Cao, L. Zhang, Y.-W. Zhu, and J. Zhao, "Two typical oxidation models on nickel-based superalloys under different initial surface roughness," *Corrosion Science*, vol. 176, p. 108942, 2020.

[143] J. L. Evans, "Effect of surface roughness on the oxidation behavior of the ni-base superalloy ME3," *Journal of Materials Engineering and Performance*, vol. 19, no. 7, pp. 1001–1004, 2010.

[144] S. Cruchley, M. Taylor, R. Ding, H. Evans, D. Child, and M. Hardy, "Comparison of chromia growth kinetics in a ni-based superalloy, with and without shot-peening," *Corrosion Science*, vol. 100, pp. 242 – 252, 2015.

[145] X. Montero, A. Ishida, T. Meißner, H. Murakami, and M. Galetz, "Effect of surface treatment and crystal orientation on hot corrosion of a Ni-based single-crystal superalloy," *Corrosion Science*, vol. 166, p. 108472, 2020.

[146] L. Wang, W.-G. Jiang, X.-W. Li, J.-S. Dong, W. Zheng, H. Feng, and L.-H. Lou,

"Effect of surface roughness on the oxidation behavior of a directionally solidified Ni-based superalloy at 1,100 °C," *Acta Metallurgica Sinica (English Letters)*, vol. 28, no. 3, pp. 381–385, 2015.

[147] F. Czerwinski and J. Szpunar, "Controlling the surface texture of nickel for hightemperature oxidation inhibition," *Corrosion Science*, vol. 41, no. 4, pp. 729 – 740, 1999.

[148] X.-x. Yu, A. Gulec, Q. Sherman, K. L. Cwalina, J. R. Scully, J. H. Perepezko, P. W. Voorhees, and L. D. Marks, "Nonequilibrium solute capture in passivating oxide films," *Phys. Rev. Lett.*, vol. 121, p. 145701, 2018.

[149] U. Krupp, V. B. Trindade, P. Schmidt, H. Christ, U. Buschmann, and W. Wiechert, "Oxidation mechanisms of Cr-containing steels and Ni-base alloys at high temperatures Part II: Computer-based simulation," *Materials and Corrosion*, vol. 57, no. 3, pp. 263–268, 2006.

[150] S. Cruchley, H. Evans, M. Taylor, M. Hardy, and S. Stekovic, "Chromia layer growth on a ni-based superalloy: Sub-parabolic kinetics and the role of titanium," *Corrosion Science*, vol. 75, pp. 58 – 66, 2013.

[151] C. Wagner, "The mechanism of the movement of ions and electrons in solids and the interpretation of reactions between solids," *Journal of the Chemical Society, Faraday Transactions*, vol. 34, pp. 851–859, 1938.

[152] C. Wang, S. Ai, and D. Fang, "A phase-field study on the oxidation behavior of Ni considering heat conduction," *Acta Mechanica Sinica/Lixue Xuebao*, vol. 32, no. 5, pp. 1–10, 2016.

[153] G. Gibbs and R. Hales, "The influence of metal lattice vacancies on the oxidation of high temperature materials," *Corrosion Science*, vol. 17, no. 6, pp. 487 – 507, 1977.

[154] J. Harris, "Vacancy injection during oxidation—a re-examination of the evidence," *Acta Metallurgica*, vol. 26, no. 6, pp. 1033 – 1041, 1978.

[155] R. Haugsrud and P. Kofstad, "On the high-temperature oxidation of Cu-rich Cu-Ni alloys," *Oxidation of Metals*, vol. 50, no. 3-4, pp. 189–213, 1998. cited By 48.

[156] P. Hari, N. Arivazhagan, M. Nageswara Rao, and A. Pavan, "Oxidation studies on nickel-base superalloy 617 OCC," *Materials Today: Proceedings*, vol. 27, pp. 2763 – 2767, 2020. International Conference on Materials and Manufacturing Methods – 2019.

[157] C. K. Kim and L. W. Hobbs, "Microstructural evidence for short-circuit oxygen diffusion paths in the oxidation of a dilute Ni-Cr alloy," *Oxidation of Metals*, vol. 45, no. 3, pp. 247–265, 1996.

[158] R. Haugsrud, "On the high-temperature oxidation of Fe, Co, Ni and Cu-based alloys with addition of a less noble element," *Materials Science and Engineering: A*, vol. 298, no. 1, pp. 216–226, 2001.

[159] B. Pieraggi and R. Rapp, "Stress generation and vacancy annihilation during scale growth limited by cation-vacancy diffusion," *Acta Metallurgica*, vol. 36, no. 5, pp. 1281 – 1289, 1988.

[160] G. C. Wood and F. H. Stott, "Oxidation of alloys," *Materials Science and Technology*, vol. 3, no. 7, pp. 519–530, 1987.

[161] M. J. Graham, R. J. Hussey, and M. Cohen, "Influence of oxide structure on the oxidation rate of nickel single crystals," *Journal of The Electrochemical Society*, vol. 120, no. 11, pp. 1523–1529, 1973.

[162] D. M. Duffy and P. W. Tasker, "A calculation of the interaction between impurity ions and grain boundaries in NiO," *Philosophical Magazine A*, vol. 50, no. 2, pp. 155–169, 1985.

[163] D. M. Duffy and P. W. Tasker, "A calculation of the formation energies of intrinsic defects near grain boundaries in NiO," *Philosophical Magazine A*, vol. 50, no. 2, pp. 143–154, 1985.

[164] R. Haugsrud and T. Norby, "Determination of thermodynamics and kinetics of point defects in NiO using the Rosenburg method," *Solid State Ionics*, vol. 111, no. 3, pp. 323–332, 1998.

[165] "Ellingham Diagram." `https://en.wikipedia.org/wiki/Ellingham\_diagram`, 2018.

[166] S. Chevalier, F. Desserrey, and J. P. Larpin, "Oxygen transport during the high temperature oxidation of pure nickel," *Oxidation of Metals*, vol. 64, no. 3, pp. 219–234, 2005.

[167] M. J. Graham and R. J. Hussey, "Analytical techniques in high temperature corrosion," *Oxidation of Metals*, vol. 44, no. 1, pp. 339–374, 1995.

[168] B. D. Bastow, G. C. Wood, and D. Whittle, "The segregation of alloy components in scales and subscales formed by binary alloys of Mn, Fe, Co and Ni," *Corrosion Science*, vol. 25, no. 4, pp. 253–285, 1985.

[169] M. J. Graham, D. Caplan, and M. Cohen, "Growth via leakage paths of nickel oxide on nickel at high temperatures," *Journal of The Electrochemical Society*, vol. 119, no. 9, pp. 1265–1267, 1972.

[170] Y.-H. Wen, L.-Q. Chen, and J. A. Hawk, "Phase-field modeling of corrosion kinetics

under dual-oxidants," *Modelling and Simulation in Materials Science and Engineering*, vol. 20, no. 3, 2012.

[171] C. H. Zhou, H. T. Ma, and L. Wang, "Comparative study of oxidation kinetics for pure nickel oxidized under tensile and compressive stress," *Corrosion Science*, vol. 52, no. 1, pp. 210–215, 2010.

[172] T. R. Fu, P. Tan, J. Ren, and H. S. Wang, "Total hemispherical radiation properties of oxidized nickel at high temperatures," *Corrosion Science*, vol. 83, pp. 272–280, 2014.

[173] C. Dubois, C. Monty, and J. Philibert, "Oxygen self-diffusion in NiO single crystals," *Philosophical Magazine A*, vol. 46, no. 3, pp. 419–433, 1982.

[174] S. Mrowec and Z. Grzesik, "Oxidation of nickel and transport properties of nickel oxide," *Journal of Physics and Chemistry of Solids*, vol. 65, no. 10, pp. 1651–1657, 2004.

[175] R. Farhi and G. Petot-Ervas, "Electrical conductivity and chemical diffusion coefficient measurements in single crystalline nickel oxide at high temperatures," *Journal of Physics and Chemistry of Solids*, vol. 39, no. 11, pp. 1169–1173, 1978.

[176] S. A. Makhlouf, "Electrical properties of NiO films obtained by high-temperature oxidation of nickel," *Thin Solid Films*, vol. 516, no. 10, pp. 3112 – 3116, 2008.

[177] N. L. Peterson, "Impurity diffusion in transition-metal oxides," *Solid State Ionics*, vol. 12, pp. 201–215, 1984.

[178] S. Garruchet, O. Politano, P. Arnoux, and V. Vignal, "A variable charge molecular dynamics study of the initial stage of nickel oxidation," *Applied Surface Science*, vol. 256, no. 20, pp. 5968–5972, 2010.

[179] X. Wang and J. A. Szpunar, "Effects of grain sizes on the oxidation behavior of Ni-based alloy 230 and n," *Journal of Alloys and Compounds*, vol. 752, pp. 40 – 52, 2018.

[180] D. P. Moon, "Duplex scale formation during high-temperature oxidation of Ni-0.1 wt.% Al alloy," *Oxidation of Metals*, vol. 31, no. 1, pp. 71–89, 1989.

[181] J.-H. Ahn, B.-J. Kim, J.-G. Kim, H.-J. Kim, G.-W. Hong, H.-G. Lee, J.-M. Yoo, and H. Pradeep, "Effects of oxidation conditions on the microstructure and texture of NiO in a cube-textured polycrystalline nickel substrate," *Physica C: Superconductivity and its Applications*, vol. 445, pp. 620–624, 2006. Proceedings of the 18th International Symposium on Superconductivity (ISS 2005).

[182] D. J. Young, *High Temperature Oxidation and Corrosion of Metals*. Oxford, UNITED KINGDOM: Elsevier Science & Technology, 2016.

[183] F. Yang, B. Liu, and D.-N. Fang, "Analysis on high-temperature oxidation and growth stress of iron-based alloy using phase field method," *Applied Mathematics and Mechanics (English Edition)*, vol. 32, no. 6, pp. 757–764, 2011.

[184] M. A. Elhelaly, M. A. ElZomor, M. H. Ahmed, and A. O. Youssef, "Effect of zirconium addition on high-temperature cyclic oxidation of diffusion chromo-aluminized Ni-base superalloy," *Oxidation of Metals*, 2018.

[185] A. S. Parlakyigit, T. Gulmez, and A. C. Karaoglanli, "Evaluation of mixed oxide formation and sintering behavior in thermal barrier coatings on nickel-based superalloy," *Materialwissenschaft und Werkstofftechnik*, vol. 49, no. 6, pp. 822–833, 2018.

[186] D. Migas, G. Moskal, M. Mikuśkiewicz, and T. Maciąg, "Thermogravimetric investigations of new γ-γ' cobalt-based superalloys," *Journal of Thermal Analysis and Calorimetry*, vol. 134, no. 1, pp. 119–125, 2018.

[187] H. Wang, H. Wang, Q. Zhao, P. Kan, and B. Xu, "Investigation on hot corrosion behaviour of aluminum rare earth coating in mixed sulphate at 1050°C," *Corrosion Science*, vol. 135, pp. 99–106, 2018.

[188] I. Šulák, K. Obrtlík, L. Čelko, T. Chráska, D. Jech, and P. Gejdoč, "Low cycle fatigue performance of Ni-based superalloy coated with complex thermal barrier coating," *Materials Characterization*, vol. 139, pp. 347–354, 2018.

[189] J. Jung, B. Shollock, and K.-b. Yoo, "Transient oxidation of a nickel-base superalloy with varying oxygen partial pressure," *Oxidation of Metals*, vol. 85, no. 3, pp. 221–229, 2016.

[190] S. Deng, P. Wang, Y. He, and J. Zhang, "Surface microstructure and high temperature oxidation resistance of thermal sprayed NiCoCrAlY bond-coat modified by cathode plasma electrolysis," *Journal of Materials Science & Technology*, vol. 33, no. 9, pp. 1055–1060, 2017.

[191] M. Zagula-Yavorska, M. Wierzbińska, and J. Sieniawski, "Rhodium and hafnium influence on the microstructure, phase composition, and oxidation resistance of aluminide coatings," *Metals*, vol. 7, no. 12, 2017.

[192] G. J. Tatlock and T. J. Hurd, "Platinum and the oxidation behavior of a nickel based superalloy," *Oxidation of Metals*, vol. 22, no. 5, pp. 201–226, 1984.

[193] H. M. Tawancy, "Comparative structure, oxidation resistance and thermal stabil-

ity of CoNiCrAlY overlay coatings with and without Pt and their performance in thermal barrier coatings on a Ni–based superalloy," *Oxidation of Metals*, 2018.

[194] H. M. Tawancy, "Influence of manufacturing route on the oxidation resistance of platinum-modified aluminide bond coatings and their performance in thermal barrier coatings deposited on a ni-based superalloy," *Oxidation of Metals*, 2018.

[195] M. Elsaß, M. Frommherz, and M. Oechsner, "The influence of the coating deposition process on the interdiffusion behavior between nickel–based superalloys and MCrAlY bond coats," *Journal of Thermal Spray Technology*, vol. 27, no. 3, pp. 379–390, 2018.

[196] T. Galiullin, A. Chyrkin, R. Pillai, R. Vaßen, and W. J. Quadakkers, "Effect of alloying elements in Ni-base substrate material on interdiffusion processes in MCrAlY-coated systems," *Surface and Coatings Technology*, 2018.

[197] H. Zhen and X. Peng, "A new approach to manufacture oxidation-resistant NiCrAl overlay coatings by electrodeposition," *Corrosion Science*, vol. 150, pp. 121 – 126, 2019.

[198] N. P. Padture, M. Gell, and E. H. Jordan, "Thermal barrier coatings for gas-turbine engine applications," *Science*, vol. 296, no. 5566, pp. 280–284, 2002.

[199] W. Li, J. Sun, S. Liu, Y. Liu, L. Fu, T. Wang, S. Jiang, J. Gong, and C. Sun, "Preparation and cyclic oxidation behaviour of Re doped aluminide coatings on a Ni-based single crystal superalloy," *Corrosion Science*, p. 108354, 2019.

[200] N. S. Bornstein, "The importance of oxide scale adherence in gas turbine engines," *Materials at High Temperatures*, vol. 13, no. 4, pp. 181–184, 1995.

[201] F. Nozahic, C. Estournès, A. L. Carabat, W. G. Sloof, S. van der Zwaag, and D. Monceau, "Self-healing thermal barrier coating systems fabricated by spark plasma sintering," *Materials & Design*, vol. 143, pp. 204–213, 2018.

[202] Z. Min, S. N. Parbat, L. Yang, B. Kang, and M. K. Chyu, "Fabrication and characterization of additive manufactured nickel-based oxide dispersion strengthened coating layer for high-temperature application," *Journal of Engineering for Gas Turbines and Power*, vol. 140, no. 6, pp. 062101 1–7, 2018.

[203] S. Yuanyang, Z. Yuhong, Z. Baojun, Y. Wenkui, L. Xiaoling, and H. Hua, "Phase-field modeling of microstructure evolution of Cu-rich phase in Fe–Cu–Mn–Ni–Al quinary system coupled with thermodynamic databases," *Journal of Materials Science*, vol. 54, no. 16, pp. 11263–11278, 2019.

[204] A. T. Fromhold-Jr., "Parabolic growth law for coherent oxides," *The Journal of Chemical Physics*, vol. 41, no. 2, pp. 509–514, 1964.

[205] C. Wagner, "Equations for transport in solid oxides and sulfides of transition metals," *Progress in Solid State Chemistry*, vol. 10, pp. 3 – 16, 1975.

[206] R. P. Kolli, Z. Mao, D. N. Seidman, and D. T. Keane, "Identification of a Ni0.5(Al0.5-xMnx) B2 phase at the heterophase interfaces of Cu-rich precipitates in an α-Fe matrix," *Applied Physics Letters*, vol. 91, no. 24, p. 241903, 2007.

[207] E. Vincent, C. Becquart, C. Pareige, P. Pareige, and C. Domain, "Precipitation of the FeCu system: A critical review of atomic kinetic monte carlo simulations," *Journal of Nuclear Materials*, vol. 373, no. 1, pp. 387–401, 2008.

[208] L.-J. You, L.-J. Hu, Y.-P. Xie, and S.-J. Zhao, "Influence of Cu precipitation on tensile properties of Fe–Cu–Ni ternary alloy at different temperatures by molecular dynamics simulation," *Computational Materials Science*, vol. 118, pp. 236–244, 2016.

[209] I. Martin-Bragado, R. Borges, J. P. Balbuena, and M. Jaraiz, "Kinetic monte carlo simulation for semiconductor processing: A review," *Progress in Materials Science*, vol. 92, pp. 1–32, 2018.

[210] M. Hillert, "The compound energy formalism," *Journal of Alloys and Compounds*, vol. 320, no. 2, pp. 161 – 176, 2001. Materials Constitution and Thermochemistry. Examples of Methods, Measurements and Applications. In Memoriam Alan Prince.

[211] M. Hillert and L.-I. Staffansson, "The regular solution model for stoichiometric phases and ionic melts," *Acta Chemica Scandinavica*, vol. 24, no. 10, pp. 3618–3626, 1970.

[212] J. Heulens, B. Blanpain, and N. Moelans, "Phase field modeling of the crystallization of FeOx-SiO2 melts in contact with an oxygen-containing atmosphere," *Chemical Geology*, vol. 290, no. 3-4, pp. 156–162, 2011.

[213] I. Bellemans, N. Moelans, and K. Verbeken, "Phase-field modelling in extractive metallurgy," *Critical Reviews in Solid State and Materials Sciences*, vol. 43, no. 5, pp. 417–454, 2018.

[214] A. Basak and V. I. Levitas, "Interfacial stresses within boundary between martensitic variants: Analytical and numerical finite strain solutions for three phase field models," *Acta Materialia*, vol. 139, pp. 174–187, 2017.

[215] N. Moelans, B. Blanpain, and P. Wollants, "An introduction to phase-field modeling of microstructure evolution," *Calphad*, vol. 32, no. 2, pp. 268–294, 2008.

[216] M. J. Welland, M. H. A. Piro, S. Hibbins, and N. Wang, "A method of integrating CALPHAD data into phase-field models using an approximated minimiser applied to intermetallic layer growth in the Al–Mg system," *Calphad*, vol. 59, pp. 76–83, 2017.

[217] R. Perumal, M. Selzer, and B. Nestler, "Concurrent grain growth and coarsening of two-phase microstructures; large scale phase-field study," *Computational Materials Science*, vol. 159, pp. 160 – 176, 2019.

[218] J. Santoki, D. Schneider, M. Selzer, F. Wang, M. Kamlah, and B. Nestler, "Phase-field study of surface irregularities of a cathode particle during intercalation," *Modelling and Simulation in Materials Science and Engineering*, vol. 26, no. 6, p. 065013, 2018.

[219] I. Steinbach, "Phase-field models in materials science," *Modelling and Simulation in Materials Science and Engineering*, vol. 17, no. 7, p. 073001, 2009.

[220] L.-Q. Chen, "Phase-field models for microstructure evolution," *Annual Review of Materials Research*, vol. 32, pp. 113–140, 2002.

[221] A. Karma, *Phase Field Methods*. Encyclopedia of materials: science and technology, 2001.

[222] A. Finel, Y. Le Bouar, B. Dabas, B. Appolaire, Y. Yamada, and T. Mohri, "Sharp phase field method," *Physical Review Letters*, vol. 121, p. 025501, 2018.

[223] T. Q. Ansari, Z. Xiao, S. Hu, Y. Li, J.-L. Luo, and S.-Q. Shi, "Phase-field model of pitting corrosion kinetics in metallic materials," *npj Computational Materials*, vol. 4, no. 1, p. 38, 2018.

[224] W. J. Boettinger, J. A. Warren, C. Beckermann, and A. Karma, "Phase-field simulation of solidification," *Annual Review of Materials Research*, vol. 321, no. 1, pp. 163–194, 2002.

[225] A. Finel, Y. L. Bouar, A. Gaubert, and U. Salman, "Phase field methods: Microstructures, mechanical properties and complexity," *Comptes Rendus Physique*, vol. 11, no. 3, pp. 245–256, 2010.

[226] H. Miura, "Phase-field model for growth and dissolution of a stoichiometric compound in a binary liquid," *Phys. Rev. E*, vol. 98, p. 023311, 2018.

[227] M. Greenwood, K. N. Shampur, N. Ofori-Opoku, P. Tatu, L. Wang, S. Gurevich, and N. Provatas, "Quantitative 3D phase field modelling of solidification using next-generation adaptive mesh refinement," *Computational Materials Science*, vol. 142, pp. 153–171, 2018.

[228] R. S. Qin and H. K. Bhadeshia, "Phase field method," *Materials Science and Technology*, vol. 26, no. 7, pp. 803–811, 2010.

[229] R. Kobayashi, "Modeling and numerical simulations of dendritic crystal growth," *Physica D: Nonlinear Phenomena*, vol. 63, no. 3, pp. 410–423, 1993.

[230] R. Kobayashi, "A numerical approach to three-dimensional dendritic solidification," *Experimental Mathematics*, vol. 3, no. 1, pp. 59–81, 1994.

[231] X. lei Dong, H. Xing, K. rong Weng, and H. liang Zhao, "Current development in quantitative phase-field modeling of solidification," *Journal of Iron and Steel Research, International*, vol. 24, no. 9, pp. 865–878, 2017.

[232] G. A. Haveroth, E. A. B. d. Moraes, J. L. Boldrini, and M. L. Bittencourt, "Comparison of semi and fully-implicit time integration schemes applied to a damage and fatigue phase field model," *Latin American Journal of Solids and Structures*, vol. 15, 2018.

[233] A. A. Kuleshov, E. E. Myshetskaya, and S. E. Yakush, "Simulation of forest fires based on a two-dimensional three-phase model," *Journal of Physics: Conference Series*, vol. 1336, p. 012002, 2019.

[234] M. Wei, L. Zhang, M. Yang, K. Li, S. Liu, P. Zhao, and Y. Du, "Phase–field simulation of the solidified microstructure in a new commercial 6xxx aluminum alloy ingot supported by experimental measurements," *International Journal of Manufacturing Research*, vol. 109, no. 2, pp. 91–98, 2018.

[235] Y. Zhao, S. Ai, and D. Fang, "Elasto-plastic phase field modelling of oxidation of zirconium alloys," *International Journal of Solids and Structures*, 2017.

[236] J. E. Guyer, W. J. Boettinger, J. A. Warren, and G. B. McFadden, "Phase field modeling of electrochemistry. I. Equilibrium," *Physical Review E*, vol. 69, p. 021603, 2004.

[237] J. E. Guyer, W. J. Boettinger, J. A. Warren, and G. B. McFadden, "Phase field modeling of electrochemistry. II. Kinetics," *Physical Review E*, vol. 69, p. 021604, 2004.

[238] W. Pongsaksawad, A. C. Powell, and D. Dussault, "Phase-field modeling of transport-limited electrolysis in solid and liquid states," *Journal of The Electrochemical Society*, vol. 154, no. 6, pp. F122–F133, 2007.

[239] Q. Li, W. Chen, J. Zhong, L. Zhang, Q. Chen, and Z.-K. Liu, "On sluggish diffusion in FCC Al-Co-Cr-Fe-Ni high-entropy alloys: An experimental and numerical study," *Metals*, vol. 8, no. 1, p. 16, 2018.

[240] L. S. Darken, "Diffusion, mobility and their interrelation through free energy in binary metallic systems," *Transactions of AIME*, vol. 175, pp. 184–201, 1948.

[241] S. Aminorroaya, M. Reid, and R. Dippenaar, "Simulation of microsegregation and the solid/liquid interface progression in the concentric solidification technique," *Modelling and Simulation in Materials Science and Engineering*, vol. 19, no. 2, p. 025003, 2011.

[242] J. Sanhueza, D. Rojas, O. Prat, J. Garcia, R. Espinoza, C. Montalba, and M. Melendrez, "Precipitation kinetics in a 10.5Experimental results and simulation by TC-PRISMA/DICTRA," *Materials Chemistry and Physics*, vol. 200, pp. 342 – 353, 2017.

[243] L. da Costa Morais and R. Magnabosco, "Experimental investigations and DICTRA simulation of sigma phase formation in a duplex stainless steel," *Calphad*, vol. 58, pp. 214 – 218, 2017.

[244] H. Larsson and L. Höglund, "Multiphase diffusion simulations in 1D using the DICTRA homogenization model," *Calphad*, vol. 33, no. 3, pp. 495 – 501, 2009.

[245] H. Larsson and A. Engström, "A homogenization approach to diffusion simulations applied to α+γ Fe–Cr–Ni diffusion couples," *Acta Materialia*, vol. 54, no. 9, pp. 2431 – 2439, 2006.

[246] B.-J. Lee, "Numerical simulation of diffusional reactions between multiphase alloys with different matrix phases," *Scripta Materialia*, vol. 40, no. 5, pp. 573 – 579, 1999.

[247] Åsa Gustafson, "Coarsening of TiC in austenitic stainless steel — experiments and simulations in comparison," *Materials Science and Engineering: A*, vol. 287, no. 1, pp. 52 – 58, 2000.

[248] C. Zener, "Theory of growth of spherical precipitates from solid solution," *Journal of Applied Physics*, vol. 20, no. 10, pp. 950–953, 1949.

[249] J. Bardeen, "Diffusion in binary alloys," *Phys. Rev.*, vol. 76, pp. 1403–1405, Nov 1949.

[250] A. E. Stearn and H. Eyring, "Absolute rates of solid reactions: Diffusion.," *J. Phys. Chem.*, vol. 44, pp. 955–980, Aug. 1940.

[251] E. Kozeschnik, "2 - thermodynamic basis of phase transformations," in *Computational Materials Engineering* (K. G. JANSSENS, D. RAABE, E. KOZESCHNIK, M. A. MIODOWNIK, and B. NESTLER, eds.), pp. 7–46, Burlington: Academic Press, 2007.

[252] G. Aral, M. M. Islam, and A. C. T. van Duin, "Role of surface oxidation on the size

dependent mechanical properties of nickel nanowires: a ReaxFF molecular dynamics study," *Phys. Chem. Chem. Phys.*, vol. 20, pp. 284–298, 2018.

[253] M. L. Sushko, V. Alexandrov, D. K. Schreiber, K. M. Rosso, and S. M. Bruemmer, "Multiscale model of metal alloy oxidation at grain boundaries," *The Journal of Chemical Physics*, vol. 142, no. 21, p. 214114, 2015.

[254] J. J. Kim, S. H. Shin, J. A. Jung, K. J. Choi, and J. H. Kim, "First-principles study of interstitial diffusion of oxygen in nickel chromium binary alloy," *Applied Physics Letters*, vol. 100, no. 13, p. 131904, 2012.

[255] M. Curnan, C. Andolina, M. Li, Q. Zhu, H. Chi, W. Saidi, and J. Yang, "Connecting oxide nucleation and growth to oxygen diffusion energetics on stepped Cu(011) surfaces: An experimental and theoretical study," *Journal of Physical Chemistry C*, vol. 123, no. 1, pp. 452–463, 2019.

[256] E. Miyoshi, T. Takaki, Y. Shibuta, and M. Ohno, "Bridging molecular dynamics and phase-field methods for grain growth prediction," *Computational Materials Science*, vol. 152, pp. 118–124, 2018.

[257] W. D. Callister and D. G. Rethwisch, *Materials science and engineering.* Wiley, 8th edition., SI version ed., 2015.

[258] J. Taylor and A. Dinsdale, "A thermodynamic assessment of the Ni-O, Cr-O and Cr-Ni-O systems using the ionic liquid and compound energy models," *Zeitschrift fuer Metallkunde/Materials Research and Advanced Techniques*, vol. 81, pp. 354–366, 1990.

[259] A. Atkinson and R. I. Taylor, "The self-diffusion of Ni in NiO and its relevance to the oxidation of Ni," *Journal of Materials Science*, vol. 13, no. 2, pp. 427–432, 1978.

[260] M. O'Keeffe and W. J. Moore, "Diffusion of oxygen in single crystals of nickel oxide," *The Journal of Physical Chemistry*, vol. 65, no. 8, pp. 1438–1439, 1961.

[261] R. Lindner and Å. Åkerströ, "Diffusion of nickel-63 in nickel oxide (NiO)," *Discuss. Faraday Soc.*, vol. 23, pp. 133–136, 1957.

[262] D. Prokoshkina, V. Esin, G. Wilde, and S. Divinski, "Grain boundary width, energy and self-diffusion in nickel: Effect of material purity," *Acta Materialia*, vol. 61, no. 14, pp. 5188–5197, 2013.

[263] W. Chen, N. Peterson, and L. Robinson, "Chromium tracer diffusion in NiO crystals," *Journal of Physics and Chemistry of Solids*, vol. 34, no. 4, pp. 705–709, 1973.

[264] J. Askill, "Tracer diffusion in the chromium–nickel system," *physica status solidi (a)*, vol. 8, no. 2, pp. 587–596, 1971.

[265] M. Chen, B. Hallstedt, and L. J. Gauckler, "Thermodynamic assessment of the co-o system," *Journal of Phase Equilibria*, vol. 24, no. 3, pp. 212–227, 2003.

Appendix A

Multi-Phase to Binary phase Derivations

Writing Equation 5.27 for a binary simulation allows ϕ_j to be written as $(1-\phi_i)$

$$\Delta G_{curv} = \sigma_{ij}\left[(1-\phi_i)\nabla\phi_i - \phi_i\nabla(1-\phi_i) - \frac{36}{\eta^2}(\phi_i-(1-\phi_i))\phi_i(1-\phi_i)\right] \tag{A.1}$$

Considering only the second term in Equation A.1 for simplification;

$$\frac{36}{\eta^2}(\phi_i-(1-\phi_i))\phi_i(1-\phi_i) \tag{A.2}$$

$\phi_i-(1-\phi_i)$ can be further simplified to $2\phi_i-1$ which is equivalent to $\frac{1}{2}-\phi_i$

$$\Delta G_{curv} = \sigma_{ij}\left[(1-\phi_i)\nabla^2\phi_i - \phi_i\nabla^2(1-\phi_i) - \frac{36}{\eta^2}\left(\phi_i(1-\phi_i)(\frac{1}{2}-\phi_i)\right)\right] \tag{A.3}$$

$$\nabla^2\phi_j = -\nabla^2\phi_i \tag{A.4}$$